

M.Sc. Thesis  
Master of Science in Engineering

 DTU Fotonik  
Department of Photonics Engineering

# High average power mid-infrared supercontinuum generation in tapered chalcogenide fibers

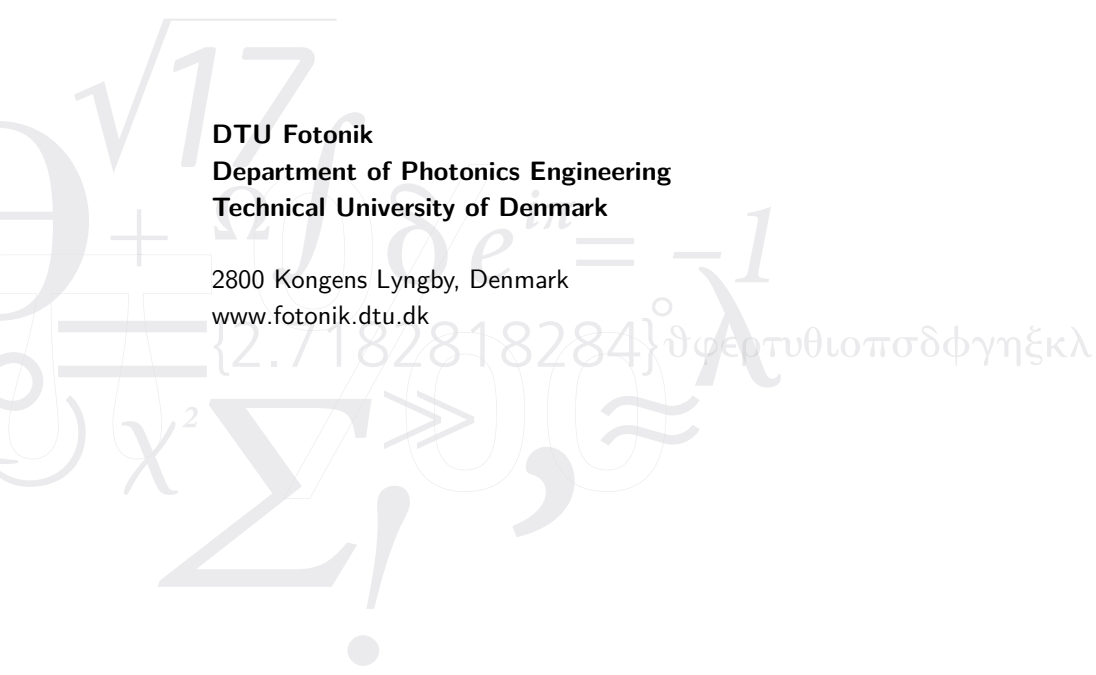
Charles N. Christensen (s113046)

Kongens Lyngby 2017



**DTU Fotonik**  
**Department of Photonics Engineering**  
**Technical University of Denmark**

2800 Kongens Lyngby, Denmark  
[www.fotonik.dtu.dk](http://www.fotonik.dtu.dk)



# Abstract

---

The topic of mid-IR supercontinuum generation in chalcogenide photonic crystal fibers (PCF) is treated not only in terms of modelling and numerical analysis, but also experimentally.

The experimental part of the thesis is comprised of two experiments that have been conducted on a chalcogenide PCF of the composition  $\text{Ge}_{10}\text{As}_{22}\text{Se}_{68}$ . In the first of those experiments, the dispersion of the chalcogenide fiber is measured and compared with predictions from numerical modelling of the same fiber in order to validate the fiber modelling. In the second experiment the self-phase modulation occurring in the chalcogenide fiber is measured in an attempt to estimate the nonlinear refractive index,  $n_2$ , by fitting the measurements to numerical simulations using the  $n_2$  as a free parameter. The value found is  $3.5 \cdot 10^{-18} \text{ m}^2/\text{W}$  at  $1.93 \text{ }\mu\text{m}$ .

The main focus of the thesis is to simulate dual-polarisation pulse propagation in tapered chalcogenide PCF. To this end an efficient interaction picture Dormand-Prince Runge-Kutta based method has been designed and is shown to perform better than some other methods in the literature. The simulation results reveal prominent soliton dynamics in a broad mid-IR supercontinuum when pumping with high average power, and these predictions are found to be consistent with the findings of a reference experiment based on the same fiber.

# Preface

---

This Master's thesis is the product of a 30 ECTS Master's project at DTU Fotonik that has been undertaken as the last part of a degree in Mathematical Modelling and Computation at the Technical University of Denmark. While my M.Sc. is in mathematics, several of my elective courses have been in photonics, physics and mathematical physics. In addition to that I have a B.Sc. in Physics and Nanotechnology with a *fagprojekt* and Bachelor's thesis also completed at DTU Fotonik. Given my mixed background, I have had an equal desire to pursue problems of both mathematical and physical nature relating to the topic of the thesis, and I think and hope the content reflects that, not in the sense that it is a little bit of everything, but rather that it is comprehensible by covering all the important aspects that govern this field: theoretical physics, experimental physics, mathematical modelling and numerical analysis.

The Master's project has been made in the Fiber Sensors & Supercontinuum group lead by professor Ole Bang, whom has also been my supervisor in the project. I have appreciated his guidance and his insistence on regular weekly meetings.

I would like to thank Rasmus D. Engelholm, whom is a PhD student in the Fiber Sensors & Supercontinuum group. Rasmus has been of great assistance during the whole project, and early on provided me with some code that set me on track to eventually developing my own solver. He has also been patient when I've occasionally hurled a flurry of questions at him.

Christian Rosenberg Petersen, a postdoc in the group, also has my gratitude for having spent several hours with me in the lab, where he has assisted me in the two experiments documented in the thesis. Without his expertise the experiments could easily have ended up being a great time sink inhibiting the progress on the modelling front.

Kongens Lyngby, September 19, 2017

A handwritten signature in black ink that reads "Charles N. Christensen". The signature is written in a cursive, flowing style.

Charles N. Christensen (s113046)

# Contents

---

<b>Abstract</b>	<b>i</b>
<b>Preface</b>	<b>ii</b>
<b>Contents</b>	<b>iii</b>
<b>1 Introduction</b>	<b>1</b>
1.1 Structure of this thesis . . . . .	2
<b>2 Relevant mathematics and physics</b>	<b>3</b>
2.1 Fourier transform and notation . . . . .	3
2.2 Optical modes in fibers . . . . .	3
2.3 Propagation equations . . . . .	5
2.3.1 NLSE . . . . .	5
2.3.2 GNLSE . . . . .	5
2.3.3 MM-GNLSE . . . . .	6
2.4 Important quantities . . . . .	8
2.4.1 Power Spectral Density . . . . .	8
2.4.2 Spectrogram . . . . .	8
<b>3 Modelling of fibers and supercontinuum generation</b>	<b>9</b>
3.1 Modelling photonic crystal fibers with COMSOL . . . . .	9
3.2 Numerical parameters . . . . .	10
3.3 Quantum noise . . . . .	11
3.4 Solving the MM-GNLSE by numerical integration . . . . .	11
3.4.1 Interaction picture methods . . . . .	13
3.4.2 Adaptive step size control . . . . .	14
3.5 Modelling tapered fibers . . . . .	14
<b>4 Nonlinear effects in optical fibers</b>	<b>17</b>
4.1 Kerr nonlinearity and group velocity dispersion . . . . .	17
4.2 Solitons . . . . .	18
4.3 Delayed Raman response . . . . .	20
<b>5 Numerical Analysis</b>	<b>22</b>
5.1 Convergence behaviour for fiber modelling . . . . .	22
5.2 Validation and performance of GNLSE solver . . . . .	23
5.2.1 Reproducing an analytical second order soliton solution . . . . .	23
5.2.2 Convergence rate when simulating supercontinuum generation . . . . .	24
5.3 Conserved quantities . . . . .	26

<b>6 Experiments</b>	<b>28</b>
6.1 Dispersion measurement . . . . .	28
6.1.1 Experimental method and setup . . . . .	28
6.1.2 Results . . . . .	30
6.2 Estimation of nonlinear refractive index . . . . .	32
6.2.1 Experimental setup . . . . .	33
6.2.2 Analysis and results . . . . .	34
<b>7 Supercontinuum generation in tapered chalcogenide fibers</b>	<b>37</b>
7.1 Discretizing a tapered fiber . . . . .	37
7.2 Optical properties along taper . . . . .	39
7.3 Importance of fiber dimensions . . . . .	41
7.4 Reference experiment . . . . .	43
7.5 Reproducing the experimental measurements . . . . .	43
7.5.1 Attempting to reproduce with GNLSE . . . . .	45
7.5.2 Attempting to reproduce with simplified MM-GNLSE . . . . .	45
7.5.3 Using full MM-GNLSE . . . . .	47
7.5.4 Matching the long wavelength loss edge . . . . .	51
7.6 Dependence on power . . . . .	52
7.7 Sensitivity to important parameters . . . . .	54
7.7.1 Fractional Raman contribution . . . . .	55
7.7.2 Initial polarisation seeding . . . . .	55
7.7.3 Fiber dimensions . . . . .	56
7.8 Variations of the MM-GNLSE . . . . .	56
7.8.1 Excluding four-wave mixing . . . . .	57
7.8.2 Including higher-order shock terms . . . . .	57
<b>8 Conclusion</b>	<b>60</b>
<b>A The DPIP method</b>	<b>62</b>
<b>B Unchirped SPM fits</b>	<b>63</b>
<b>C Implementation of MM-GNLSE solver</b>	<b>64</b>
<b>D Soliton numbers</b>	<b>74</b>
<b>Bibliography</b>	<b>75</b>

# CHAPTER 1

## Introduction

A supercontinuum (SC) is a continuous spectrum of light that has been strongly broadened from a narrow band pump beam. There are multiple techniques to generating SC, but the common trend among all techniques is that nonlinear interactions within the medium give rise to the broadening. One such medium is the photonic crystal fiber (PCF) that is the fiber type exclusively studied in this thesis. The structure of a PCF is shown on figure 1.1, where the cladding is seen to have five layers of air holes. The size of the cladding can vary, and in the case of the PCFs simulated in this thesis, the cladding has only three layers. A microscope image of one of those PCFs is shown later.

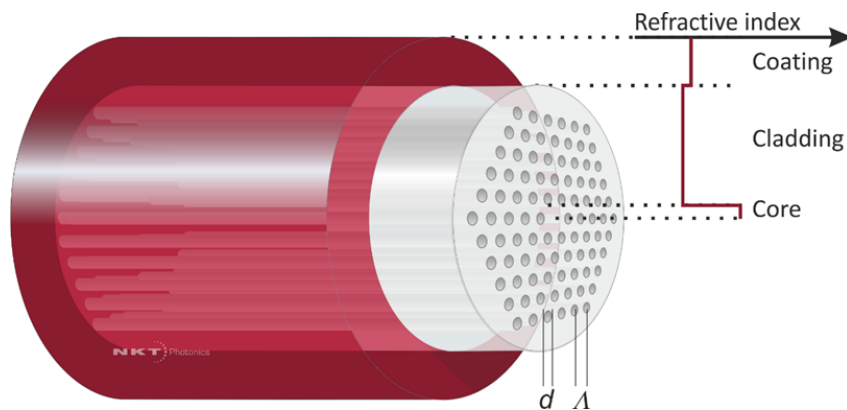


**Figure 1.1:** A photonic crystal fiber with the fiber dimensions pitch,  $\Lambda$ , and hole diameter,  $d$ . Source: NKT Photonics.

While the phenomenon of SC dates all the way back to 1970 [1], it has mostly been in the last 15 or so years that the field has really emerged as an active research field driven largely by technological advances in the sources that generate supercontinua.

The applications of SC sources have consequently seen a large growth today spanning fields such as optical coherence tomography, spectroscopy and optical frequency metrology, the latter application being awarded a Nobel Prize in 2005 [2].

Many applications require supercontinuum in the mid-IR. However, commercial SC sources have reached the limit of the mature silica technology given the physical limitations of silica that renders it effectively opaque at  $2\ \mu\text{m}$  and above due to the material absorption increasing wildly at this point. Hence, a shift towards other types of glasses, those known as soft glasses, has occurred in recent years with tellurite, ZBLAN and chalcogenide attracting most attention [3]. In addition to those glasses being transparent in the mid-IR spectrum, they also have much higher nonlinear refractive indices, especially chalcogenide for which the nonlinear refractive index can be 200-1000 times higher [4, 5]. To increase the nonlinearity even further, a fiber can be tapered, which means that it has been stretched while being heated resulting in a thinner fiber. A tapered fiber is often described by five sequential segments: before taper, down taper,

taper waist, up taper and after taper. The fiber dimensions decrease (increase) in the down (up) taper, but remain constant in the other three segments.

For the reasons above, tapered chalcogenide fibers are interesting candidates for use as propagating medium in SC generation, and we shall consider them throughout the thesis, both experimentally and numerically.

## 1.1 Structure of this thesis

The goal of the thesis is to model dual-polarisation pulse propagation<sup>1</sup> in tapered chalcogenide fibers in the mid-IR spectrum, 2-10  $\mu\text{m}$ , when pumped with high average power, as well as modelling the fibers alone (in order to find mode functions etc.), and finally to experimentally characterise the same chalcogenide fibers with the purpose to compare with and validate numerical results.

Three levels of testing and validation with different focuses and strictness will occur. In section 4 we explore some basic and essential nonlinear effects, but at the same time this will provide an informal test of the implementation that was developed as part of this project, since the findings here are well-known and in some cases have analytical roots. Section 5 contains a more strict numerical analysis of convergence and consistency with respect to analytical solutions and conserved quantities. Then in section 6 two experiments performed during this project are documented and the findings are compared with numerical modelling and other experimental findings, and will thus also serve as a reality check of some of the modelling. Finally, we should have some confidence in the implementation and we will see how well it stands up against an actual mid-IR SC experiment based on the same tapered chalcogenide PCF pumped with high average power.

---

<sup>1</sup>Referred to also as multimode propagation given the presence of two polarisation modes.

# CHAPTER 2

## Relevant mathematics and physics

---

### 2.1 Fourier transform and notation

In this work the following definition of the Fourier transform and inverse Fourier transform is used

$$\hat{F}\{f(t)\} = \tilde{f}(\omega) = \int_{-\infty}^{\infty} f(t)e^{i\omega t} dt, \quad (2.1)$$

$$\hat{F}^{-1}\{\tilde{f}(\omega)\} = f(t) = \frac{1}{2\pi} \int_{-\infty}^{\infty} \tilde{f}(\omega)e^{-i\omega t} d\omega. \quad (2.2)$$

An important result that can be derived from the Fourier transform is Parseval's theorem [6]

$$\int_{-\infty}^{\infty} f(t)g^*(t) dt = \frac{1}{2\pi} \int_{-\infty}^{\infty} \tilde{f}(\omega)\tilde{g}^*(\omega) d\omega, \quad (2.3)$$

where the special case when  $f = g = A(t)$  will be useful later.

The following notation for convolutions will be used

$$f * g = \int_{-\infty}^{\infty} f(t)g(t-t') dt', \quad (2.4)$$

which by the convolution theorem is equivalent to  $f * g = \hat{F}^{-1}\{\hat{F}\{f\}\hat{F}\{g\}\}$ . And finally, a differential operator with respect to the variable  $x$  will be written as  $\partial_x$ , i.e.  $\partial f(x)/\partial x = \partial_x f(x)$ .

### 2.2 Optical modes in fibers

From Maxwell's equations one can derive the wave equation that describes light propagation in optical fibers [7]

$$\nabla \times \nabla \times \mathbf{E}(\mathbf{r}, t) = -\frac{1}{c^2} \frac{\partial^2 \mathbf{E}(\mathbf{r}, t)}{\partial t^2} - \mu_0 \frac{\partial^2 \mathbf{P}(\mathbf{r}, t)}{\partial t^2}, \quad (2.5)$$

where  $\mathbf{E}$  is the electric field,  $\mathbf{P}$  is the polarisation,  $\mu_0$  is the vacuum permeability and  $c$  is the speed of light. In deriving (2.5) it is assumed that the fiber is nonmagnetic and that there is no free charge [8].

The polarisation is often written as a Taylor expansion in the electric field [9]

$$\mathbf{P}(\mathbf{r}, t) = \epsilon_0 \left( \chi^{(1)} + \chi^{(2)} \mathbf{E}(\mathbf{r}, t) + \chi^{(3)} \mathbf{E}(\mathbf{r}, t) \mathbf{E}(\mathbf{r}, t) \right) \mathbf{E}(\mathbf{r}, t), \quad (2.6)$$

where  $\chi^n$  is the  $n$ th order susceptibility tensor forming tensor scalar products with the electric field.

The first term is the linear susceptibility  $\chi^{(1)}$ , which determines the refractive index and attenuation of the media. The second-order term is responsible for second-harmonics generation, but since amorphous solids, such as glass (e.g. chalcogenide), display inversion symmetry, also known as centrosymmetry, at a molecular level, the  $\chi^{(2)}$  term vanishes as well as all other even-order terms [9, 10, 11]. The third-order term gives rise to several nonlinear effects, in particular the Kerr effect, which we will return to in a later section.

The expression (2.6) neglects the time-dependence of the susceptibility tensor, which is equivalent to assuming that the medium responds instantaneously, and this in turn implies that the medium must be lossless and dispersionless [9]. Neither of those things do we want to assert, and thus we have to introduce a convolution between the electric field and the susceptibility in order to account for the time-dependency. If we write the polarisation as consisting of a linear and a nonlinear part, i.e.,

$$\mathbf{P}(\mathbf{r}, t) = \mathbf{P}_L(\mathbf{r}, t) + \mathbf{P}_{NL}(\mathbf{r}, t), \quad (2.7)$$

then the linear part including the time-dependent susceptibility tensor is given by [9]

$$\mathbf{P}_L(\mathbf{r}, t) = \epsilon \int_{-\infty}^t \chi^{(1)}(t - t') \mathbf{E}(\mathbf{r}, t') dt'. \quad (2.8)$$

The nonlinear part  $\mathbf{P}_{NL}$  is omitted here for brevity (see [7, 9]), but in a general case it consists of convolutions of the higher-order susceptibility terms of (2.6), although it very often in fiber optics, as well as in this work, is taken to only include convolutions with the  $\chi^{(3)}$  term.

Now in order to describe the electric modes propagating in a fiber, we return to (2.5), but consider it in the frequency domain, while treating  $\mathbf{P}_{NL}$  as a small perturbation, such that we can neglect it for now [7]. Using the convolution theorem to write the  $\chi^{(1)}$  convolution in the frequency domain and substituting  $\mu_0\epsilon_0 = 1/c^2$  yields

$$\nabla \times \nabla \times \tilde{\mathbf{E}}(\mathbf{r}, \omega) = \left[1 + \tilde{\chi}^{(1)}(\omega)\right] \frac{\omega^2}{c^2} \tilde{\mathbf{E}}(\mathbf{r}, \omega) = \epsilon_r(\omega) k_0^2 \tilde{\mathbf{E}}(\mathbf{r}, \omega), \quad (2.9)$$

where  $\tilde{\mathbf{E}}(\mathbf{r}, \omega)$  and  $\tilde{\chi}^{(1)}(\omega)$  are Fourier transforms of their time domain counterparts. The quantity  $1 + \tilde{\chi}^{(1)}(\omega)$  is also known as the relative permittivity  $\epsilon_r(\omega)$ , which is related to the refractive index and attenuation coefficient through  $\epsilon_r = (n + i\alpha c/2\omega)^2$  [7].

Equation (2.9) can be solved numerically, e.g. using a finite element method (FEM) solver such as COMSOL, in order to find the modes of a fiber. Due to the cylindrical symmetry of a fiber, separation of variables can be employed to find solutions that fulfil

$$\tilde{\mathbf{E}}(\mathbf{r}, \omega) = \mathbf{F}(x, y, \omega) e^{uz}, \quad (2.10)$$

where  $u$  is the eigenvalue returned by COMSOL and it corresponds to  $-i\beta - \alpha/2$  with  $\beta$  being the propagation constant and  $\alpha$  being the attenuation coefficient (confinement loss<sup>1</sup>) both used in the following section. The eigenvalue also provides the effective refractive index via  $n_{\text{eff}} = (\beta - i\alpha/2)/k_0$ .

---

<sup>1</sup>Generally, the attenuation coefficient consists of both confinement loss and material loss, where the latter usually is measured and added to the confinement loss – this is described later in the thesis.

## 2.3 Propagation equations

### 2.3.1 NLSE

Starting from wave equation (2.5) and this time explicitly including the nonlinear part of the polarisation, however still assumed to be a small perturbation, one can derive an equation for the propagation of an optical mode in a fiber known in the simplest form as the nonlinear Schrödinger equation (NLSE). One major simplification that has to be made in deriving the NLSE is that the optical field maintains its polarisation along the fiber enabling a scalar description of the mode functions. In the interest of undoing this simplification, among other reasons, we will later consider an extended equation, the MM-GNLSE.

The NLSE takes the form of a differential equation in the field envelope  $A(z, t)$  [7]

$$\partial_z A(t, z) = -i\frac{1}{2}\beta_2\partial_t^2 A(t, z) + i\gamma(\omega_0)|A(z, t)|^2 A(z, t), \quad (2.11)$$

in which  $\gamma(\omega_0)$  is the nonlinear coefficient and  $\beta_2$  is the group velocity dispersion (GVD) given by  $\beta_2 = \partial_\omega^2 \beta(\omega)$  with  $\beta$  being the propagation constant. The time variable  $t$  that is present in (2.11) is called delayed time, often retarded time in the literature, because it represents the time with respect to a frame of reference moving at the group velocity speed. This time transformation is rather simple and not further described here (see [3, 7]). Had this transformation not been done, equation (2.11) would have to be extended with a term  $\beta_1 \partial_t A(z, t)$  on the right-hand side.

Note that the nonlinear coefficient is written as a function of  $\omega_0$ , because it can also be expressed as [7]

$$\gamma(\omega_0) = \frac{\omega_0 n_2}{c A_{\text{eff}}}, \quad \text{with} \quad A_{\text{eff}} = \frac{\left( \int \int_{-\infty}^{\infty} |F(x, y)|^2 dx dy \right)^2}{\int \int_{-\infty}^{\infty} |F(x, y)|^4 dx dy}, \quad (2.12)$$

where  $n_2$  is the nonlinear refractive index, and  $A_{\text{eff}}$  is the effective mode area. The definition of (2.12) implies that the field envelope  $A(z, t)$  has been normalised such that  $|A|^2$  represents the optical power (i.e.  $[A] = [\text{W}^{1/2}]$ ), which is most convenient. Other normalisations can be chosen as well, for instance normalising w.r.t. the electric field in order for  $A$  to have units of the electric field ( $[\text{V/m}]$ ), which would lead to another definition of  $\gamma$  [7]. The nonlinear refractive index quantifies the Kerr effect, namely that the refractive index of a medium is dependent on the optical intensity  $I$  in a linear fashion,  $n = n_0 + n_2 I$ .

Higher-order dispersion can also be incorporated into the NLSE, for instance third-order dispersion is included by adding the term  $i\frac{1}{6}\beta_3\partial_t^3 A(t, z)$  on the right-hand side of (2.11) with  $\beta_3 = \partial_\omega^3 \beta(\omega)$ .

Finally, it is noted that equation (2.11) can be exactly solved in the form of soliton solutions, of varying orders, which will be covered later as a means of validating numerical implementations.

### 2.3.2 GNLSE

One of the assumptions that lead to the NLSE is that the nonlinear polarisation response is instantaneous, which is analogous to not including the effect of molecular vibrations known as the Raman effect. In reality the response occurs over a period of time, hence the name delayed Raman response. For chalcogenide fibers the Raman response can easily last as much as 1 ps

[12], whereas the response time window for silica is generally below 100 fs [7]. Since the Raman effect is also power dependent, the NLSE is only accurate for either low peak power pulses or pulses with pulse widths much larger than the period in which the Raman response occurs. In this work we will only consider high average power pulses with pulse widths below 2 ps, and thus it is crucial to include the Raman response, especially when simulating chalcogenide fibers.

As in section 2.2 we will now account for the time-dependence of the susceptibility tensor as a convolution with the electric field to state a more accurate version of the NLSE. Furthermore, a full Taylor expansion of the propagation constant is included, as well as attenuation via the variable  $\alpha$ . With these additions the NLSE becomes the generalised nonlinear Schrödinger equation (GNLSE) given by [7, 13]

$$\partial_z A_z = i \sum_{m \geq 2} \frac{i^m \beta_m}{m!} \partial_t^m A - \frac{\alpha}{2} + i\gamma(\omega_0) (1 + i\tau \partial_t) \left[ A \int_{-\infty}^{\infty} R(t') |A(z, t - t')|^2 dt' \right], \quad (2.13)$$

where  $R(t')$  is the Raman response function and  $\tau$  is called the shock time. The Raman response function can be written as

$$R(t) = (1 - f_R)\delta(t) + f_R h_R(t), \quad (2.14)$$

with  $f_R$  being the fraction of the Kerr term that is delayed while  $(1 - f_R)$  is the fraction that is instantaneous. The function  $h_R(t)$  is called the delayed Raman response function. The shock time  $\tau$  is [2]

$$\tau = \frac{1}{\omega_0} - \frac{1}{n_{\text{eff}}} (\partial_\omega n_{\text{eff}})_{\omega=\omega_0} - \frac{1}{A_{\text{eff}}} (\partial_\omega A_{\text{eff}})_{\omega=\omega_0}. \quad (2.15)$$

As the first term is dominant, the approximation  $\tau = 1/\omega_0$  is often used, but according to [7, 2] the second and especially the third term becomes important for simulating very broad SC.

### 2.3.3 MM-GNLSE

We now seek to further extend the GNLSE. The NLSE and GNLSE describe the propagation of just a single mode. When simulating multimode fibers one needs to account for the coupling between the modes. Even for a single-mode fiber two polarisation modes can exist, and they might couple as well. The latter case is true for the fibers considered in this thesis. Hence, we will need an equation that describe the propagation of a field when more than one mode is present, while at the same time featuring the same depth as the GNLSE – this equation is commonly referred to as the multimode generalised Schrödinger equation (MM-GNLSE). The MM-GNLSE that has been chosen as a basis for this work is documented in [13], and in addition to the features mentioned above, it also incorporates an extra delayed Raman response term oscillating at twice the optical frequency. For the  $p$ th mode the equation reads

$$\begin{aligned} \partial_z A_p = & i(\beta_0^{(p)} - \beta_0) A_p - (\beta_1^{(p)} - \beta_1) \partial_t A_p + i \sum_{n \geq 2} \frac{\beta_n^{(p)}}{n!} (i \partial_t)^n A_p \\ & + i \frac{n_2 \omega_0}{c} \sum_{l, m, n} \left\{ \left( 1 + i \tau_{plmn}^{(1)} \partial_t \right) Q_{plmn}^{(1)} 2A_l [R * (A_m A_n^*)] \right. \\ & \left. + \left( 1 + i \tau_{plmn}^{(2)} \partial_t \right) Q_{plmn}^{(2)} A_l^* [(R \cdot e^{2i\omega_0 \tau}) * (A_m A_n)] \right\}, \end{aligned} \quad (2.16)$$

in which the so-called overlap integrals  $Q_{plmn}^{(1,2)}$  are comparable to  $A_{\text{eff}}$  used previously. The overlap integrals are evaluated at  $\omega_0$  according to [13], while it may be kept dependent on  $\omega$  as done in [14] in order to account for mode profile dispersion (i.e. a frequency-dependent effective area). When simulating supercontinuum generation the effect of mode profile dispersion may be important to include as pointed out in [15], although the approach taken in [15] differs somewhat from the one employed here. The constants  $\beta_0$  and  $1/\beta_1$  are free parameters corresponding to an overall phase factor and the velocity of the temporal reference frame, respectively. As noted previously the time variable  $t$  represents delayed time w.r.t. this reference frame, and to minimise the overall delay the velocity should be chosen to be close to the group velocity at the carrier frequency. Now that we have multiple modes, we choose to set  $\beta_0$  and  $\beta_1$  as the propagation constant and inverse group velocity of the fundamental mode at  $\omega_0$ .

The overlap integrals are defined as

$$Q_{plmn}^{(1)}(\omega) = \frac{\varepsilon_0^2 n_0^2 c^2}{12} \frac{\int dx dy [\mathbf{F}_p^*(\omega) \cdot \mathbf{F}_l(\omega)] [\mathbf{F}_m(\omega) \cdot \mathbf{F}_n(\omega)^*]}{N_p(\omega) N_l(\omega) N_m(\omega) N_n(\omega)}, \quad (2.17)$$

$$Q_{plmn}^{(2)}(\omega) = \frac{\varepsilon_0^2 n_0^2 c^2}{12} \frac{\int dx dy [\mathbf{F}_p^*(\omega) \cdot \mathbf{F}_l(\omega)^*] [\mathbf{F}_m(\omega) \cdot \mathbf{F}_n(\omega)]}{N_p(\omega) N_l(\omega) N_m(\omega) N_n(\omega)}, \quad (2.18)$$

in which the normalisation factor

$$N_n(\omega) = \frac{1}{2} \left( \int dx dy [\mathbf{F}_m^*(\omega) \times \mathbf{H}_n(\omega) + \mathbf{F}_n(\omega) \times \mathbf{H}_m^*] \cdot \mathbf{e}_z \right)^{1/2} \quad (2.19)$$

is used to ensure that the squared field envelope is in units of power.

The response functions occurring in (2.16) are defined slightly different than for the GNLSE,

$$R(t) = (1 - f_R) \delta(t) + \frac{3}{2} f_R h(t). \quad (2.20)$$

Another difference to the GNLSE is that the shock time is now mode-dependent and there is one for each Raman response convolution,

$$\tau_{plmn}^{(1,2)} = \frac{1}{\omega_0} + \left\{ \partial_\omega \ln [Q_{plmn}^{1,2}(\omega)] \right\}_{\omega=\omega_0}. \quad (2.21)$$

As noted for the GNLSE, the approximation  $\tau_{plmn}^{(1,2)} = 1/\omega_0$  can in many cases be used as it tends to be the dominant term, but for very broad SC both terms may be of importance [2]. Thus we will keep the expression general for now and in a later section it will be investigated whether this approximation is valid.

In order to solve (2.16) numerically it is advantageous to Fourier transform into the frequency domain as the time derivatives become products,  $\hat{F}\{\partial_t^n\} = [-i(\omega - \omega_0)]^n \hat{F}$ . Applying the Fourier transform to (2.16) yields

$$\begin{aligned} \partial_z \tilde{A}_p = i & \left[ \beta^{(p)}(\omega) - \beta_0 - (\omega - \omega_0) \beta_1 \right] \tilde{A}_p \\ & + i \frac{n_2 \omega_0}{c} \left[ 1 + \frac{\omega - \omega_0}{\omega_0} \right] \sum_{l,m,n} \hat{F} \left\{ Q_{plmn}^{(1)} 2A_l [R(\tau) * (A_m A_n^*)] \right. \\ & \left. + Q_{plmn}^{(2)} A_l^* [(R \cdot e^{2i\omega_0 \tau}) * (A_m A_n)] \right\}, \end{aligned} \quad (2.22)$$

where  $\beta^{(p)}(\omega)$  represents the exact functional form of the propagation constant as given by the full Taylor expansion.

## 2.4 Important quantities

The following physical quantities will be used throughout the thesis.

### 2.4.1 Power Spectral Density

Consider an electric field,  $A$ , for a pulse, which is normalized such that

$$P(t) = |A(t)|^2, \quad E = \int_{-\infty}^{\infty} |A(t)|^2 dt, \quad (2.23)$$

where  $P$  and  $E$  denotes power and energy, respectively.

According to Parseval's theorem we have that

$$E = \int_{-\infty}^{\infty} |A(t)|^2 dt = \frac{1}{2\pi} \int_0^{\infty} |\tilde{A}(\omega)|^2 d\omega, \quad (2.24)$$

where only positive frequencies are included and  $\omega$  is the angular frequency. Making a variable substitution from  $\omega$  to  $\lambda = 2\pi c/\omega$  and using  $d\lambda = d\omega(-2\pi c/\omega^2)$ , we can write

$$E = \frac{1}{2\pi} \int_{\infty}^0 |\tilde{A}(\lambda)|^2 \left(-\frac{\omega^2}{2\pi c}\right) d\lambda \quad (2.25)$$

$$= \frac{1}{2\pi} \int_0^{\infty} |\tilde{A}(\lambda)|^2 \left(-\frac{(2\pi c/\lambda)^2}{2\pi c}\right) d\lambda \quad (2.26)$$

$$= \int_0^{\infty} |\tilde{A}(\lambda)|^2 \frac{c}{\lambda^2} d\lambda. \quad (2.27)$$

We define the integrand of (2.27) as the energy spectral density,  $\text{ESD}(\lambda) \equiv |\tilde{A}(\lambda)|^2 \frac{c}{\lambda^2}$ . This energy quantity is associated with a single pulse. To get the energy per time in a pulsed system, rather than the energy per pulse, we multiply with the repetition of the laser ( $f_{\text{rep}}$ ) and define the product as the power spectral density,  $\text{PSD}(\lambda) \equiv f_{\text{rep}} \text{ESD}(\lambda)$ .

### 2.4.2 Spectrogram

When considering a pulse after some propagation, usually one would visualise it in the time or frequency domain separately. However, it can bring some valuable insight to consider both domains at once, in particular how a certain part of the pulse in one domain is manifested in the other domain. A spectrogram provides a means of visualising the propagation in this fashion.

In essence the spectrogram is calculated by partitioning or gating the pulse in the time domain into intervals of a chosen length, and then Fourier transforming the part of the field in each interval to find its spectral equivalent. Mathematically, we can state this as the following integral [16]

$$S(z, t, \omega) = \left| \int_{-\infty}^{\infty} e^{-(\omega - \omega_0)t'} e^{-(t'-t)^2/T_w^2} A(z, t') dt' \right|^2, \quad (2.28)$$

where the  $T_w$  is the width of the moving time window in which the field is sampled and then Fourier transformed.

# CHAPTER 3

## Modelling of fibers and supercontinuum generation

### 3.1 Modelling photonic crystal fibers with COMSOL

The commercially available FEM solver COMSOL is used to solve (2.9), which supports the equation as is. The resulting eigenvalues that are returned is written as  $\lambda = -i\beta - \alpha/2$ , where  $\beta$  is the propagation constant and  $\alpha$  is the attenuation coefficient, although this value only includes confinement loss as previously noted (material loss can also be added as we shall see later).

To find the optical modes of the fiber, the geometry of the fiber is defined in COMSOL after which an appropriate discretization is performed, i.e. the geometry is partitioned into a mesh of finite elements, or triangles in our case. For the problem to be well-defined, we must also specify the boundary condition. For this purpose we apply a perfectly matched layer (PML), which is an absorbing layer with the property that incident waves do not reflect at the interface [8], but are extinguished completely. The purpose of the PML is to imitate the outer cladding and coating of an optical fiber, which typically constitute a much larger area than the fiber core, and thus a truncation is necessary for computational feasibility. A mode field will be truncated at the outer boundary of a PML, and therefore it is important to ensure that the PML is sufficiently thick. This will be addressed in the chapter on Numerical Analysis along with a study of what mesh resolutions are necessary.

An example of the fiber geometry as defined in COMSOL can be seen in figure 3.1, and an example of a rather coarse mesh is shown in figure 3.2.

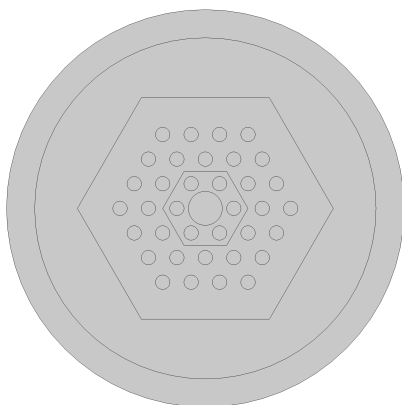


**Figure 3.1:** PCF geometry as defined in COMSOL. The outmost layer is a PML boundary condition.

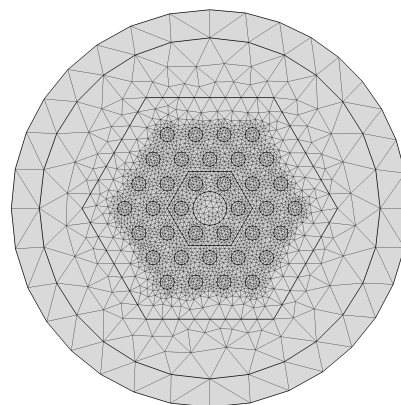


**Figure 3.2:** Adaptive mesh of geometry with coarse refinement resulting in roughly 6000 elements.

## 3.2 Numerical parameters

When solving the NLSE numerically, the choices of how to discretize the frequency and time grids are worthy of careful consideration. At an overall level we simply have to make sure that the temporal and spectral windows are sufficiently large to completely contain the field in each respective domain, and that the grid spacings are small enough to resolve the field accurately. Apart from discretisation parameters, we shall also treat  $\omega_0$  as a free parameter. While  $\omega_0$  is often taken to be the angular frequency of the pump laser,  $\omega_p$ , but for simulating SC that extends to below half the wavelength of the pump laser, other values of  $\omega_0$  will have to be chosen – the reason for this will be clear in the following. When choosing  $\omega_0$  to be different than  $\omega_p$ , a chirp of the input pulse has to be introduced [3], while the velocity of the moving frame of reference in the propagation equation may still favourably be chosen as the group velocity at  $\omega_p$  not  $\omega_0$  (to decrease overall delay and thus the required size of time window).

**Domain windows.** For the temporal window to have a sufficiently large span, say,  $t_{\text{width}}$ , we can state a simple condition  $t_{\text{width}} = \delta_t N$ , where  $\delta_t$  is the temporal grid spacing and  $N$  is the number of points in the field, preferably a power of 2 to enable the FFT to work efficiently. Since time is described in a frame moving at the group velocity, the temporal window is placed symmetrically around  $t = 0$ , such that

$$t \in \left[ -\frac{\delta_t N}{2}, \frac{\delta_t N}{2} \right]. \quad (3.1)$$

In order for the spectral window to be large enough, we have to take the Nyquist-Shannon sampling theorem into account [17], which states that the sampling rate, i.e.  $1/\delta_t$ , must be twice that of the maximum frequency to be represented, hence  $1/\delta_t = 2f_{\text{max}}$ , where  $f_{\text{max}}$  is the frequency in the moving frame, shifted  $\omega_0/(2\pi)$  from the physical frequency. Hence, we have the following spectral window

$$\lambda \in \left[ \frac{c}{\frac{\omega_0}{2\pi} + \frac{1}{2\delta_t}}, \frac{c}{\frac{\omega_0}{2\pi} - \frac{1}{2\delta_t}} \right] \quad (3.2)$$

From this expression it is apparent that a lower bound for  $\delta_t$  exists, since division by zero must be avoided as well as operating with negative frequencies. For the mid-IR SC that we will be considering in this thesis, the spectral window should at least span from  $\lambda_{\text{min}} = 1.2 \mu\text{m}$  to  $\lambda_{\text{max}} = 12 \mu\text{m}$ , which by use of (3.2) yields approximately  $2\pi c/\omega_0 = 2.2 \mu\text{m}$  and  $\delta_t = 4.5 \text{ fs}$ .

**Discretization points.** The pump laser considered in chapter 7 generates pulses with a temporal width of  $t_{\text{FWHM}} = 250 \text{ fs}$ , meaning that with the above value for  $\delta_t$  there will be over 50 points to resolve the pump pulse before propagation in the fiber. As it turns out this is more than enough, even half as many is plenty, which can be easily checked by convergence tests numerically and it is consistent with findings in [3].

Had the value of  $\delta_t$  been too large, we could simply sacrifice a bit of efficiency by allowing the spectral window to be larger than necessary – for instance reducing the short wavelength edge results in a lower  $\delta_t$  value (and higher  $\omega_0$ ).

In the frequency domain we also have to make sure that a sufficiently large number of points, say  $m$ , resolves the initial pump pulse. Given the temporal pulse width  $t_{\text{FWHM}}$ , the frequency width of the ESD is given by  $\omega_{\text{FWHM}} = 4 \ln 2/t_{\text{FWHM}}$  [3]. The maximum frequency grid spacing

is thus  $d_\omega = \omega_{\text{FWHM}}/m$ . The value of  $m$  should be something similarly large as  $t_{\text{FWHM}}/\delta_t$  above.

Finally, the time and frequency spacing set two conditions on the number of discretization points  $N$  in order for the temporal and spectral windows to be large enough. We must choose  $N$  such that

$$N \geq \min \left[ \frac{t_{\text{width}}}{\delta_t}, \frac{2\pi c \left( \frac{1}{\lambda_{\min}} - \frac{1}{\lambda_{\max}} \right)}{\delta_\omega} \right], \quad (3.3)$$

where  $\lambda_{\min}$ ,  $\lambda_{\max}$  are as stated previously.

### 3.3 Quantum noise

In realised nonlinear optical systems noise has an important influence on supercontinuum generation. Indeed noise might even be the very cause of the supercontinuum as it can induce modulational instability (MI), where deviations from a periodic waveform are reinforced by nonlinearity.

The noise source that is employed in this thesis when modelling supercontinuum generation is the one-photon-per-mode model [16, 11]. In this model the input pulse is changed such that at every frequency bin  $\omega_n$  a field with random phase and an energy corresponding to that of a single photon is added, i.e.

$$\tilde{A}(\omega_n) = (\hbar\omega/\delta_\omega)^{1/2} \exp(2\pi i r_n), \quad (3.4)$$

where  $\hbar$  is Planck's reduced constant,  $\delta_\omega$  is the frequency grid spacing and  $r_n$  is a random number between 0 and 1.

To illustrate the significance of the noise floor as compared to an input pulse without noise, consider figure 3.3. As expected the limit of numerical precision can be seen at around  $10^{-15}$ , and importantly the quantum noise is well above this level.

To further stress the importance of including noise, we will for a moment consider the problem that will be modelled in a later chapter, namely that of supercontinuum generation in a tapered chalcogenide fiber. Due to the strong nonlinearity of chalcogenide and the reinforcement of nonlinear effects by the tapering, small fluctuations in the input pulse can induce huge fluctuations in the end of the fiber. This is exemplified in figure 3.4, in which we see the result of five identical simulations but with different seeds for the random number generator producing the quantum noise. An obvious way to deal with this large variance is to perform an average over an ensemble of differently seeded fields after propagation. This gives rise to the ensemble average of the previous five simulations also shown on figure 3.4. As seen here many of the single shot simulations show dips of magnitude up to 40-50 dBm caused by random variation, whereas the ensemble average of just these five propagated fields virtually removes all random dips of more than 10 dBm. In numerical work described in a later chapter we will tend to use even larger ensembles consisting of 10-20 propagated fields.

### 3.4 Solving the MM-GNLSE by numerical integration

In order to solve a differential equation such as the GNLSE (and thereby of course NLS and MM-GNLSE) there are two main approaches in the literature, namely split-step methods and

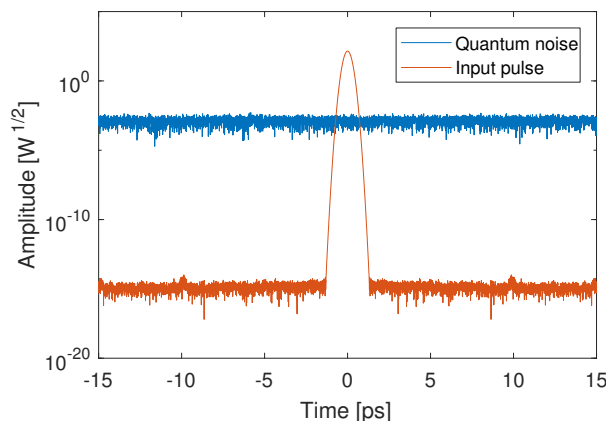


**Figure 3.3:** Quantum noise given by the one-photon-per-mode noise source compared to a noiseless input pulse.

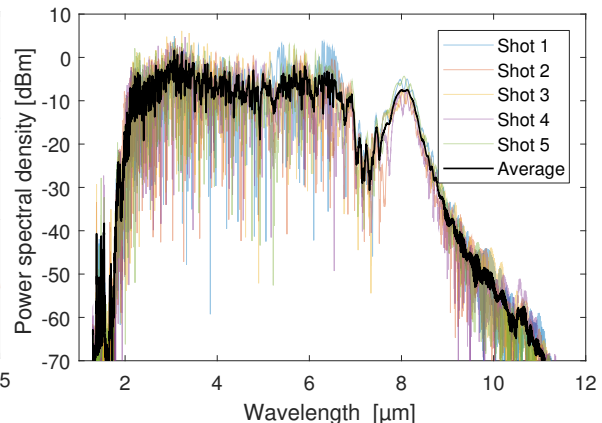


**Figure 3.4:** Ensemble of five otherwise identical simulations but with different noise seeds and the ensemble average.

interaction picture methods. Perhaps the most straightforward method is to Fourier transform the GNLSE to get rid of temporal differential operators, and then simply use a numerical integration scheme to solve the resulting ordinary differential equation (ODE). Such a method is very inefficient in comparison to the above-mentioned approaches, since the linear part can be accounted for analytically rather than numerically.

The split-step method works by solving the linear and nonlinear parts of the GNLSE separately. The linear part consists of dispersion and linear loss and it can be solved analytically, while the nonlinear part must be solved numerically. It is then possible to approximate the solution to the GNLSE by alternately using the solutions from either part to step forward.

The simple split-step method is rather inefficient [18], but several improvements have been suggested, such as the symmetric split-step Blow-Wood RK2 and RK4 method [19] or the implicit symmetric split-step method proposed by Agrawal [18, 7]. The acronym RK stands for Runge-Kutta, while the number after RK refers to the convergence order of the method, something that is defined and studied in chapter 5.

Interaction picture (IP) methods transform the field envelope by multiplication with an exponential function, whereby the GNLSE no longer have two separate parts, but can be expressed by a single term on the right-hand side [17, 3, 18]. The benefit of doing so is that the linear part is accounted for by the transformation itself, and the numerical integration scheme only has to handle the nonlinear part in principle. This idea is a bit similar to the split-step approach, and indeed both techniques can be designed to have the same convergence rate, namely the convergence rate given by the numerical integration. The interaction picture method used throughout this thesis, referred to as the DPIP method (Dormand-Prince Interaction Picture), was developed during the project, and in chapter 5 it is shown to have a high order of convergence while being computationally more efficient than other methods, i.e. better performance when considering convergence versus runtime.

### 3.4.1 Interaction picture methods

The transformation of the field envelope,  $A(z, t)$ , into the interaction picture is defined as

$$A_I = e^{-(z-z')\hat{D}}A, \quad (3.5)$$

where  $A_I$  is the interaction picture representation of the field envelope, and  $z'$  is a separation distance that we can freely choose. If we differentiate this expression and insert the GNLSE,  $\partial_z A = (\hat{D} + \hat{N})A$ , we find

$$\begin{aligned} \partial_z A_I &= -\hat{D}e^{-(z-z')\hat{D}}A + e^{-(z-z')\hat{D}}(\hat{D} + \hat{N})A \\ &= e^{-(z-z')\hat{D}}\hat{N}A = e^{-(z-z')\hat{D}}\hat{N}e^{(z-z')\hat{D}}A_I \Leftrightarrow \partial_z A_I = \hat{N}_I A_I, \end{aligned} \quad (3.6)$$

in which  $\hat{N}_I$  is the interaction picture representation of the nonlinear operator.

The question is now what to choose as the separation distance  $z'$ . Some authors [17, 3] simply choose  $z' = 0$ , but it can also be chosen based on the numerical integration scheme applied. A popular numerical integration scheme is the RK4, also known as the classical Runge-Kutta method, where an iterative solution to  $\partial_z y = f(z, y)$  is given by

$$y(z+h) = y(z) + \frac{h}{6}(k_1 + 2k_2 + 2k_3 + k_4), \quad (3.7)$$

where

$$k_1 = f(z, y(z)), \quad k_2 = f\left(z + \frac{h}{2}, y(z) + \frac{h}{2}k_1\right) \quad (3.8)$$

$$k_3 = f\left(z + \frac{h}{2}, y(z) + \frac{h}{2}k_2\right), \quad k_4 = f(z+h, y(z) + hk_3). \quad (3.9)$$

If we apply the RK4 method to (3.6), we will by default have to use 16 FFTs [18]: 2 for  $A_I$ , 2 for transforming to and from the interaction picture, 2 for  $k_1$  and  $k_4$ , respectively, and 4 for  $k_2$  and  $k_3$ , respectively. However, since  $k_2$  and  $k_3$  are evaluated at the step midpoint, we can simply choose  $z' = z + h/2$ , such that the interaction picture and normal picture coincide at this point, eliminating the need of any FFTs, thus yielding a total number of FFTs of 8. This trick was first proposed in [20] and later applied to nonlinear optics in [18], where the method was coined RK4IP.

Other choices of  $z'$  will be advantageous for other numerical integration schemes. For the DPIP method developed during this project that builds upon the Dormand-Prince Runge-Kutta scheme, and is specified in appendix A, an optimal choice of  $z'$  is to have it a whole step size ahead. In short, the scheme has two function evaluations a whole step size ahead, and by choosing  $z' = z + h$ , we can similarly eliminate the FFTs in those two evaluations, and then additionally remove the need to transform back from the interaction picture before the next step, because the interaction and normal picture coincides at  $z + h$  as a consequence of the choice. Like the RK4IP this also saves 8 FFTs, but it has a higher order of convergence as we shall see in chapter 5, where a brief comparison of the schemes is given. For this reason the DPIP method is used throughout the thesis with all presented simulation results of fiber propagation relying on it.

### 3.4.2 Adaptive step size control

Computation time can be greatly reduced by using a non-fixed step size that is adjusted based on an estimation of the error that the step will introduce. This technique is referred to as adaptive step size control. There are many possible procedures to adjust the step size given an error estimation. A simple procedure is to reject a step if the corresponding error is above a chosen tolerance, and then redoing the step with half the step size – conversely the step size is doubled if the estimated error is well below the tolerance. The step size control employed in the solver developed during this project follows the outline of [21] and is a bit more elaborate but similar to the procedure just described.

The error estimation of a step can be inferred from considering a conserved quantity such as the energy or photon number, which are both studied in section 5.3. However, as is shown in section 5.3, the presence of attenuation during propagation in a fiber will cause those quantities to be non-conserved. A possible remedy is discussed in section 5.3, but a more general approach is to use an integration scheme with an embedded error estimator. The embedded error is usually found as the difference between two solutions of different order both provided by the scheme. As mentioned previously the DPIP method builds upon the Dormand-Prince scheme that unlike RK4 has an embedded error estimator, which is another benefit of the DPIP method compared to the RK4IP method. See appendix A for more details on the DPIP method and its embedded error estimator.

## 3.5 Modelling tapered fibers

Conceptually, it is simple to extend the description of pulse propagation in plain fibers to tapered fibers, because the only difference is that the linear operator and mode functions (hence overlap integrals) get a dependence on the propagation distance,  $z$ . This is easy to account for in a numerical implementation. The non-trivial problems related to modelling tapered fibers is how the down and up taper segments should be appropriately discretized, investigated in section 7.1, and how the fiber dimensions should vary along those segments. We will address the latter problem here.

It is often assumed that the pitch is proportional to the outer fiber diameter, and since the outer diameter is assumed to vary linearly along the tapered regions so too will the pitch. However, upon looking at measured dimensions of a tapered fiber [22], it was found that the pitch after the down taper can be as much as 10 % larger than expected from this linear dependence on the outer diameter. Hence, this assumption of exact proportionality to the outer diameter should be abandoned.

In this section a simple model to vary the pitch and hole diameter along the down and up taper with the constraint that the hole-to-pitch ratio varies linearly along the down taper, while not relying on the proportionality assumption of the pitch and outer diameter. This implies that both hole diameter and pitch will vary nonlinearly. The model may be relevant when considering tapered fibers with large reductions of the hole-to-pitch ratio along the down taper, because it may be more accurate than the proportionality assumption, but note that there is no experimental evidence for this – the idea to have the aforementioned constraint is based on speculation alone. Indeed the model was developed early on in the project, where such large reductions of the hole-to-pitch ratio were considered, but the specific fibers that have subsequently become the main focus of the simulations in the later chapters almost have constant

hole-to-pitch ratio, in which case either of the three methods documented in the following will produce very similar results.

**Derivation.** We consider the tapering of a fiber in which the outer diameter is shrunk linearly over a normalised distance  $x$  such that  $x = 0$  corresponds to just before the tapering, and  $x = 1$  corresponds to right after the tapering. Let  $\Lambda_0$  and  $d_0$  be the pitch and hole diameter before tapering, and let  $\Lambda_w$  and  $d_w$  be the corresponding values in the fiber waist after tapering. The most straight-forward way to have the pitch,  $\Lambda$ , and hole diameter,  $d$ , vary along the down taper is of course linearly,

$$\Lambda(x) = (1 - x)\Lambda_0 + x\Lambda_w, \quad d(x) = (1 - x)d_0 + xd_w. \quad (3.10)$$

With those definitions of  $\Lambda$  and  $d$ , the hole-to-pitch ratio,  $d/p$ , is not linear. To impose linearity of this ratio we set the constraint that  $d/\Lambda = (1-x)d_0/\Lambda_0 + xd_w/\Lambda_w$ . An easy way to incorporate this constraint is to have the pitch follow the linear definition of (3.10), and then define the hole diameter from the constraint, i.e.

$$d(x) = [(1 - x)\Lambda_0 + x\Lambda_w] \left[ (1 - x)\frac{d_0}{\Lambda_0} + x\frac{d_w}{\Lambda_w} \right]. \quad (3.11)$$

Now rather than keeping the pitch linear and removing the offset from the constraint by adjusting the hole diameter alone, we might as well split this offset, call it  $h$ , equally between the pitch and hole diameter, namely

$$\Lambda(x) = (1 - x)\Lambda_0 + x\Lambda_w + h(x), \quad d(x) = (1 - x)d_0 + xd_w - h(x), \quad (3.12)$$

which when solved with respect to the constraint gives the following solution for  $h$

$$h(x) = \frac{(x - 1)x(\Lambda_0 - \Lambda_w)(\Lambda_0d_w - d_0\Lambda_w)}{(xd_w + \Lambda_w)\Lambda_0 + (\Lambda_w - x\Lambda_w)d_0}. \quad (3.13)$$

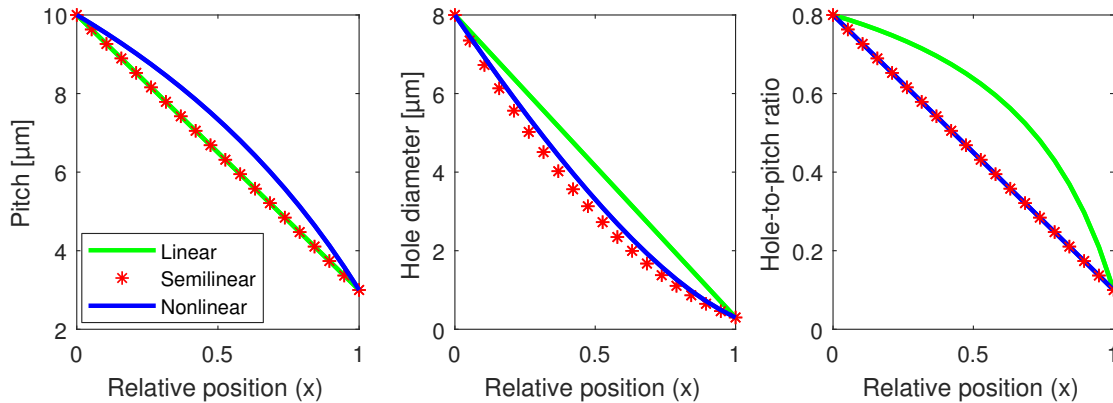


**Figure 3.5:** Different ways to vary pitch and hole diameter in a tapered section.

**Comparison of methods.** In figure 3.5 we compare the completely linear method (3.10), the method in which only the pitch is linear (3.11), referred to as semilinear in the figure, and finally the method where the constraint offset is split between the pitch and hole diameter

(3.12), referred to as nonlinear in the figure. As expected the linear variation of pitch and hole diameter leads to a nonlinear hole-to-pitch ratio, whereas the two other methods have linear hole-to-pitch ratio. For the method (3.12), we see that both the pitch and hole diameter varies nonlinearly due to  $h$ . In the semilinear case the hole diameter is even further from linear variation, because the constraint offset is not split.

# CHAPTER 4

## Nonlinear effects in optical fibers

We will now explore some general nonlinear effects. Some of those effects are important to achieving a supercontinuum (SC) in a fiber, while other effects are documented as a means of testing the code against well-known phenomena, since all solutions in the following are computed with the solver that has been developed during the project.

Several of the solutions presented in this section are not based on frequency-dependent linear and nonlinear operators, and for those solutions the carrier wavelength is chosen freely to be 4  $\mu\text{m}$ , which seems fitting as the rest of the thesis is concerned with mid-IR.

### 4.1 Kerr nonlinearity and group velocity dispersion

Returning to the NLS in the most simple form (2.11), which only includes a single linear term, governing the group velocity dispersion (GVD), and a cubic nonlinear term associated with the Kerr effect. We will now consider each of these terms separately. Solving the NLS with the Kerr nonlinearity alone and an initial sech-shaped pulse, the solution yields a pulse that remains constant in the time domain, because there is no dispersion, however in the frequency domain the effect of self-phase modulation (SPM) occurs as a direct result of the Kerr nonlinearity, causing a chirp that can be seen as the spectral broadening to the left in figure 4.1. Conversely, when there is no Kerr nonlinearity and only GVD, the pulse is seen to broaden temporally, while maintaining its spectral pulse width to the right in figure 4.1.

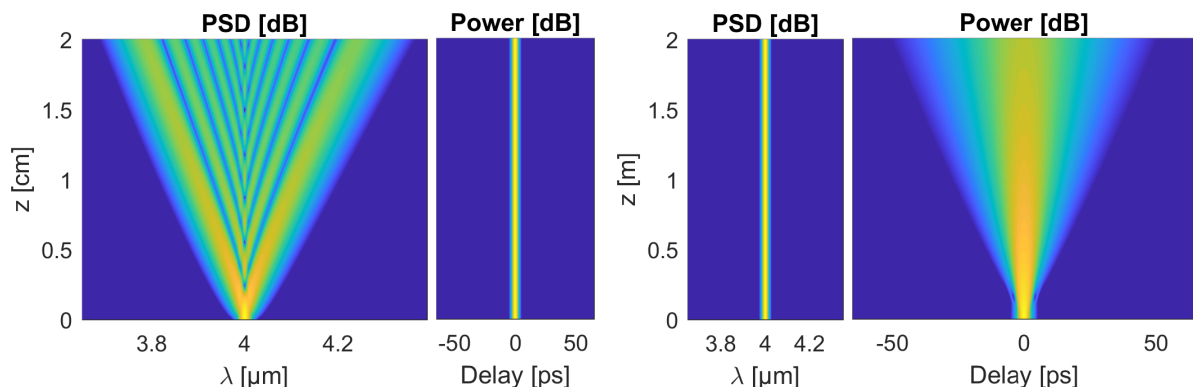


**Figure 4.1:** Spectral and temporal broadening in the NLS. Two leftmost plots show a solution using only the nonlinear part, the Kerr effect, resulting in SPM, while the two rightmost plots show a solution using only the linear part resulting in dispersion. Parameters used are  $\gamma = 0.1 \text{ (Wm)}^{-1}$ ,  $P = 20 \text{ kW}$  (left);  $\beta_2 = -10 \text{ ps}^2/\text{m}$ ,  $P = 5 \text{ kW}$  (right) and  $T_0 = 1 \text{ ps}$  (both).

## 4.2 Solitons

If we combine the two effects above, the chirp from SPM can be set to exactly counterbalance the dispersion, which leads to solutions known as solitons. This behaviour can be described by the NLSE with only second-order dispersion,

$$\partial_z A(z, t) = -i \frac{\beta_2}{2} \partial_t^2 A + i \gamma |A|^2 A, \quad \beta_2 < 0, \quad (4.1)$$

in which the dispersion is said to be anomalous, because the GVD is negative. If we then assume the initial condition to be  $A(0, t) = \sqrt{P_0} \text{sech}(T/T_0)$ , where  $P_0$  is the peak power, the integer  $N$  is the soliton order, or soliton number, and  $T_0$  is the pulse width, the solutions to (4.1) will be soliton solutions. The soliton order is given by  $N^2 = \gamma P_0 T_0^2 / |\beta_2|$ , and since it must be an integer, this condition sets constraints on the parameters of the pulse and the GVD of the fiber.

The solution for  $N = 1$  is called the fundamental soliton and it has a particularly simple form [7]

$$A(z, t) = \sqrt{P_0} \text{sech} \left( \frac{t}{T_0} \right) \exp \left( i \frac{|\beta_2|}{2 T_0^2} z \right). \quad (4.2)$$

The power of the fundamental soliton,  $|A|^2$ , has no  $z$ -dependence, see figure 4.2(b), nor does the power spectral density (PSD), see figure 4.2(a).

Higher-order solitons,  $N > 1$ , do have  $z$ -dependence in the power and PSD, but the higher-order solitons are all periodic with the same period  $z' = \frac{\pi}{2} \frac{T_0^2}{|\beta_2|}$  [7]. Closed form exact solutions for some higher-order solitons also exists, an example of which we will see in the next chapter. A simulation of a eight-order soliton is shown in figure 4.3. The propagation length has been set to twice that of the period  $z'$  above, which is indeed seen to give two periods in the simulation.

A test of the time window boundaries are shown on figure 4.2(c), where the reference frame is set to move faster than the group velocity (GV) of the soliton resulting in an increasing delay of the soliton. When the soliton reaches the right boundary of the time window, the periodic boundary conditions of the FFT and IFFT algorithms that are used in the solver causes the soliton to reappear in the opposing side of the time window.

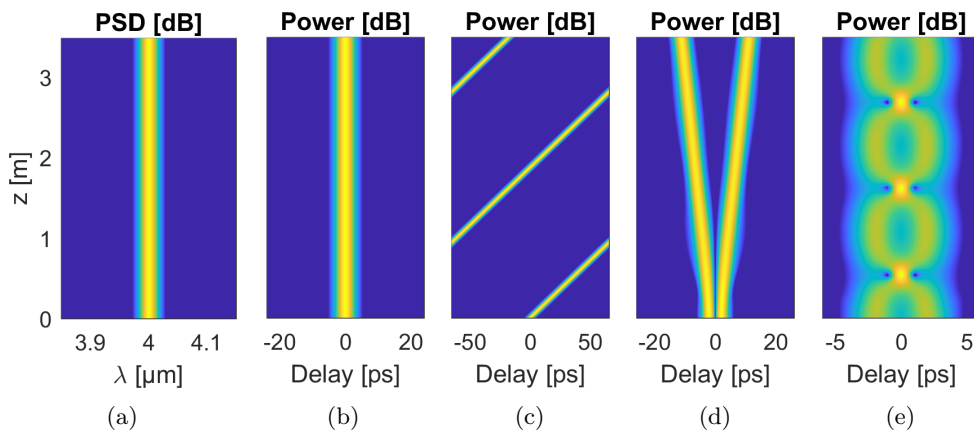


**Figure 4.2:** Fundamental soliton(s) with parameters  $\beta_2 = -10 \text{ ps}^2 \text{ m}^{-1}$ ,  $\gamma = 0.1 \text{ (Wm)}^{-1}$ ,  $T_0 = 1 \text{ ps}$  and  $P = 100 \text{ W}$ . All plots share the same second axis. (a) Soliton in frequency domain, (b) Soliton in time domain, (c) Test of time window, (d) Soliton repulsion, (e) Soliton collision.

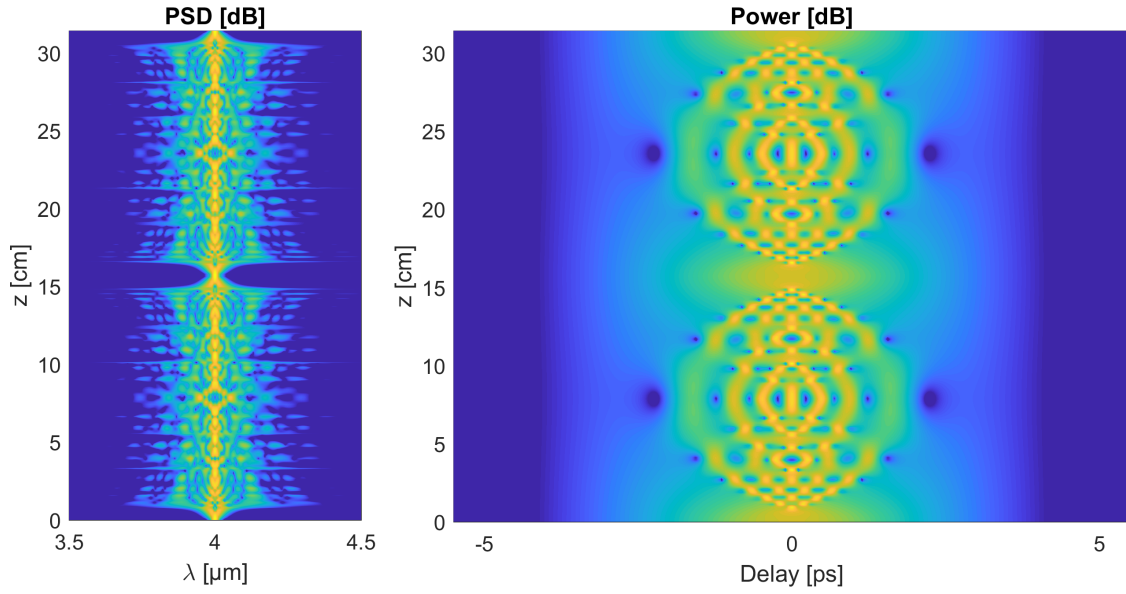


**Figure 4.3:** A eight-order soliton solution in terms of PSD (left) and power (right) during propagation of  $2z'$ . Parameters used are the same as in figure 4.2, except for the power now being 6400 W.

In figure 4.2(d) and 4.2(e), we see simulations of two solitons displaced slightly in time and with a half period phase difference (d) and equal phase (e). The phase difference causes a sort of repulsion between the solitons leading to increasing temporal displacement between them, whereas a repeating collision occurs for the phase matched solitons.

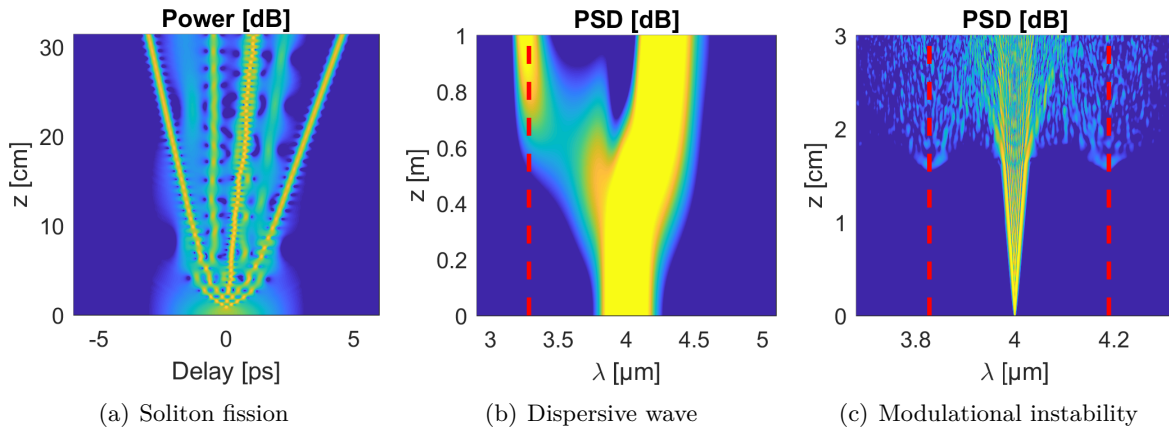


**Figure 4.4:** Simulation of sech-shaped pulses with parameters: (a)  $\beta_2 = -10 \text{ ps}^2 \text{ m}^{-1}$ ,  $\gamma = 0.1 \text{ (Wm)}^{-1}$ ,  $T_0 = 1 \text{ ps}$ ,  $\beta_3 = 0.1 \text{ ps}^3 \text{ m}^{-1}$  and  $P = 6400 \text{ W}$  ( $N = 8$ ); (b)  $\beta_2 = -2 \cdot 10^{-3} \text{ ps}^2 \text{ m}^{-1}$ ,  $\beta_3 = 0.1 \cdot 10^{-3} \text{ ps}^3 \text{ m}^{-1}$ ,  $\gamma = 0.025 \text{ (Wm)}^{-1}$ ,  $T_0 = 50 \text{ fs}$ ,  $P = 200 \text{ W}$  ( $N = 2.5$ ); (c)  $\beta_2 = -10 \text{ ps}^2 \text{ m}^{-1}$ ,  $\gamma = 0.1 \text{ (Wm)}^{-1}$ ,  $T_0 = 10 \text{ ps}$ ,  $P = 22.65 \text{ kW}$  ( $N = 150$ ).

Figure 4.4(a) shows a phenomenon known as soliton fission, where  $\beta_3 \neq 0$  resulting in the pulse splitting into multiple solitons. The associated PSD has been omitted, as the fission is most evident in the time-domain.

On figure 4.4(b) we see the formation of a so-called dispersive wave, which is a consequence of the initial soliton being redshifted, but not necessarily due to delayed Raman response, with

the excess energy being siphoned into the generation of the dispersive wave. From theory a prediction of the frequency,  $\Omega$ , at which the dispersive wave is expected to be generated is given by [7]

$$\beta_2 \Omega^2 + \frac{\beta_3}{3} \Omega^3 - \gamma P_s = 0, \quad (4.3)$$

where  $P_s$  is the peak power of the redshifted soliton, taken to be equal to that of the input pulse as an approximation, and the dispersion parameters  $\beta_2$  and  $\beta_3$  are at the frequency of the soliton, not the frequency  $\omega_0$  of the input pulse. For the simulation result shown on the figure, two constant values for  $\beta_2$  and  $\beta_3$  were used, and using a Taylor series the corresponding dispersion parameters at the soliton wavelength estimated to be  $4.3 \mu\text{m}$  can be found. The computed value of  $\Omega$  has been indicated by the dashed line in the figure, which is seen to agree quite well with the simulation result.

Another effect for which we can also make an analytical prediction is one known as modulational instability (MI), where a small perturbation to a periodic optical field is built up during propagation due to nonlinearity, which leads to spectral sidebands characterised by two frequencies of maximal gain given by [7]

$$\Omega = \omega_0 \pm 2\pi \sqrt{\frac{2\gamma P_0}{|\beta_2|}}. \quad (4.4)$$

Those two predicted frequencies are indicated by the dashed lines on figure 4.4(c), where MI is seen to occur after about 1.5 cm of propagation. The predictions seem to be consistent with the sidebands found in the simulation given that the dashed lines pass right through what appears to be the center of the sidebands. After the breakup of the initial pulse, the bandwidth is seen to be significantly larger, and for this reason MI is often used for SC generation.

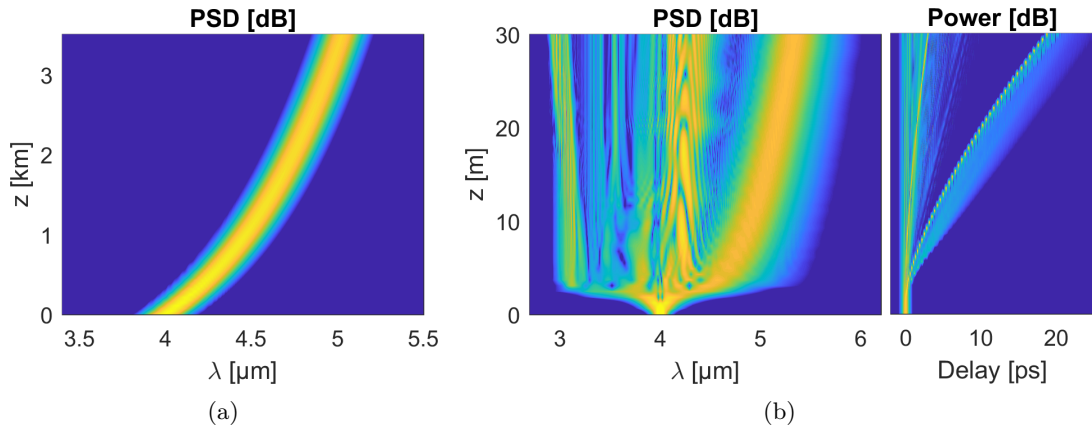


**Figure 4.5:** Redshifting soliton with parameters:  $f_R = 0.18$  and (a)  $\beta_2 = -0.5 \cdot 10^{-3} \text{ps}^2 \text{m}^{-1}$ ,  $\gamma = 0.025 (\text{Wm})^{-1}$ ,  $T_0 = 50 \text{fs}$ ,  $P = 8 \text{W}$ ; (b)  $\beta_2 = -2 \cdot 10^{-3} \text{ps}^2 \text{m}^{-1}$ ,  $\beta_3 = 0.1 \cdot 10^{-3} \text{ps}^3 \text{m}^{-1}$ ,  $\gamma = 0.025 (\text{Wm})^{-1}$ ,  $T_0 = 200 \text{fs}$  and  $P = 100 \text{W}$ .

### 4.3 Delayed Raman response

The final nonlinear effect we will consider in this chapter is the delayed Raman response described by the GNLSE, eq. (2.13). The Raman effect is of great importance to the SC generation

simulated later. The response function used is given by (2.14), with the delayed Raman response function being an analytical approximation often used for silica [7]

$$h_R(t) = \frac{\tau_1^2 + \tau_2^2}{\tau_1 \tau_2^2} \exp(-t/\tau_2) \sin(t/\tau_1), \quad (4.5)$$

where  $\tau_1 = 12.2$  fs,  $\tau_2 = 32$  fs and  $h_R(t) = 0$  for  $t < 0$ .

In figure 4.5(a) we see the effect of the delayed Raman response to a low-power fundamental soliton by a gradual redshift over a relatively large propagation distance. In figure 4.5(b) the input pulse is sech-shaped, but the parameters do not correspond to a fundamental soliton,  $N = 7.1$ , which in addition to the higher power quickly causes a breakup of the input pulse leading to generation of a supercontinuum.

# CHAPTER 5

## Numerical Analysis

A numerical method is said to be consistent if it has an order  $p$  greater than 0 such that the local truncation error of the  $n$ th step is bounded by  $\delta_n^h = O(h^{p+1})$ , where  $h$  is a discretization parameter, e.g. step size [23]. Consistency and stability are the two necessary and sufficient conditions for convergence. Stability analysis is out of the scope of this thesis, but the numerical methods used throughout will now be investigated for consistency and convergence with stability being assumed.

### 5.1 Convergence behaviour for fiber modelling

As described previously, the fiber is modelled with COMSOL from which we get the propagation constants as eigenvalues and mode functions as eigenvectors. One obvious way to validate the results from COMSOL would be to compare them with analytical or experimental values. Unfortunately, no analytical solutions exist for photonic crystal fibers. As for comparing with experimental data, we will do exactly that in the chapter on experiments. For now we will assess the modelling from a numerical perspective.

Firstly, the discretization resolution is addressed. The geometry representing the fiber is discretized into a mesh of elements, in our case triangles, which was shown earlier. The meshing of the geometry is handled adaptively by COMSOL, but a choice regarding the maximum size

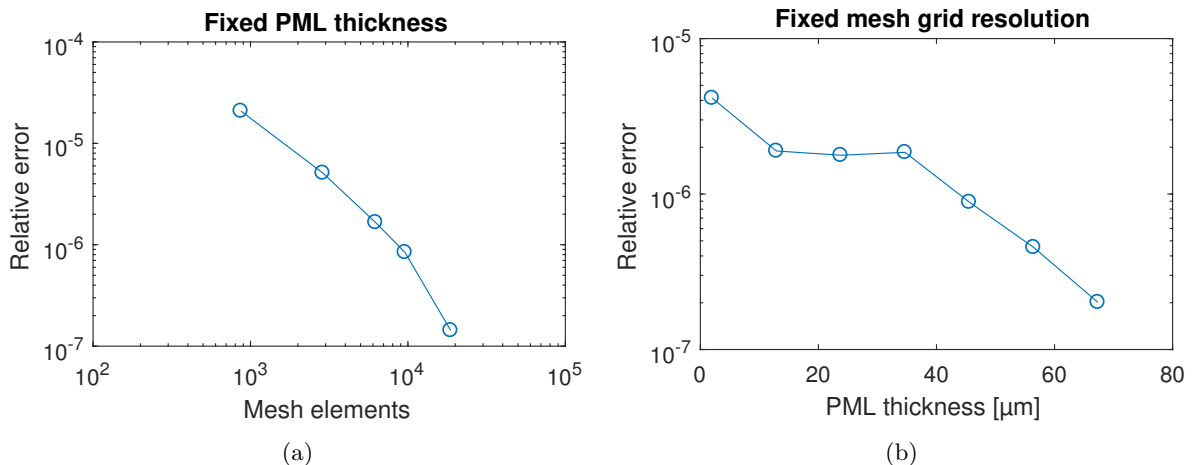


**Figure 5.1:** Convergence of the eigenvalue obtained from COMSOL. The relative errors are computed with respect to the most precise computation performed. To the left the eigenvalue converges as a function of the number of mesh elements with a fixed PML thickness that was sufficiently large as to not limit the convergence. To the right the eigenvalue is seen to converge as the PML thickness is increased, while the mesh grid is kept at a constant resolution high enough as to not limit convergence.

of an element has to be made, which then determines the total number of mesh elements.

To verify that the solutions converge, we vary the mesh resolution and compare resulting eigenvalues against the most precise solution computed, i.e. the solution with highest resolution. We define the eigenvalue error as the relative deviation to the eigenvalue of this most precise computation. For an arbitrary choice of frequency<sup>1</sup>, 140 THz, and with other fiber parameters corresponding to the fiber that is experimentally investigated later, the eigenvalue errors as a function of mesh elements are shown in figure 5.1(a).

The convergence rate is seen to be superlinear, and with more than  $10^4$  mesh elements the relative error is within a tolerance that is also used when simulating fiber propagation.

Next the boundary condition is verified to be sufficient. The reader is reminded that we use the perfectly matched layer (PML) as a boundary condition. For numerical efficiency we want the PML to be as thin as possible, but the question remains how thin. This is something that was investigated by simply varying the PML thickness while keeping the mesh resolution constant such that the number of elements per area in the core is the same regardless of the PML thickness. Since the PML truncates the mode functions that decrease exponentially with the distance from the fiber core, the error arising from having a too thin PML will very quickly tend to zero. This is indeed seen in the figure 5.1(b), where the linear curve on the semilogarithmic plot indicates an exponentially decreasing error. A PML with a thickness of 40  $\mu\text{m}$  or more is seen to comply with our usual tolerance.

## 5.2 Validation and performance of GNLSE solver

First we consider the problem of simulating a higher-order soliton and afterwards a more demanding simulation of supercontinuum in a chalcogenide fiber – for now we do not concern ourselves with the physics of supercontinuum, so a thorough account of the parameters and input data used here is given in a later chapter.

### 5.2.1 Reproducing an analytical second order soliton solution

As described previously the chirp from self-phase modulation can exactly counterbalance the effect of anomalous dispersion giving rise to solitons. The solitons were found as solutions to the NLSE with an integer  $N$  being the order.

In case of the fundamental soliton, the power  $|A|^2$  has no  $z$ -dependence, and thus it is not very useful for validating an implementation of a solver for numerically integrating the NLS.

For  $N = 2$  there is also a closed form solution [7]

$$A(z, t) = 2\sqrt{P_0} \frac{\left[ \cosh\left(3\frac{t}{T_0}\right) + 3 \exp\left(4iz\frac{|\beta_2|}{T_0^2}\right) \cosh\left(\frac{t}{T_0}\right) \right] \exp\left(i\frac{|\beta_2|z}{2T_0^2}\right)}{\left[ \cosh\left(4\frac{t}{T_0}\right) + 4 \cosh\left(2\frac{t}{T_0}\right) + 3 \cos\left(4\frac{|\beta_2|}{T_0^2}z\right) \right]}. \quad (5.1)$$

The second-order soliton does not pertain its shape over  $z$ , rather it is periodic as other higher-order solitons with period  $z' = \frac{\pi T_0^2}{2|\beta_2|}$ .

A closed form solution also exists for  $N = 3$  [24], but as it is even more lengthy it will not be listed here, nor will it be used for validation purposes or numerical convergence testing, because the  $N = 2$  soliton has the same nonlinear behaviour and is thus sufficient.

The expression (5.1) is plotted on figure 5.2(a), where five periods are seen to occur.

---

<sup>1</sup>Convergence behaviour should be the same at all frequencies for which there exist propagating modes

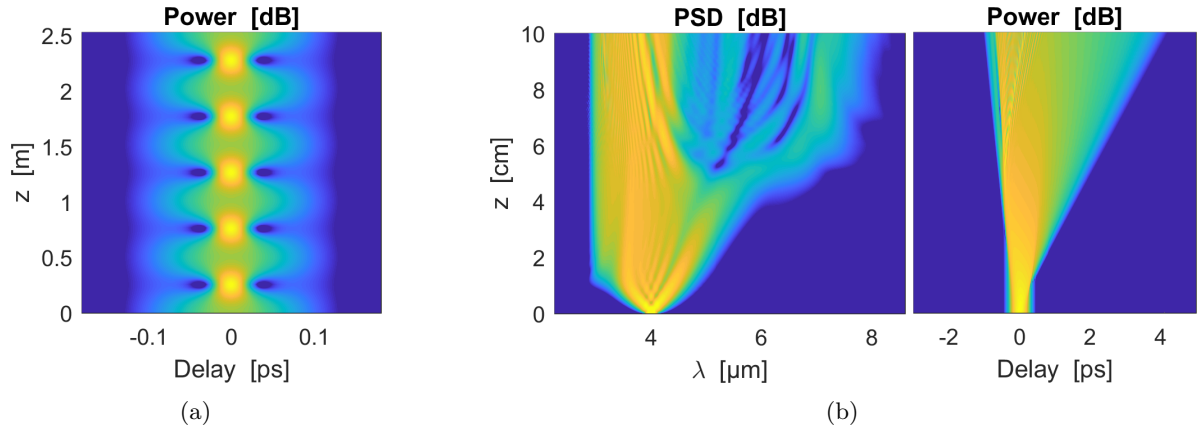


**Figure 5.2:** Solutions to the test problems. (a) Second-order soliton solution to the NLSE based on parameters  $T_0 = 60$  fs,  $\beta_2 = -0.01$  ps<sup>2</sup>/m and  $P = 1.2$  kW. (b) Supercontinuum generation in a chalcogenide fiber studied later. The equation solved corresponds to the GNLSE but with a frequency-dependent mode area and without delayed Raman response and attenuation. The ZDW for the fiber is at 5  $\mu\text{m}$ .

### 5.2.1.1 Convergence rates of interaction picture Runge-Kutta schemes

We shall now compare the different interaction picture (IP) Runge-Kutta (RK) based methods mentioned in chapter 3 when simulating the second-order soliton, namely the RK4IP and DPIP methods, the latter being the method that was developed during the project and is used throughout the thesis – it is specified in appendix A. Along with those two solutions, an alternative method based on the RK-Fehlberg scheme using the same IP separation distance,  $z'$ , as the RK4IP method, i.e. half a step size. The RK-Fehlberg method is expected to be a fifth order method, hence higher order than the RK4IP, but does not allow advantageous choices of the IP separation distance as the RK4IP and DPIP methods do, and is thus expected to be less computational efficient (i.e. the performance when considering time).

The error of a solution is evaluated as

$$Er = \left( \sum |A_{\text{ana}} - A_{\text{num}}| \right) \left( \sum |A_{\text{ana}}| \right)^{-1}, \quad (5.2)$$

where  $A_{\text{ana}}$  is the analytical field envelope and  $A_{\text{num}}$  is the numerically computed field envelope.

In figure 5.3 we see the convergence rates of the methods, where we not only consider the convergence with respect to computational steps but also computational time to account for the fact that the stages of the higher-order RK schemes are more demanding, and to see whether they truly are more efficient. The DPIP method is seen to have the highest convergence rate, an order close to 6, for the considered test problem. When considering computational efficiency, the RK4IP has a head start as seen in figure 5.3(b) given that it is less demanding, but the DPIP quickly becomes more efficient, when the problem gets larger and the run time increases.

## 5.2.2 Convergence rate when simulating supercontinuum generation

We now want to test convergence when simulating the more complex problem of SC generation with frequency-dependent nonlinear coefficient and attenuation, as well as delayed Raman re-

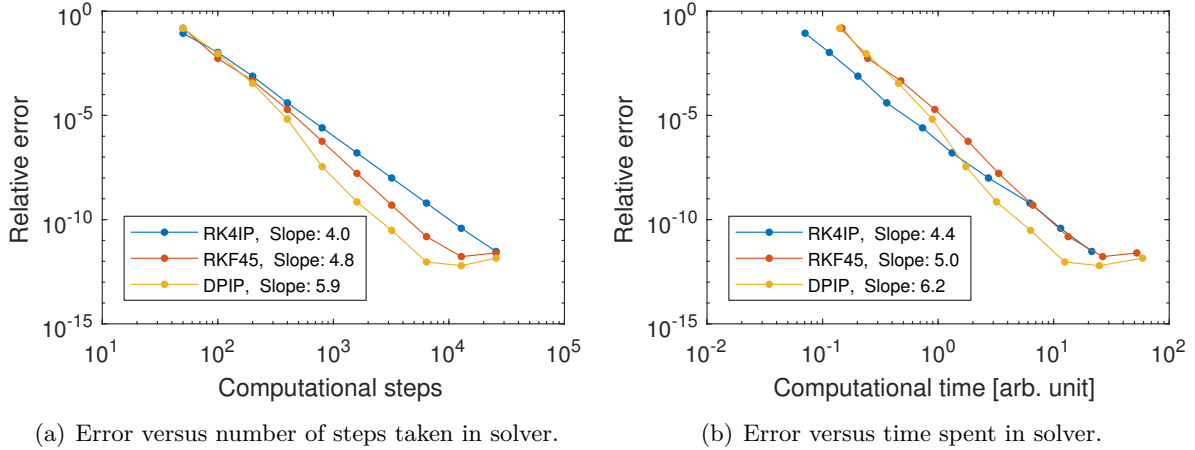


**Figure 5.3:** Comparison of convergence rate between Runge-Kutta methods when computing a second order soliton solution for which we can use the analytical solution as reference. The slope value in the legends refer to the slope of a linear fit describing the trends before reaching the limit set by numerical precision  $10^{-12}$ .

sponse. We shall use parameters that correspond to the chalcogenide fiber simulated in later chapters – the exact parameters that are used will be described in chapter 7, for now we will simply consider the convergence rate when using the full MM-GNLSE.

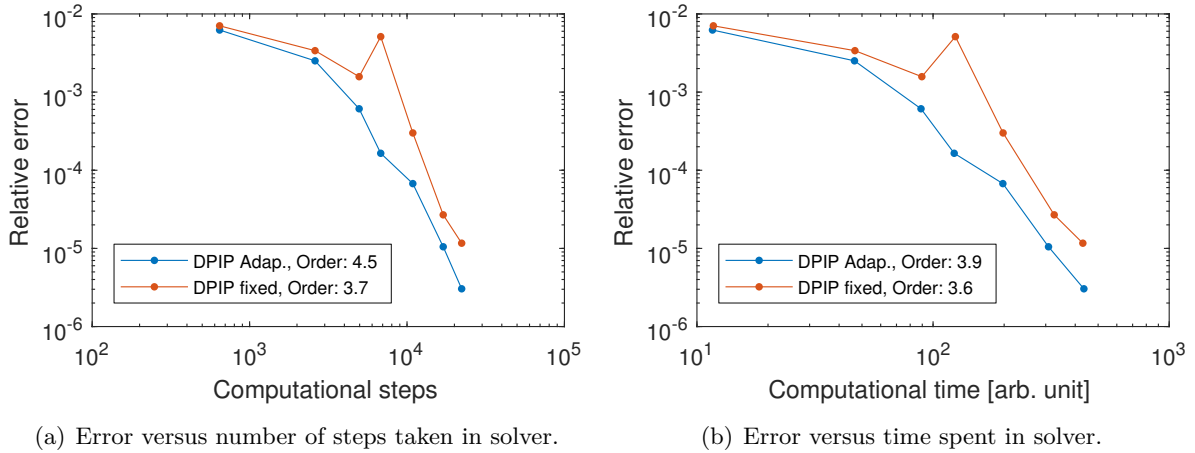


**Figure 5.4:** Comparison of convergence rates of the DPIP method with and without adaptive step size control when simulating SC generation in a chalcogenide fiber. The slope value in the legends refer to the slope of a linear fit describing the trends before reaching the limit set by numerical precision  $10^{-12}$ .

On figure 5.4 we see the convergence rates when using the DPIP with and without the adaptive step size control described in 3.4.2. The more complex problem simulated here yields a lower convergence order apparently, but still close to an order of 4, which is the minimal convergence rate expected of a Dormand-Prince scheme. The adaptive step size control is not expected to increase the convergence rate, which is also seen to be the case on the figure. It does however give a constant factor of better performance as evidenced by the almost parallel but downward shifted blue curves of figure 5.4.

## 5.3 Conserved quantities

The simple NLSE (2.11) can be shown to conserve energy, but due to the shock term  $\tau\partial_t$  in the GNLSE and MM-GNLSE, those two equations do not conserve energy, but instead the photon number given by [19]

$$P_N(z) = \int_{-\infty}^{\infty} \frac{|\tilde{A}(z, \omega)|^2}{\omega} d\omega. \quad (5.3)$$

Conserved quantities are very useful when studying numerical convergence, because it gives a clear indication of when a solution is sufficiently converged. Furthermore, they also form a good validation check, as an implementation is conclusively incorrect if solutions are not found to converge towards invariance of the quantities when increasing the precision (i.e. a discretization parameter).

We shall now see if the implementation developed during this project does indeed converge towards invariance when a quantity is expected to be conserved. Additionally, we will briefly consider an example, where none of above the quantities are conserved, namely when loss is introduced.

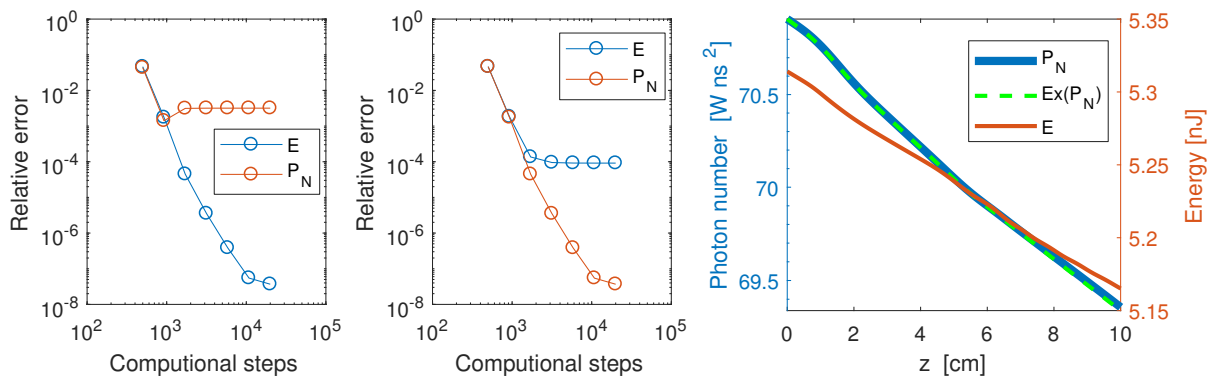


**Figure 5.5:** Convergence towards invariance of energy in the NLSE (left) and photon number in the GNLSE (mid), and a plot showing decrease of both energy and photon number in the presence of attenuation (right) with the decrease of latter quantity being predictable.

**Energy conservation.** We first simulate 5 cm of propagation with the NLSE using a Gaussian input pulse  $A(t) = \sqrt{P} \exp(-t^2/T_0^2)$  with  $T_0 = 1$  ps,  $P = 20$  kW,  $\beta_2 = 10$  ps<sup>2</sup>/m and  $\gamma = 0.5$  (Wm)<sup>-11</sup>. The solution shows both SPM and dispersion in a similar fashion to what was seen in the beginning of chapter 4. We then evaluate the energy by integration of  $|A(t)|^2$  at the end of propagation and compare it to the initial energy. The relative error when using an increasing number of steps along the fiber is shown as the blue curve,  $E$  for energy, in the left side of figure 5.5 with the similarly defined relative error for the photon number, denoted  $P_N$ . The relative error of the energy is seen to converge rapidly, at a rate that is consistent with the order of the RK scheme seen in the previous sections. Approaching a relative error of 10<sup>-8</sup>, indications of numerical precision start to appear based on the last two points. Meanwhile the photon number is seen to not be conserved as its associated relative error converges towards a non-zero value.

Given that the error is seen to converge for the energy rather than reaching a non-zero limit well above numerical precision, implies that the choice of numerical parameters outlined in section 3.2 are sufficient.

**Photon number conservation.** Using the same parameters as before but now for the GNLSE with a Raman response function equal to that given in chapter 4, we expect the photon number to be conserved due to the presence of the shock term. As before the relative error is determined when using an increasing number of steps in the propagation, and the result can be seen in the mid of figure 5.5. The convergence behaviour is the same as before, but now for the photon number instead, while the energy this time is found to converge towards a non-zero value.

**No conserved quantities.** Finally, we will again consider the problem of simulating SC generation in a chalcogenide fiber as in section 5.2.2 for which the simulation result was shown in figure 5.2(b). For this problem neither the energy nor the photon number is conserved due to attenuation,  $\alpha(\omega)$ , which can be seen by the declining red and blue curves to the right in figure 5.5. However, the following relation accurately describes how the photon number varies [21]

$$\partial_z P_N(z) = - \int_{-\infty}^{\infty} \alpha(\omega) \frac{|\tilde{A}(z, \omega)|^2}{\omega} d\omega. \quad (5.4)$$

By integrating this differential during propagation, an expected photon number can be determined. This expectation, denoted  $\text{Ex}(P_N)$ , is shown as the dashed line in the right plot of figure 5.5, where it is seen to follow the actual photon number closely, only deviating very slightly near the end of the fiber, which is due to the number of steps used to find the solution in this example is not very high, approximately 1000, and so by increasing the number of steps, a better agreement will be found.

An application of (5.4) is to use the deviation between the expected and computed photon number as an error estimator, which can then be used for adaptive step size control. This technique was found to provide a good alternative to the adaptive step size control based on the Runge-Kutta embedded error estimators mentioned in section 3.4, and is particularly useful for simpler RK schemes that do not even have built-in error estimates, such as the RK4 scheme described previously. However, the technique does not work when simulating tapered fibers, because even without any attenuation, the photon number is not conserved when the linear operator is dependent on propagation distance as is the case in a taper [3]. Therefore, the technique is not actually employed in the simulations performed in chapter 7, and the method of adaptive step size control described in chapter 3 is used instead.

# CHAPTER 6

## Experiments

---

In this chapter two experiments will be described that have been conducted during the project with the assistance of Christian R. Petersen. In both experiments a chalcogenide fiber fabricated by Selenoptics is studied. The fiber that has been measured upon has a slightly smaller core than the one we model in chapter 7, but the material composition  $\text{Ge}_{10}\text{As}_{22}\text{Se}_{68}$  is identical. Since the two fibers are so similar, we can reasonably expect that a good agreement between experiment and numerical modelling of one of the fibers will also hold for the other.

Finding agreement between modelling and experiment will be addressed in the first experiment, where we measure the dispersion in the fiber and compare with numerical results obtained from COMSOL. In the second experiment we measure the self-phase modulation (SPM) that occur in the fiber in order to estimate the nonlinear refractive index, which will be used in the following chapter on simulating SC. In this experiment the fiber dimensions are also measured using an optical microscope and a clamp meter providing the values  $\Lambda = 8.1 \pm 0.1 \mu\text{m}$  (pitch) and  $d = 3.6 \pm 0.1 \mu\text{m}$  (hole diameter), which are used throughout this chapter in the context of fiber modelling. More details on the fiber modelling are given in the next chapter.

### 6.1 Dispersion measurement

For simulating supercontinuum one important effect to describe accurately is dispersion and the associated position of the zero-dispersion wavelength (ZDW). Simulations rely on fiber parameters, such as the dispersion, computed with COMSOL, because it would simply be infeasible to experimentally measure the dispersion for each of the many different fiber geometries that occur throughout the down and up taper areas in the very broad frequency window spanning over  $10 \mu\text{m}$ . Hence, it is important to verify that the modelling of the fibers is accurate, so that we can trust the implementation of the linear operator.

#### 6.1.1 Experimental method and setup

The method employed is a spectral interferometry-based technique as outlined in [25], but here we apply it to a sequence of different configurations in order to increase the bandwidth of the spectrum that we can accurately characterise.

The setup is essentially similar to that of a Mach-Zehnder interferometer, but with one arm being of adjustable length,  $L$ , and the fiber to be characterised being part of the other arm – see figure 6.1. The SC source has a bandwidth spanning up to about  $5 \mu\text{m}$ .

The fiber is assumed to be an endlessly single-mode fiber, such that the measured dispersion can be ascribed to the fundamental mode. However, there might be two polarisation modes propagating simultaneously, which could be remedied by using a polariser in the setup situated before the first beam splitter, but as numerical modelling reveals the polarisation modes of the

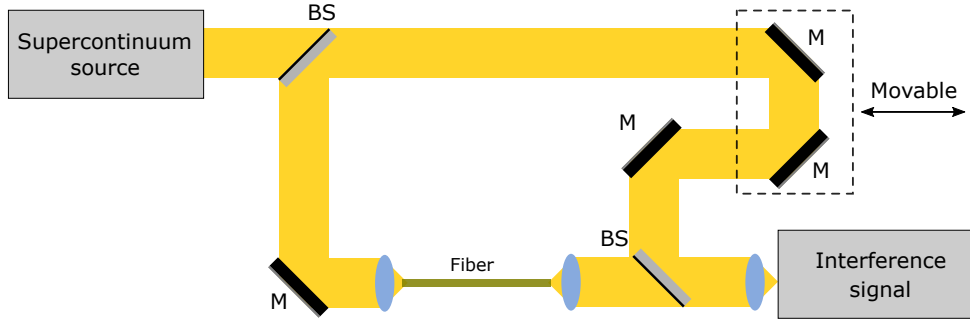


**Figure 6.1:** Experimental setup to determine chromatic dispersion.

fundamental mode are virtually identical with respect to dispersion, and thus we have chosen to not distinguish between the two and rather treat them as one in the experiment.

At the detector the optical path difference (OPD) will be given by

$$\Delta p(\lambda) = p_{\text{ref}} - p_{\text{test}}(\lambda) = L - l - n_{\text{eff}}(\lambda)z, \quad (6.1)$$

where  $l$  is the path length in the air in the test arm,  $n_{\text{eff}}$  and  $z$  is respectively the effective refractive index of the propagating mode and the length of the fiber.

The interference maxima (fringes with constructive interference) are given by

$$L - l - n_{\text{eff}}(\lambda)z = m\lambda, \quad (6.2)$$

where  $m$  is the interference order of the fringes. The effective refractive index is now approximated by a modified Cauchy dispersion formula [25]

$$n_{\text{eff}}(\lambda) = A_1\lambda^{-4} + A_2\lambda^{-2} + A_3 + A_4\lambda^2 + A_5\lambda^4, \quad (6.3)$$

where  $A_i$  are constants to be determined. Inserting (6.3) into (6.2), we find

$$a_1\lambda^{-5} + a_2\lambda^{-3} + a_3\lambda^{-1} + a_4\lambda + a_5\lambda^3 = m, \quad (6.4)$$

where  $a_1 = -A_1z$ ,  $a_2 = -A_2z$ ,  $a_3 = L - l - A_3z$ ,  $a_4 = -A_4z$  and  $a_5 = -A_5z$ . If we measure the wavelengths to which the interference orders  $m$  correspond, as well as measuring the fibre length  $z$ , a fitting scheme can now be applied to (6.4) to obtain the coefficients.

When the coefficients are determined, we are able to describe  $n_{\text{eff}}$  by means of eq. (6.3). By definition the dispersion can then be evaluated as  $D = \partial_\lambda \beta_1 = -(2\pi c/\lambda^2)\beta_2$ , where  $\beta_1 = 1/v_g$  is the inverse group velocity that can be written

$$\begin{aligned} \beta_1 = \partial_\omega \beta &= \frac{1}{c} \partial_\omega [n_{\text{eff}}(\omega)\omega] = \frac{1}{c} [n_{\text{eff}}(\omega) + \partial_\omega n_{\text{eff}}(\omega)] \\ &= \frac{1}{c} [n_{\text{eff}}(\lambda) - \partial_\lambda n_{\text{eff}}(\lambda)], \end{aligned} \quad (6.5)$$

where the definition of the effective refractive index has been used  $\beta = n_{\text{eff}}(2\pi/\lambda) = n_{\text{eff}}\omega/c$  as well as the chain rule. Inserting (6.3) into (6.5) to obtain  $\beta_1$ , the formula for the dispersion becomes

$$D = \partial_\lambda \beta_1 = \frac{1}{c} [-20A_1\lambda^{-5} - 6A_2\lambda^{-3} - 2A_4\lambda - 12A_5\lambda^3]. \quad (6.6)$$

The zero dispersion wavelength (ZDW) is then found by finding the root of the dispersion,  $D(\lambda) = 0$ .

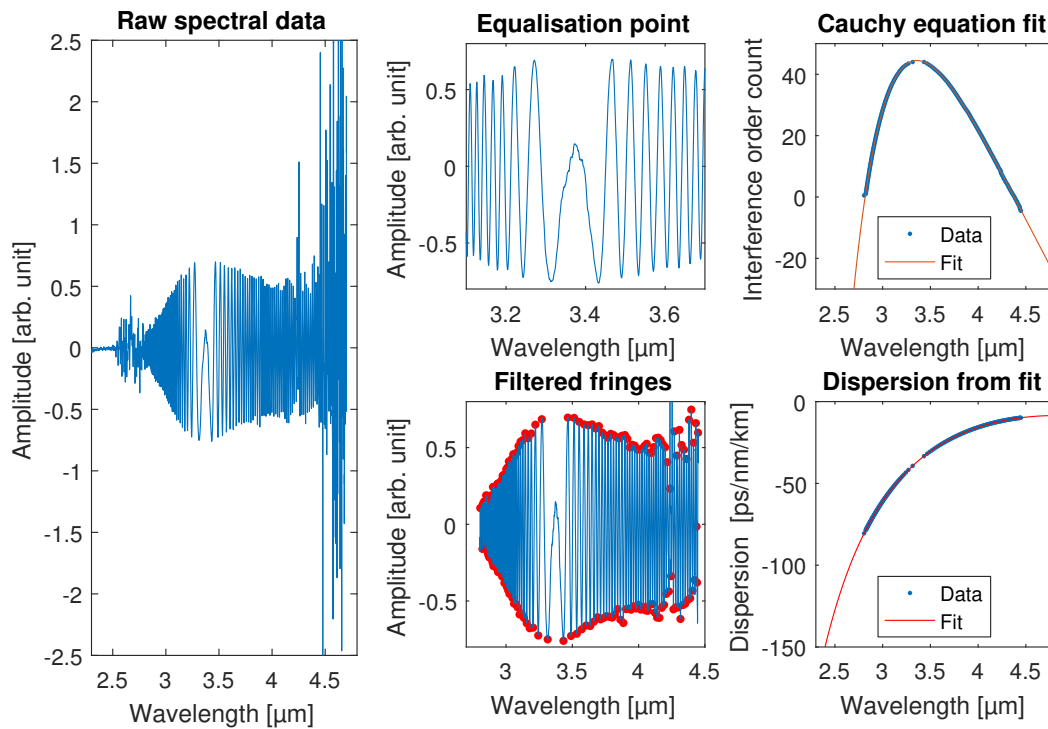


**Figure 6.2:** The unprocessed output from the spectrometer is shown to the left. The central part of the spectrum is enlarged in the top-mid plot, which shows the point at which the optical paths in the two arms are exactly equal. In the bottom-mid plot, the interference maxima with their associated wavelengths have been identified, which is shown on the top-right plot together with the resulting fit. The fit coefficients can then be used to express the dispersion shown to in the bottom-right.

## 6.1.2 Results

The fiber length was measured to be 18.5 cm. The spectrum obtained directly from the spectrometer is shown to the left of figure 6.2. The space near 3.5  $\mu\text{m}$  shows the equalisation point, where the optical paths are exactly equal. There is very noticeable noise in both ends of the spectrum, and therefore we truncate the spectrum at about 2.8  $\mu\text{m}$  and 4.5  $\mu\text{m}$ . The truncated spectrum with the identified interference maxima at their respective wavelength, which can then be used for fitting, can be seen in the bottom-mid of the figure.

By performing a nonlinear least squares fit of the Cauchy equation, shown in the top-right, we can then evaluate the dispersion from the coefficients, shown in the bottom-right. Clearly, the dispersion does not reach zero within the interval covered by the data sample points, and thus the ZDW has to be determined via extrapolation. For the extrapolation to be accurate, the dispersion within the range that we can actually measure must have very little uncertainty, since the extrapolation will naturally enhance any uncertainty already inherent in the fit. For this reason, and with the prospect of covering an even larger bandwidth, we repeat the measurement with different lengths of the reference arm, which will shift the equalisation point.

The measurement was performed at more than 10 different reference arm lengths, and the spectra obtained are shown in figure 6.3(a) with the resulting dispersion fits in 6.3(b).

We can now average over all the fits to increase the accuracy. The interval from about 3.2  $\mu\text{m}$  to 4.2  $\mu\text{m}$  is covered by all the measurements, referred to as 100 % coverage, and will thus have the highest expected accuracy.

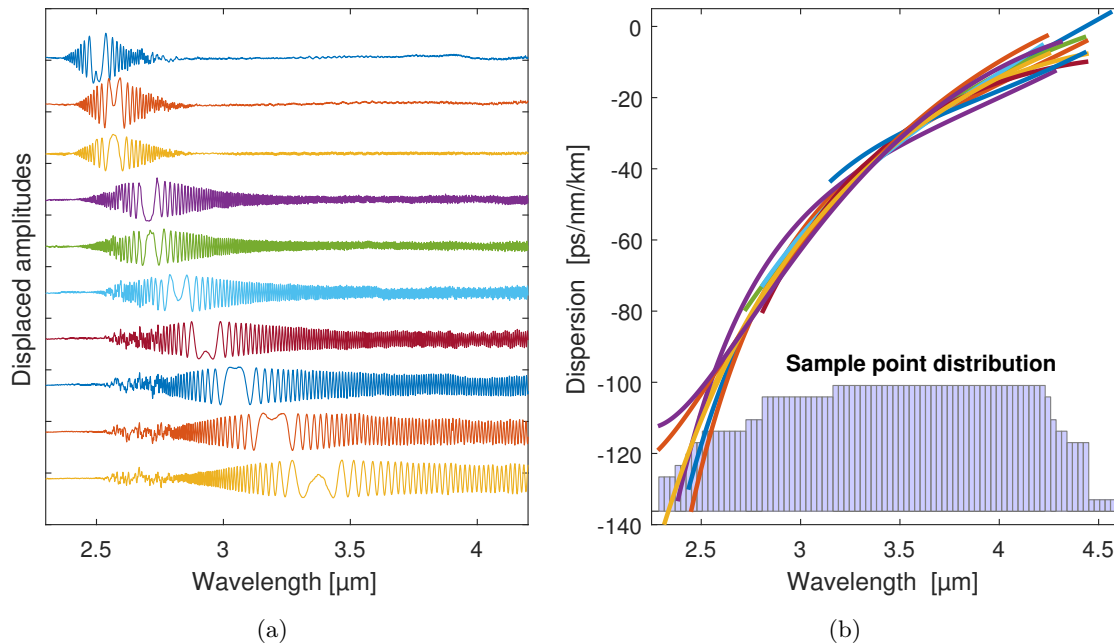


**Figure 6.3:** Data was obtained with several different lengths for the reference arm resulting in the equalisation point for the OPD to occur at different wavelengths (a). This results in multiple fits of the dispersion (b), which can then be combined for additional accuracy. The sample point distribution shown in (b) indicate how many of the measurements have spectra whose range overlap at a given frequency – for instance only a single measurement extended beyond 4.5 μm as can be seen.

We can now proceed to compare the averaged fits with numerical results from COMSOL. As noted in the beginning of the chapter the pitch and hole diameter were measured to be  $\Lambda = 8.1 \pm 0.1 \mu\text{m}$  and  $d = 3.6 \pm 0.1 \mu\text{m}$ , where the uncertainty stems from the limited resolution of the optical microscope and the uncertainty of the outer diameter when measured with clamp meter. This measurement will be elaborated shortly, but for now we will assume the uncertainty of  $\pm 0.1 \mu\text{m}$  of both parameters, and therefore perform four computations of the fiber (i.e. the four combinations of  $\Lambda = \{8.0, 8.2\} \mu\text{m}$  and  $d = \{3.5, 3.7\} \mu\text{m}$ ) to compare with the experimental results. On figure 6.4 those four computations of the dispersion and the corresponding ZDWs are shown together with averaged fit of the experimental data and the extrapolated ZDW.

Overall the agreement is decent, especially in area with 100 % sample coverage, where the fit is verified to be completely within the bounds of uncertainty for all wavelengths. However, there is a 2 % error in the ZDW, presumably due to the use of extrapolation. Most likely a better agreement would be found if a SC source with a larger bandwidth is used such that the sample coverage would extend to at least beyond the ZDW.

So far we have only considered uncertainty in the fiber dimensions, but since the length of the fiber is also used in evaluating the dispersion, the uncertainty in this parameter will also have an impact on the end result. The fiber length can be measured to within millimeter precision, and on figure 6.5 we see the different end results based on one of the measurements when assuming an uncertainty of  $\pm 1 \text{ mm}$ . Evidently, the final fit is not very sensitive to small changes in the fiber length, certainly not near the ZDW, and hence the uncertainty of  $\pm 1 \text{ mm}$  in  $z$  is not crucial.

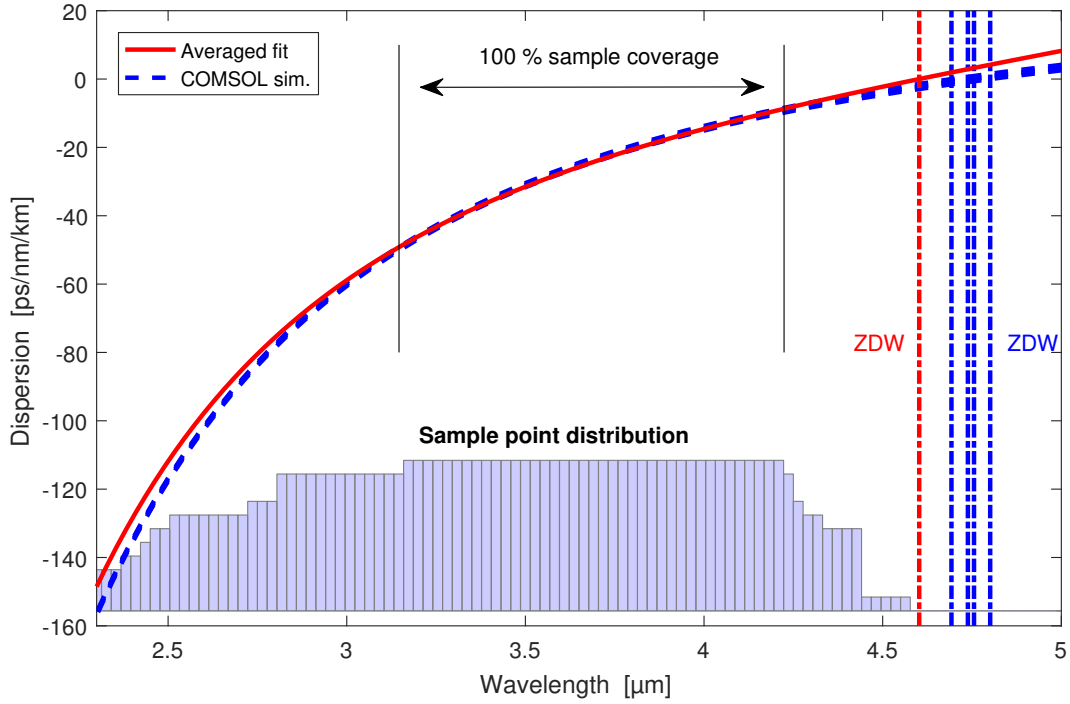


**Figure 6.4:** Dispersion obtained from averaged fits compared to simulation results from COMSOL. As no samples points correspond to  $D = 0$ , the ZDW was extrapolated to be  $4.60 \mu\text{m}$ , whereas the ZDWs obtained from modelling are  $4.69$ ,  $4.74$ ,  $4.76$  and  $4.80 \mu\text{m}$ . This corresponds to an error at around  $2\%$ , which seems reasonable given the uncertainty inherent in extrapolation. Meanwhile, the error in the interval with  $100\%$  sample coverage is completely within the bounds of uncertainty.

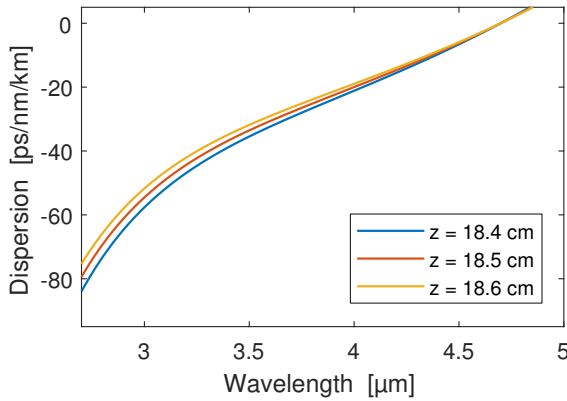


**Figure 6.5:** Sensitivity on fiber length for the resulting dispersion fit. The measured fiber length was  $z = 18.5 \pm 0.1 \text{ cm}$ , and since  $z$  is an input parameter to the dispersion formula, we consider here how the uncertainty propagates into the resulting fit. The deviation between the two extremes is significant for wavelengths below  $3.5$ , but very small in the area near the ZDW.

## 6.2 Estimation of nonlinear refractive index

The higher value of the nonlinear refractive index,  $n_2$ , is what makes chalcogenide among other soft glasses much more nonlinear than silica. For chalcogenide  $n_2$  can be 100-400 times larger than it is for silica. It is an important input parameter when simulating SC generation since the product between the power and  $n_2$  essentially determines the degree of nonlinearity. As we have seen previously, the first nonlinear effect that develops when pumping with a monochromatic source is SPM, which we want to now measure in order to estimate the value of  $n_2$ . Since the nonlinear refractive index is treated as a constant, even though it does in fact vary slightly with

wavelength, what we will do in this experiment is to vary the power and consider the resulting SPM, which then is matched to a numerical result by using  $n_2$  as a free parameter in a nonlinear optimisation algorithm. The optimisation algorithm used to find the optima is `fminsearch` in MATLAB.

The manufacturer of the fiber, Selenoptics, has noted on a data sheet of the fiber that they have measured the nonlinear refractive index to be  $8.8 \cdot 10^{-18} \text{ m}^2/\text{W}$  at  $1.55 \text{ }\mu\text{m}$  wavelength. We will estimate the value at  $1.93 \text{ }\mu\text{m}$ , which is expected to be significantly lower if studies of other chalcogenide compositions are any indication [26].

### 6.2.1 Experimental setup

A typical way of measuring the value of  $n_2$  is to use the z-scan technique [7], in which a sample of the material to be characterised is moved through different positions (hence the name) after the focal point of a laser beam. At each position the beam radius is then measured by a detector, and due to the self-focusing effect associated with the Kerr effect, the correlation between position and measured beam radius can be used to calculate  $n_2$ .

Due to the topic of this thesis, and availability of experimental equipment, the setup that have been used in this experiment revolves around propagation in a fiber and is overall simpler and presumably more inaccurate than the z-scan technique. In the setup a monochromatic mode-locked pump laser is propagated through a fiber consisting of the material we wish to measure  $n_2$  for, after which the spectrum is recorded with a spectrometer. The transmission through the fiber must be measured as well to be able to estimate the pulse peak power after coupling into the beginning of the fiber. The setup is shown on 6.6.

The pump laser has a 31 MHz repetition rate of  $\text{sech}^2$ -shaped pulses with a FWHM of 1.9 ps at a wavelength of  $1.93 \text{ }\mu\text{m}$ . The integration time of the spectrometer is 20 ms, and the spectral resolution of spectrograms is 5 nm.

The method employed here is expected to be less accurate than the z-scan technique, because the latter involves only a small sample of the material, whereas the method here will be affected by the losses and propagation effects of an optical fiber.

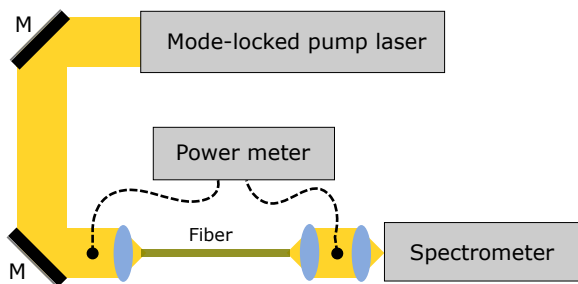


**Figure 6.6:** Experimental setup for a simple method to quantify the nonlinear refractive index. The power meter is sometimes connected to determine transmission at different power levels.

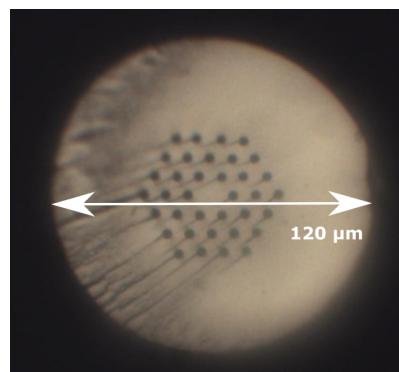


**Figure 6.7:** Microscope image of PCF fiber. Outer diameter was measured with a clamp meter to be  $120 \pm 2 \text{ }\mu\text{m}$ , which can then be used as a scale to obtain the noted pitch and hole diameter.

## 6.2.2 Analysis and results

Firstly, the fiber dimensions are measured to make modelling of the the propagation in the fiber possible. A clamp meter is used to measure the outer diameter of the fiber, which was found to be  $120 \pm 2 \mu\text{m}$ . The cross section of the fiber is then imaged with an optical microscope. The image is shown in figure 6.7. Given the measurement of the outer diameter, the pitch and hole diameter can be determined to be  $\Lambda = 8.1 \pm 0.1 \mu\text{m}$  and  $d = 3.6 \pm 0.1 \mu\text{m}$ .

The transmission was measured to be 9-15 % depending on the power – the transmission was lowest for higher pump power. After measuring the transmission the fiber is aligned to couple into the spectrometer, where the spectra can then be recorded.

The input peak power in the fiber is then estimated from the known pump power of the source, the transmission and then accounting for Fresnel coupling loss and propagation loss. The Fresnel coupling loss in the fiber end is 20 % [22], and the propagation loss is estimated to be 5 dB/m at 1.93  $\mu\text{m}$  wavelength based on loss data provided by the manufacturer – this data will be shown in the next chapter. The fiber was measured to be 14.6 cm long, which gives an expected loss of 0.8 dB during propagation. We will consider three different measurements with average pump powers 95 mW, 550 mW and 790 mW. The associated peak powers were then estimated to be 289 W, 1122 W and 1451 W based on the parameters above.

The laser source that was used is known to have some chirp [27], but the exact amount has not been measured. Therefore, chirp was introduced in the modelling as a free parameter that is also optimised upon. The chirp is added to the simulated input pulse in the following way [7]

$$A = \sqrt{P} \text{sech}(t/T_0) e^{i(C/2)t^2/T_0^2}, \quad (6.7)$$

where  $C$  is the free chirp parameter. The optima that were found tended to have values close to  $C = 5$ . An optimisation without chirp has also been done and it will be referred to shortly.

Before considering the measurements and simulation results, the process of fitting will first be described. As mentioned the optimisation algorithm employed varies the  $n_2$  parameter until an optimal agreement is found between the measured and simulated result. An optimal agreement is a minimum of an error function that we define to describe the difference between the results. A straight-forward way to define the error function is via the  $l^1$  norm given by

$$\begin{aligned} E(P_{\text{exp}}, P_{\text{sim}}) &= \|P_{\text{exp}}(\lambda) - P_{\text{sim}}(\lambda)\|_1 \\ &= \sum_i |P_{\text{exp}}(\lambda_i) - P_{\text{sim}}(\lambda_i)|, \end{aligned} \quad (6.8)$$

where  $P_{\text{exp|sim}}$  is the power spectral density (PSD) of the experimental result and simulation result, respectively, and  $\lambda_i$  is a wavelength in a discretized grid that has been chosen appropriately. The problem with this error function is that the optimisation will revolve around matching peaks rather than the wings – SPM is characterised by a spectral broadening, so the optimisation should be more concerned about matching the general shape of the results. To reflect this we define an alternative error function as

$$\begin{aligned} E_{\ln}(P_{\text{exp}}, P_{\text{sim}}) &= \|\ln[P_{\text{exp}}(\lambda)] - \ln[P_{\text{sim}}(\lambda)]\|_1 \\ &= \sum_i |\ln[P_{\text{exp}}(\lambda_i)] - \ln[P_{\text{sim}}(\lambda_i)]|. \end{aligned} \quad (6.9)$$

We will use both error functions in the following to see how it affects the fitted value of  $n_2$ , and possibly average over those values if they turn out differently.

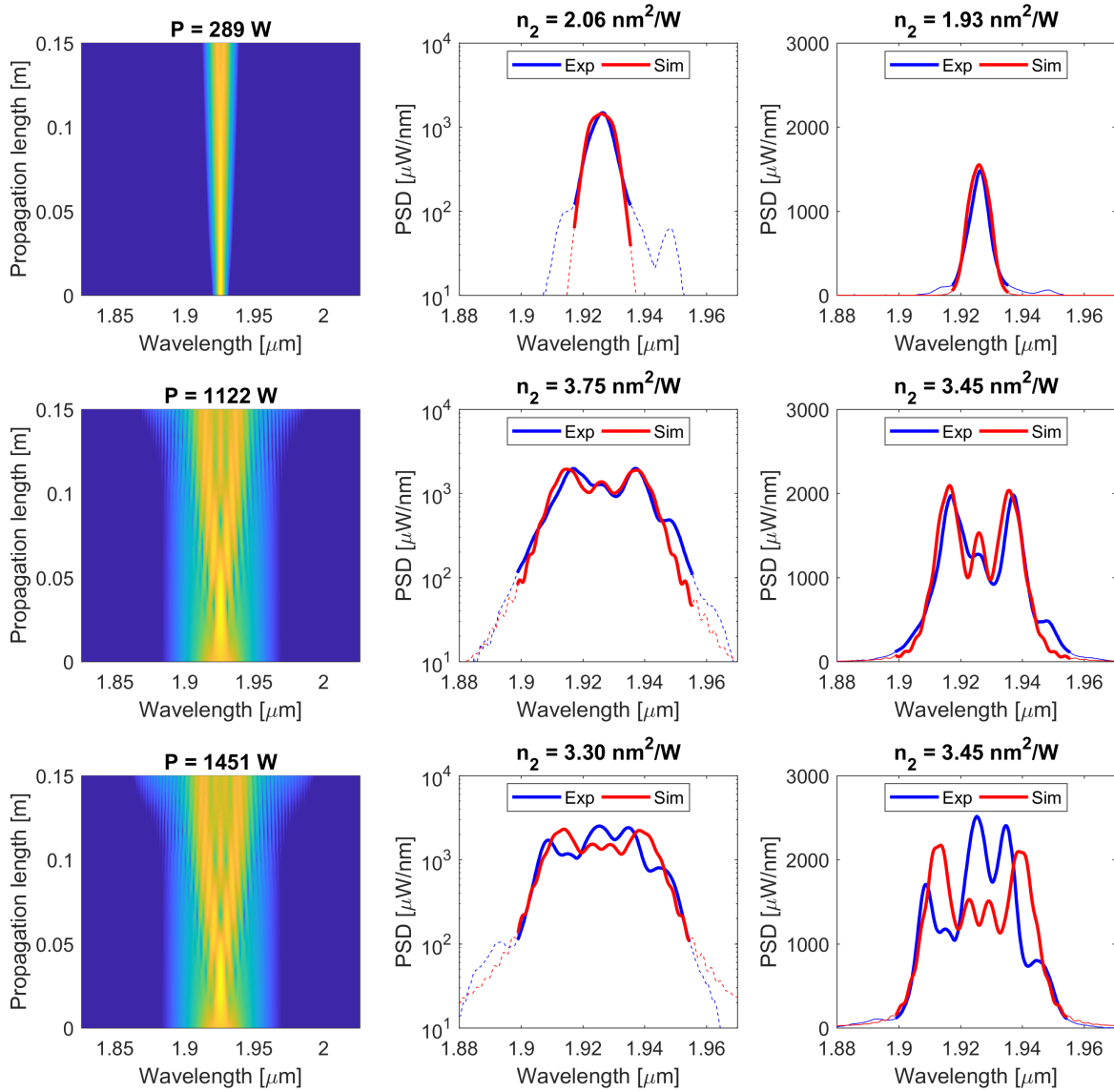


**Figure 6.8:** Measurements and corresponding fits at three different levels of estimated peak power. Each row of figures correspond to a certain power. First column of figures show the PSD during propagation in the simulated fiber. Column two and three shown optimal fits to measured spectra based on errors computed as logarithmic and linear deviation, respectively, resulting in two different but relatively close values for  $n_2$  in each case.

One more non-trivial matter regarding the optimisation is about convergence. While there are several measurements that ideally should be simultaneously fitted, the optimisation does not converge well when minimising a sum of multiple error functions each describing different pairs of measurement/simulation results. In other words if the objective function is too complex, the algorithm converges very slowly, and when it does the solution is likely to be one out of many local optima that do not fit any one of the pairs very well. Hence, the optimisation is applied to each measurement separately, and therefore multiple values of  $n_2$  will be found; one describing each measurement optimally. The final estimate on  $n_2$  is then taken to be the average of these individual results.

The measurements and simulation results are shown on figure 6.8, where each row of plots correspond to a different power. The dashed lines in the two rightmost plots of each row is data that has been filtered out when evaluating the error functions. There is very little SPM visible for the uppermost case, where the average pump power is 289 W. The optimal  $n_2$  for both error functions in this case are close to  $2 \cdot 10^{-18} \text{ m}^2/\text{W} = 2 \text{ nm}^2/\text{W}$ , but given the very low power for this case, the  $n_2$  value could easily be 50 % larger without much more spectral broadening being present – equivalently if the fitted value of  $n_2$  is kept at what it is found to be, and we increase the peak power from 289 W to 400 W in the simulation, the end result does not differ significantly. Therefore, the fitted value at low powers are bound to be rather uncertain and should be considered with a bit of scepticism if not simply rejected. The two measurements at higher power do show much more spectral broadening, and while a somewhat peculiar spectrum is found in the measurement corresponding to the 1451 W peak power case, there seems to be a consistent pattern in the fitted values of  $n_2$  with all being within 8 % of  $3.5 \text{ nm}^2/\text{W}$ . The two different definitions of the error functions also produce quite similar results. If we do not include chirp, the error functions do not reach as low minima, and the fitted values are on average close to  $2.5 \text{ nm}^2/\text{W}$  with one value being above  $3 \text{ nm}^2/\text{W}$  – the unchirped optima can be seen in app. B.

The peculiar central peaks in case of the measurement in the bottom of 6.8 is a cause of concern regarding the quality of the laser. The laser could have significant relative intensity noise (RIN), which could potentially produce pulses showing different levels of SPM and thus different levels of broadening within the integration time of the spectrometer. Those pulses that are broadened would be closer to the center wavelength, and so the fact that such central peaks are observed even for high average power could be due to this noise source. However, if that was the case, it seems unlikely that the central peaks would also be dominant in amplitude. Other proposals could be that the pump wavelength or the mode-locking of the laser is unstable.

Rejecting the fitted values for the uppermost case in the figure, the average of the four remaining fitted values give us the final result  $n_2 = 3.5 \text{ nm}^2/\text{W}$  with a potential uncertainty of as much as  $1 \text{ nm}^2/\text{W}$  if we are conservative and entertain the thought that the rejected and/or unchirped fitted values were actually accurate.

The final result does differ quite a lot from the manufacturer’s measured value at  $1.55 \mu\text{m}$ . The question is if this discrepancy can be explained by the almost 400 nm difference between their measurement at  $1.55 \mu\text{m}$  and our measurement at  $1.93 \mu\text{m}$ . Consulting the literature shows that quite significant drops can indeed happen for chalcogenide when increasing the wavelength, although perhaps not enough to explain the discrepancy above. In [26] for instance, there are comparisons of  $n_2$  measured at different wavelengths in other chalcogenide fibers, where the more reliable z-scan technique has been used. The chalcogenide composition  $\text{As}_{40}\text{Se}_{60}$  was found to decrease from 18 to  $10 \text{ nm}^2/\text{W}$  (55 % decrease) when the wavelength is increased from 1064 nm to 1430 nm. A similar result was found for the composition  $\text{Ge}_{20}\text{As}_{40}\text{Se}_{40}$ , which decreases from 18.5 to  $8.5 \text{ nm}^2/\text{W}$  (54 % decrease) with the same increase in wavelength. The latter composition is presumably quite similar to the composition that have been measured upon in this experiment, namely  $\text{Ge}_{10}\text{As}_{22}\text{Se}_{68}$ , but whether a comparable decrease of as much as 50 % is expected when increasing the wavelength another 400 nm is unknown.

# CHAPTER 7

## Supercontinuum generation in tapered chalcogenide fibers

In this chapter we will study a tapered photonic crystal fiber (PCF) of the composition  $\text{Ge}_{10}\text{As}_{22}\text{Se}_{68}$ . The length of the sections of taper are shown in figure 7.1, while other dimension parameters are presented in table 7.1. The values used are based on measurements performed on the same taper in an experiment introduced shortly.

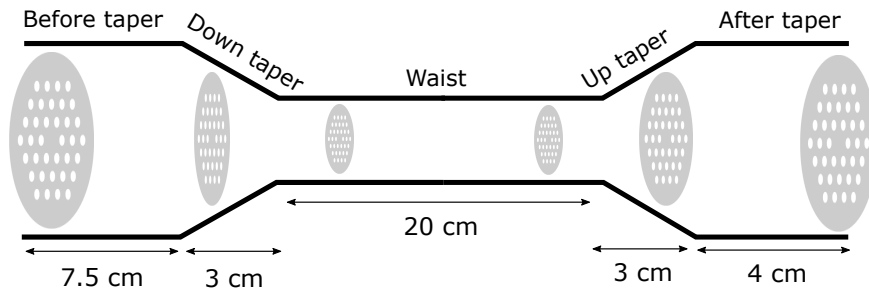


**Figure 7.1:** Lengths of the parts of the tapered fiber that is simulated.

**Table 7.1:** Tapered fiber dimensions. The value for  $d_{\text{core}}$  and OD are only included for reference – these parameters do not have a direct presence in the modelling.

	$d_{\text{core}}$ [ $\mu\text{m}$ ]	OD [ $\mu\text{m}$ ]	$d$ [ $\mu\text{m}$ ]	$\Lambda$ [ $\mu\text{m}$ ]	$d/\Lambda$
<b>Before/after taper</b>	15.1	176	5.10	10.08	0.51
<b>Taper waist</b>	5.9	67	1.89	3.91	0.48

All results presented in this chapter are ensemble averages over 10 simulations based on the parameters stated above. The code of the solver that has been developed and used in the project is presented in appendix C.

### 7.1 Discretizing a tapered fiber

In a segment of a fiber where tapering occurs, the continuous reduction of fiber dimensions will cause the linear operator to have a  $z$ -dependence. The linear operator is computed in COMSOL given specific fiber dimensions, but as this is a rather demanding computation, we cannot hope to make a new computation of the fiber modes for every single step in the simulation of pulse propagation, nor would it be very beneficial as the changes of fiber dimensions in a single step are minute. The down and up taper sections tends to be 3 cm, and a propagation step in simulations in this work is on the order of  $10^{-5}$ , corresponding to 3000 points in each of the tapering sections with unique fiber modes.

Hence, we have to partition the tapering sections into a more coarse grid of discretized points allowing interpolation of only relatively few computed fiber modes. For a point  $z$  that is between the two points  $s_0$  and  $s_1$  (referred to as nodes henceforth) for which the corresponding fiber mode solutions have been computed, we choose to apply a linear interpolation given by

$$f(z) = (1 - r)f(s_0) + rf(s_1), \quad r = \frac{z - s_0}{s_1 - s_0} \quad (7.1)$$

where  $f$  is the quantity that is desired. In the case of solving the MM-GNLSE introduced earlier the quantities to interpolate are the linear operator (propagation constant and confinement attenuation), the overlap integrals and the shock time constants (provided the approximation  $\tau \approx 1/\omega_0$  is not applied).

The taper is partitioned into equally spaced nodes, but the question is now how many nodes are needed to make the overall interpolation sufficiently accurate. The way we address this is by considering the maximal interpolation error between two nodes in the taper, which is assumed to be in the centre between the nodes. Examples of a taper discretized into either three and five nodes is shown in figure 7.2(a), where the nodes have been used to interpolate the effective

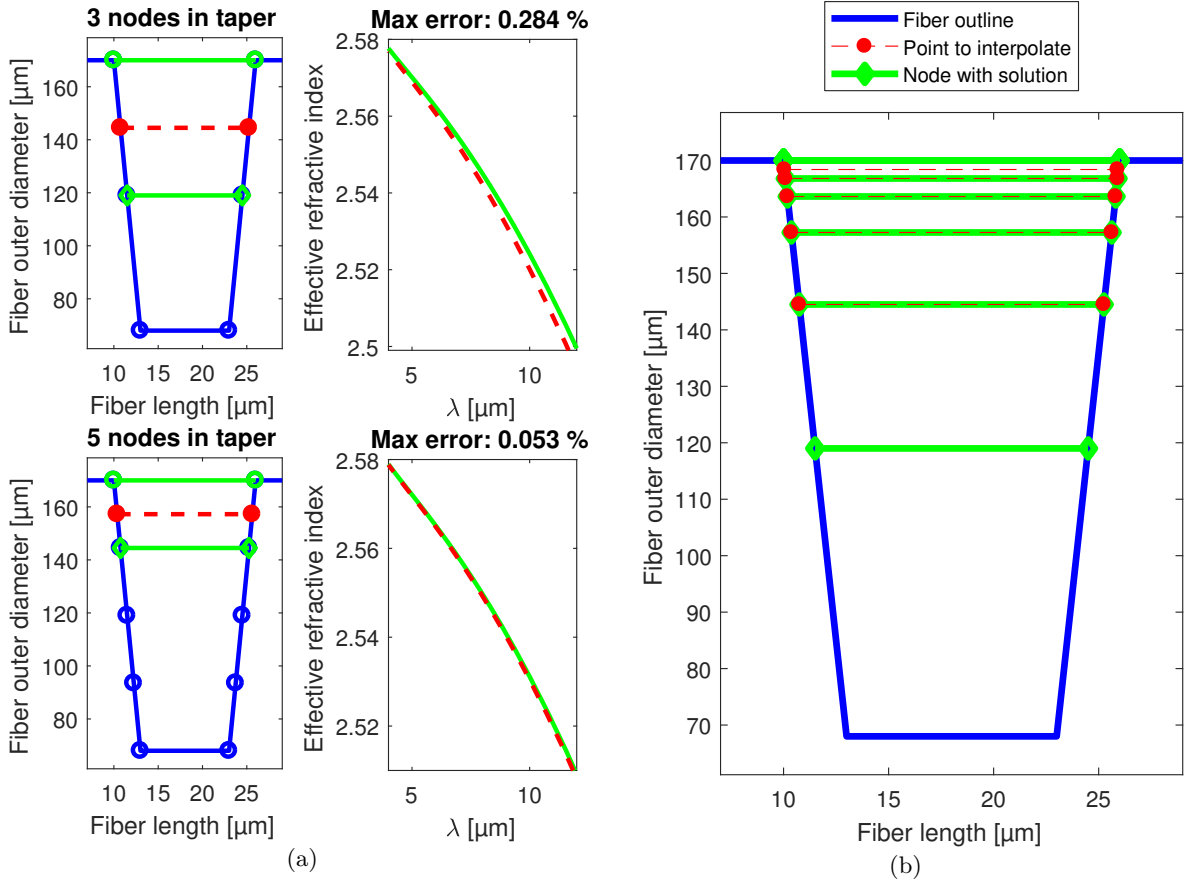


**Figure 7.2:** The two row of plots to the left show examples of discretizing the taper into either 2 and 4 intervals and the effective refractive indices at the position indicated by the red dashed lines, when using solutions at the positions indicated by the green lines. To the right is shown a figure of how a convergence test has been made, in which five different interpolants are computed corresponding to discretizing the taper into 4, 8, 16, 32 and 64 intervals.

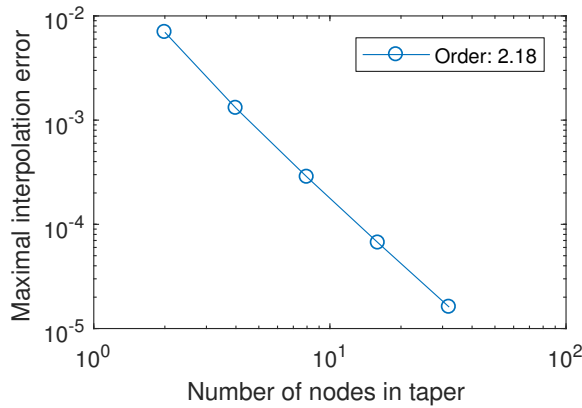


**Figure 7.3:** Convergence of the interpolation error when increasing the number of nodes in the taper segments. The interpolation error is taken to be the maximal absolute error between the interpolated refractive index and a reference numerical solution.

refractive index shown to the right of the figure. The addition of two nodes reduces the distance between nodes by a factor of 2, and is seen to reduce the maximal error of the interpolation by a factor of 4. This is an indication of quadratic convergence rate. The error is found as  $\|n_{\text{eff,interp}} - n_{\text{eff,ref}}\|$ , where  $n_{\text{eff,ref}}$  is a reference computation done at the same point (shown as the green curves in the subplots to the right of figure 7.2(a)).

Generalising upon this we want to estimate the error when we instead have for instance 9, 17 and 33 nodes in the taper. Let a node referred to as  $i/N$  be a node that is in the beginning of the  $i$ th interval, when the taper is partitioned into  $N$  equally sized intervals. The taper from before with 3 nodes will then have node indices  $0/2$ ,  $1/2$  and  $2/2$ . To estimate the generalised interpolation error, we then calculate the error at the  $1/64$  node when interpolating between the  $0/64$  and  $2/64$  nodes, and similarly at the  $1/32$ ,  $1/16$ ,  $1/8$  and  $1/4$  nodes when interpolating between the  $0/32$  and  $2/32$ , and so on. Notice that several nodes then coincide, e.g. the  $1/64$  and  $2/32$  nodes are at the same position in the taper. The positions that we interpolate and the nodes used to interpolate are visualised in figure 7.2(b). The errors are determined as before with reference computations at the same positions as the interpolants. The resulting errors are shown on figure 7.3. The convergence rate, indicated in the figure legend, is found to be quadratic as expected. Based on this information a minimum of 9 nodes should be employed to ensure an accuracy in line with the tolerance used in simulations.

## 7.2 Optical properties along taper

To describe the refractive index of the material of the fiber modelled in COMSOL, the Sellmeier equation is used

$$n_{\text{mat}}^2(\lambda) = 1 + \sum_{i=1}^3 \frac{B_i}{1 - C_i/\lambda}, \quad \begin{cases} B_1 = 2.774, B_2 = 2.892, B_3 = 0.7320, \\ C_1 = 0, C_2 = 0.4047/10^6, C_3 = 38.53/10^6 \end{cases} \quad (7.2)$$

where the coefficients have been experimentally determined by the fiber manufacturer. With the values in table 7.1, we now partition the down taper into 9 nodes, leading to 9 pairs of pitch and hole diameters with different computed optical properties associated with each pair, shown on figure 7.4 for the fundamental mode in the fiber. All values are found to be practically identical between the two polarisations modes, hence the values can be assumed to apply to both modes even if the ones shown here are based on the first polarisation mode. The values of the pitch and hole diameters of each pair is shown in the figure legend where units of  $\mu\text{m}$  is implied.

From the dispersion plot, we see that the ZDW is about 5  $\mu\text{m}$  before the taper, while getting close to 3  $\mu\text{m}$  in the waist. A second ZDW around 9  $\mu\text{m}$  also appears in the waist. As the fiber core becomes smaller near the waist, it makes sense that the effective mode area is seen to become smaller as well, resulting in higher nonlinearities in the down taper and waist due to the inverse proportionality between  $A_{\text{eff}}$  and  $\gamma$ . However, the increased nonlinearities comes at the price of higher attenuation as seen by the loss edges being shifted to shorter wavelengths close to the waist. This is only slightly counteracted by the fact that the fraction of the mode residing in the glass, and not the air holes of the PCF, becomes lower, referred to as glass occupancy (denoted  $r_{\text{glass}}$ ), leading to a lower material loss, which has to be measured and will be considered shortly. The net loss, or attenuation, is given by

$$\alpha = \alpha_{\text{con}} + r_{\text{glass}}\alpha_{\text{mat}}, \quad (7.3)$$

where  $\alpha_{\text{mat}}$  is the material loss and  $\alpha_{\text{con}}$  is the confinement loss, which is the attenuation shown in figure 7.4. The confinement loss at long wavelengths near and inside the waist is much greater than the material loss, hence even when including  $r_{\text{glass}}$  factor the net loss is still much larger here than before and after the tapering.

The effective refractive indices are seen to only approximately coincide with the material refractive index given by (7.2), and indicated by the black dashed line, at short wavelengths, and for longer wavelengths they are overall significantly lower with the minimum being in the waist.

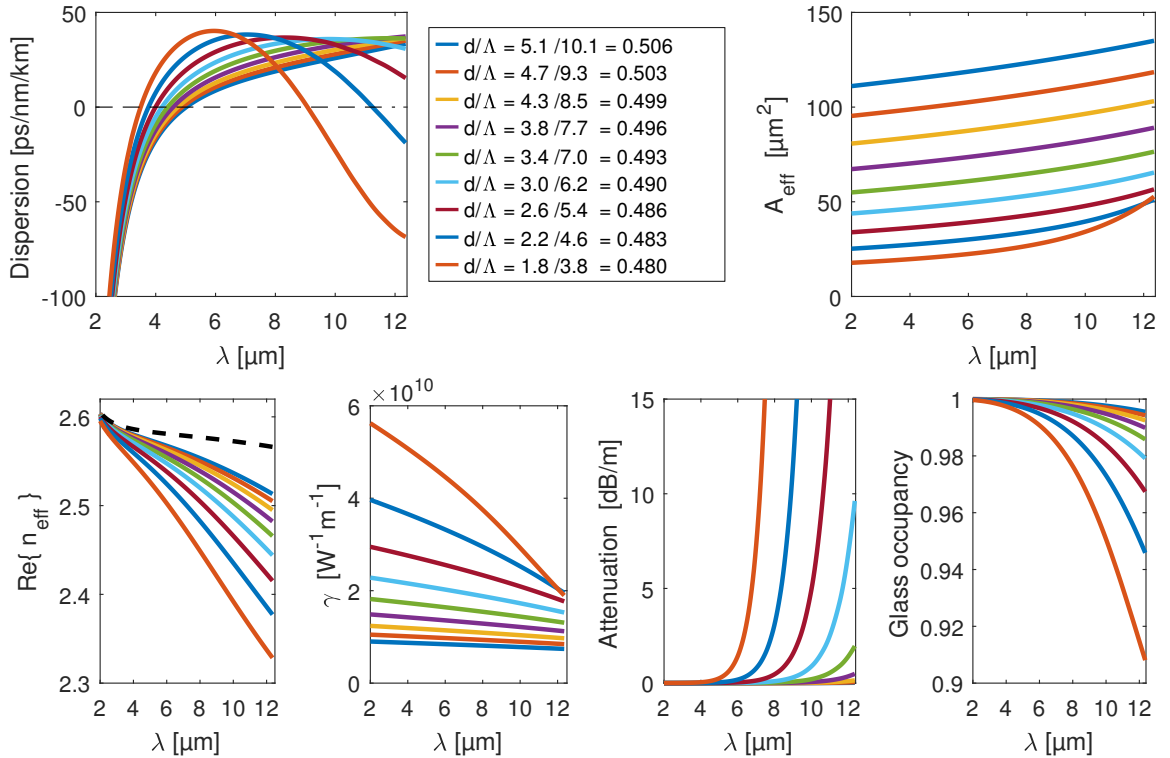


**Figure 7.4:** Dispersion, effective mode area, effective refractive index (for which the black dashed line corresponds to the Sellmeier equation for the material), nonlinear coefficient, attenuation or confinement loss, and a so-called glass occupancy defined to be the fraction of the mode that is within the glass and not the air holes of the PCF.

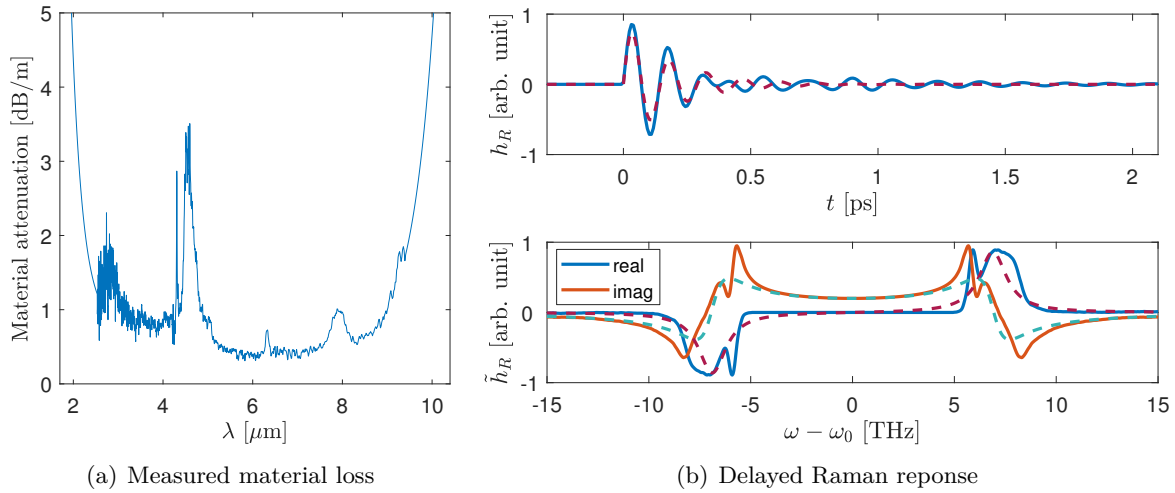


**Figure 7.5:** (a) Material loss of the considered chalcogenide fiber, measured in [28]. (b) Delayed Raman response function, measured in [22], shown in time domain (top) and frequency domain (bottom) shown with a reference analytical approximation, indicated by the dashed lines, given in [12]

As mentioned the material loss has to be measured, which has been done in [28], and the measurement is shown in figure 7.5(a). Absorption by impurities appear clearly at wavelengths of 2.9  $\mu\text{m}$ , 4.6  $\mu\text{m}$ , 6.3  $\mu\text{m}$  and 7.8  $\mu\text{m}$ , associated with O-H, Se-H, H-O-H and Ge-O absorption [22], respectively. The loss was only reliably measured at wavelengths from around 2.4  $\mu\text{m}$  to 9.7  $\mu\text{m}$ , and since the spectral window used in the simulations surpasses this bandwidth, the boundaries of the loss has been artificially extended, which can be seen as the sharp loss edges at 2  $\mu\text{m}$  and 10  $\mu\text{m}$ .

On figure 7.5(b) the measured delayed Raman response is shown [22], both in time and frequency domain, where an analytical approximation for a similar chalcogenide composition, determined in [12], has been included as reference. The analytical approximation is of the form given by 4.5 but with  $\tau_1 = 23.1$  fs and  $\tau_2 = 195$  fs. The analytical approximation is seen to follow the measured Raman response relatively well with the main difference being that the peaks in the frequency domain are Lorentzian shaped and do not feature a small dip as seen in the measured data. The analytical approximation has only been tested in simulations, and the results are nearly identical, so the differently shaped peaks are not of great significance. The value of the fractional Raman contribution that we will tend to use is  $f_R = 0.15$ , lower than the value of  $f_R = 0.18$  often used for silica, but we will also consider a value as low as  $f_R = 0.09$ , which is found to produce similar results. In [12] the value  $f_R = 0.115$  is found for a certain chalcogenide fiber, which was used as a starting point in our simulations and then freely adjusted to  $f_R = 0.15$ , as it remains unknown exactly what the correct value is for the chalcogenide composition considered here.

## 7.3 Importance of fiber dimensions

Early in the project different taper waists were considered that mostly were based on pitch and hole measurements in tapered chalcogenide fibers by [22], where three different pitch-to-hole ratios occur; 0.51, 0.43 and 0.37.

The motivation for investigating this was initially to be able to numerically design a tapered fiber that would give rise to the experimentally observed nonlinear dynamics described shortly. In particular it was believed that the presence of the second ZDW was the key to producing an observed dip in the power spectral density at around  $8 \mu\text{m}$ . Hence, being able to choose fiber

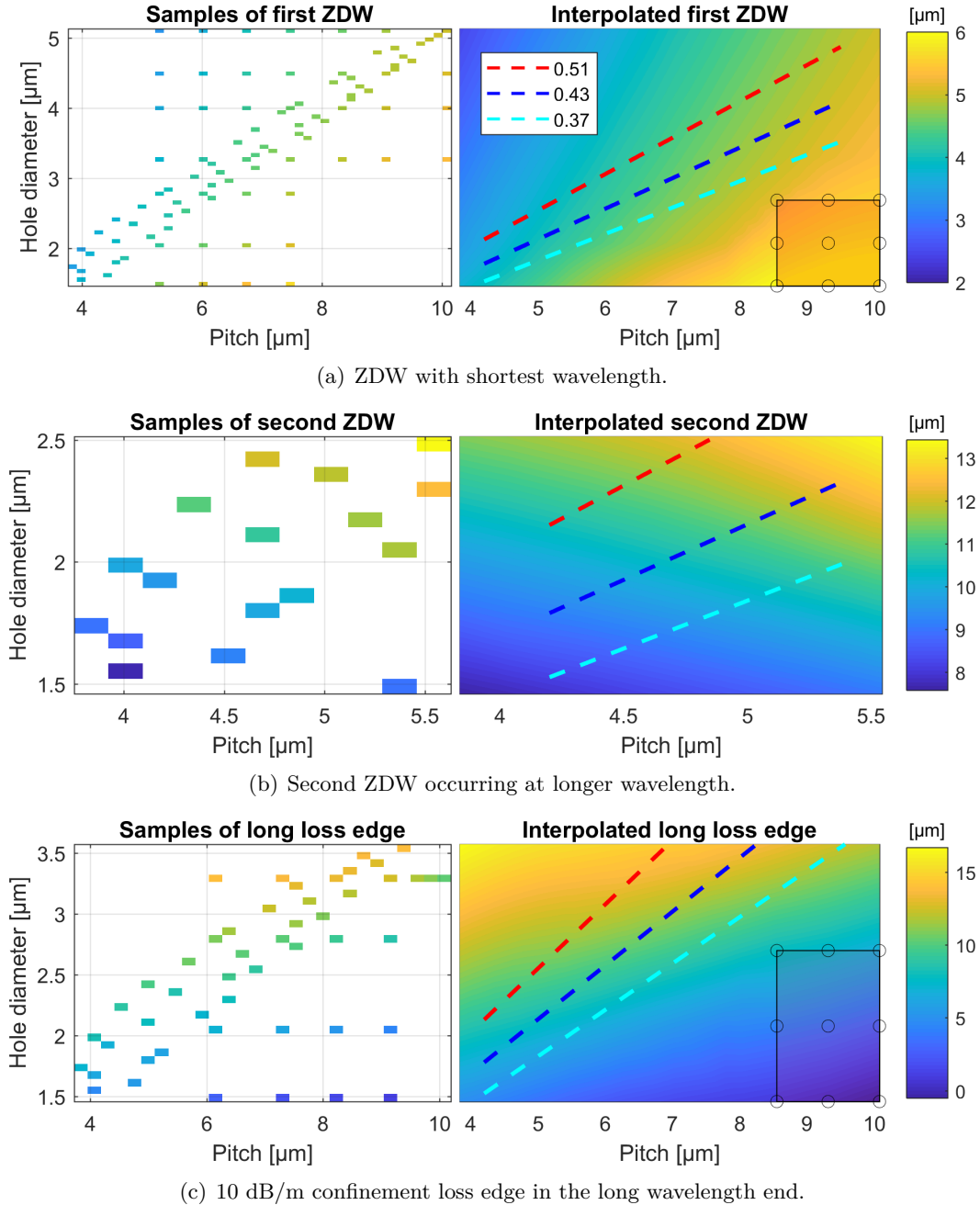


**Figure 7.6:** Interpolated first ZDW (top), second ZDW (mid) and long wavelength 10 dB/m loss edge (bottom) as functions of the taper dimensions; the pitch and hole diameter. The dashed lines indicate how tapers with different hole-to-pitch ratios will vary along the down/up taper. The shaded regions indicate parameters where no guided modes were found to exist.

dimensions to provide a second ZDW at an exact position was originally of interest.

Having solved the wave equation for several taper waists and the corresponding discretized down/up taper segments, the ZDW(s) could be determined and compiled into the grid shown in figure 7.6(a) and 7.6(b), where the latter shows the second ZDW for the solutions that have two ZDWs. The dashed lines indicate the direction of variation corresponding to different hole-to-pitch ratios, of which the 0.51 line is most close to the simulations we shall consider later in this chapter, where as noted in table 7.1 the hole-to-pitch ratio tends from 0.51 before the tapering to 0.48 in the taper waist. As was also seen on figure 7.4, the ZDW tends to reduce significantly along the down taper, eventually approaching  $\sim 3$   $\mu\text{m}$  in taper. In figure 7.4 only two of the nodes were found to have second ZDWs, at  $\sim 9$  and  $\sim 11$   $\mu\text{m}$ , but on figure 7.6(b) we see that the second ZDW can get as low as 8  $\mu\text{m}$  and as high as 13  $\mu\text{m}$  depending on the hole-to-pitch ratio.

However, when pushing the second ZDW into shorter wavelengths, say 8  $\mu\text{m}$ , by choosing fiber dimensions accordingly, the long wavelength loss edges will also shift, which turned out to be so significant as to extinguish the dynamics above 8  $\mu\text{m}$ . This loss dependency is shown on figure 7.6(c), where the long wavelength 10 dB/m loss edge is seen to be shifted all the way down to  $\sim 6$   $\mu\text{m}$  at parameters corresponding to a second ZDW at 8  $\mu\text{m}$ . Meanwhile, the 10 dB/m loss edge for the 0.51 hole-to-pitch ratio is closer to 10, and thus does not extinguish the dynamics around 8  $\mu\text{m}$  observed experimentally.

## 7.4 Reference experiment

An experiment that we will use as a reference for the majority of SCG simulations in this chapter is one conducted by Christian Rosenberg Petersen [22], in which a cut of the  $\text{Ge}_{10}\text{As}_{22}\text{Se}_{68}$  PCF similar to tapered fiber shown in figure 7.1 was pumped at different levels of power. Christian shared the data collected in this experiment allowing detailed comparisons between measurements and the simulation results in the following. The data from the experiment that has been deemed most relevant for the purpose of comparison has been visualised in figure 7.7.

The SC is seen to gain a lot of bandwidth at 16 mW pump power and above. At over 100 mW over pump power, the long wavelength part of the spectrum begins separating from the rest of the SC, evident in the three top figures of 7.7(a) and the small empty spaces in the interpolated plot in the top of figure 7.7(b). This separation is most clear for the highest used pump power of 190 mW, which in addition to having the broadest SC, features the most interesting dynamics of the shown cases, and will therefore form the basis of what we will attempt to reproduce. The spectrum corresponding to this pump power is enlarged in the bottom of figure 7.7(b).

## 7.5 Reproducing the experimental measurements

First and foremost the parameters that determine SC generation have to be carefully estimated. Most importantly the power and the nonlinear refractive index,  $n_2$ . What is decisive for the SC dynamics is the product between the power and  $n_2$ , and not so much the individual values.

Since we have previously estimated the value of  $n_2$  in the material, it seems appropriate to reuse this estimation, even though it was found to be somewhat different than the manufacturer's measured value. However, as stressed in the chapter describing this experiment the

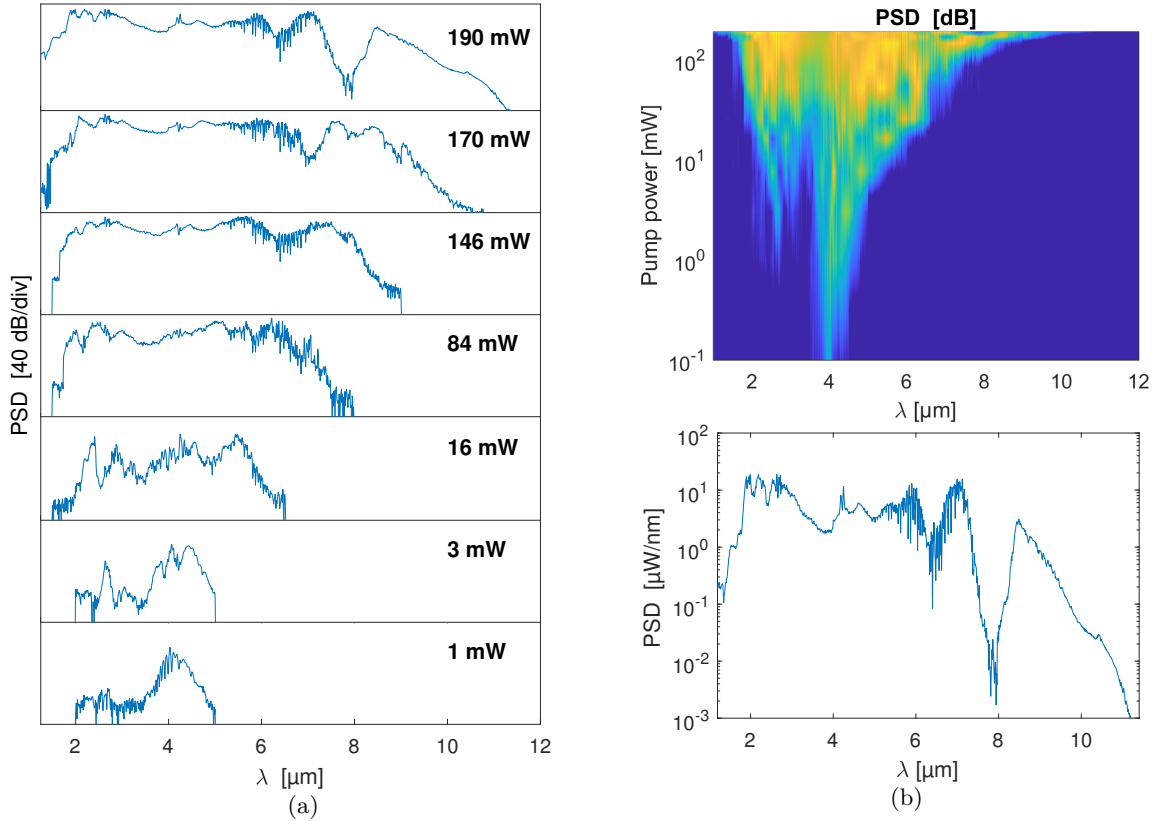


**Figure 7.7:** Experimental measurements of SC in a chalcogenide PCF. The annotations of the subplots of figure (a) indicate the pump power used to generate the SC. The seven power levels shown in (a), and four other spectra also in the interval between 1 mW to 190 mW, are all presented in the interpolated plot of figure (b). The most interesting result to try to reproduce is the broadest SC corresponding to the highest pump power, whose spectrum is enlarged in the bottom of (b).

value stated by the manufacturer was based on measurements at 1550 nm, whereas the experiment conducted in this project was at longer wavelengths. Since  $n_2$  is expected to decrease for increasing wavelength, it has been decided that the lower estimation of  $n_2$  is plausible, in fact even more so because we now will simulate at wavelengths up to 12  $\mu\text{m}$  with a pump laser at 4  $\mu\text{m}$ , more than double the wavelength at which  $n_2$  was estimated in the experiment. Due to this, the estimation of  $n_2$  at  $3.5 \cdot 10^{-18} \text{ m}^2/\text{W}$  is assumed now to have an even lower value of  $2.5 \cdot 10^{-18} \text{ m}^2/\text{W}$ , which will be used throughout this chapter. Again, the choice of  $n_2$  can be compensated for by the simulated power, and since we will vary the power greatly, this specific guess on  $n_2$  is not disruptive even if inaccurate.

As for the power, we can expect there to be Fresnel loss amounting to 19.5 % at both fibers end [22], and due to both material and confinement attenuation as seen on figure 7.5(a) and 7.4, there is likely to be propagation loss of 6 dB/m or more. The fiber length that will be simulated will span from 0.3 to 0.5 m, and so being conservative we estimate a propagation loss at 3 dB, yielding an overall transmission of 33 %.

The pump laser used in the experiment generates Gaussian shaped pulses with  $T_{\text{FWHM}} = 252$  fs. It has a repetition rate of 21 MHz, and in case of the highest pump power of 190 mW being used, this gives a peak power of 40 kW. Given the transmission above an estimate of the

simulated peak power is about 13 kW. For this reason we will start by considering propagation at this pump power, but later in the chapter we shall consider a larger range of pump powers, similarly to how it was done in the experiment. What we will find is that 13 kW is actually more than sufficient to see the characteristic dynamics observed in the experiment.

### 7.5.1 Attempting to reproduce with GNLSE

As a first attempt at reproducing the experimental result we will use the GNLSE (2.11) with the addition of attenuation, eq. (7.3), along with all the data presented in 7.4, which implies that we will let all quantities be frequency-dependent  $n_{\text{eff}}$ ,  $A_{\text{eff}}$  (and thus  $\gamma$ ) and  $\alpha$ . However, for now we will neglect the delayed Raman response function and set  $f_R = 0$ .

The simulation results obtained from solving this modified GNLSE are shown on figure 7.8. On the plot of the PSD during propagation several, the included guidelines represent: taper nodes (horizontal white), 10 dB/m loss edges (vertical white), maximal GVD (green) and ZDWs (red) – and they will be used as such in the rest of the chapter.

The measurement of the spectrum in the experimental reference of figure 7.7(b) corresponds to the PSD at the fiber that shown in the top 7.8(c). While the agreement is not great for wavelengths over 7  $\mu\text{m}$ , we see that the spectrum near the pump wavelength agrees reasonably well meaning that the estimated peak power of 13 kW seems to be appropriate.

The temporal evolution seen in figure 7.8(b) might at first sight seem a bit strange, especially when hold up against corresponding plots in chapter 4. The reason for this is that the velocity of the reference system has been chosen to be equal to the group velocity in the taper waist, which is lower than before the tapering causing the delay to be negative initially. As mentioned previously the velocity of the reference system can be chosen freely, and it would not affect the spectral development if chosen differently, and therefore this liberty has been exploited to minimise the overall delay allowing a smaller time window to be used, i.e. a smaller value of  $N_t$  as defined in section 3.2.

### 7.5.2 Attempting to reproduce with simplified MM-GNLSE

Moving on from the GNLSE, we will now as a second attempt use the MM-GNLSE, thus introducing the second polarisation mode, and again use all the frequency-dependent quantities of figure 7.4 while still neglecting the delayed Raman response.

In the presence of two polarisation modes, a choice regarding the initial polarisation has to be made, also referred to as polarisation seeding in the following. We can simply choose to have all the power in mode 1, in a way corresponding to the previous GNLSE simulation, except for the fact that the modes may now couple even if one of them has zero power initially. This is due to the term  $A_l^* [(R \cdot e^{2i\omega_0\tau}) * (A_m A_n)]$  in (2.16), which can cause the nonlinear effect known as four-wave mixing [13] giving rise to energy transfer between modes. Later in this chapter we will consider an example, where the term is removed from the MM-GNLSE. The simulation result for this case is seen on figure 7.9, in which the modes is indeed seen to couple. While initially having zero power, mode 2 catches up after the strong nonlinearity in the taper waist increases the rate of energy transfer greatly. This is also evident in figure 7.9(b), where the photon number of mode 2 is practically zero initially<sup>1</sup>, but quickly approaches an equilibrium

<sup>1</sup>The non-zero value is due to numerical truncation errors accumulating when computing the photon number integral.

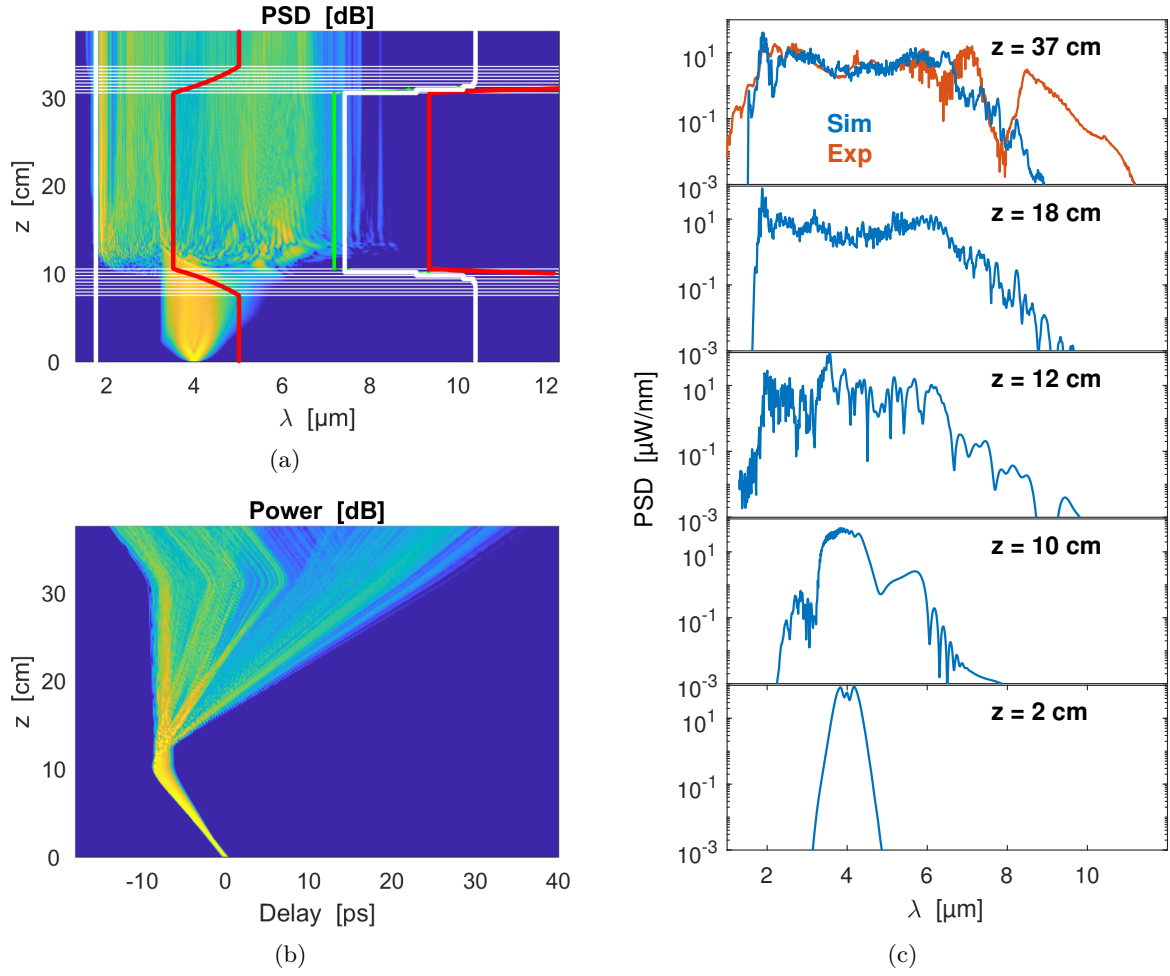


**Figure 7.8:** (a) PSD during propagation. (b) Time delay during propagation. (c) PSD at selected positions in the fiber with the position in the topmost plot being the fiber end, where the computed PSD is compared with the experimental reference, referred to as *sim* and *exp* respectively.

a bit into the taper waist.

For an initial condition where the modes equally share the initial peak power, the propagation plots are instead as shown in figure 7.10. With the two modes being seeded identically, and with the absence of delayed Raman, the differences in the PSD, figure 7.10(a), are subtle but definitely visible upon closer inspection. The difference is more evident on figure 7.10(b), in which the photon number of mode 2 is almost half that of mode 1 at  $\sim 13$  cm, despite being identical initially.

When comparing the PSD plots of figure 7.9 and 7.10 with those of the GNLSE in the previous section, figure 7.8, it is clear that the spectral development is very similar; there are no new dynamics suddenly emerging apart from the energy transfer between the modes, which however does not appear to be reflected by substantial changes in the PSD spectra. Hence, a combined PSD profile (i.e. the accumulated contributions from the modes) at the end of the fiber looks virtually identical to the one shown in figure 7.8(c), which brings us no closer to reproducing the experimental result. Common for all PSD plots seen so far it would appear that the long wavelength loss edge at around  $7 \mu\text{m}$  is an impenetrable barrier given that it

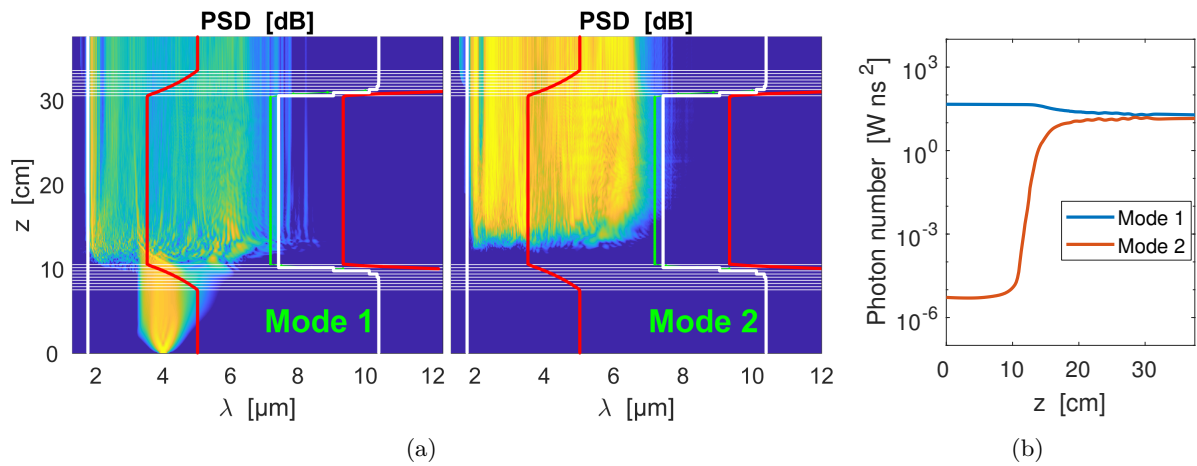


**Figure 7.9:** PSD (a) and photon number (b) during propagation for two differently seeded polarisation modes in the absence of delayed Raman response.

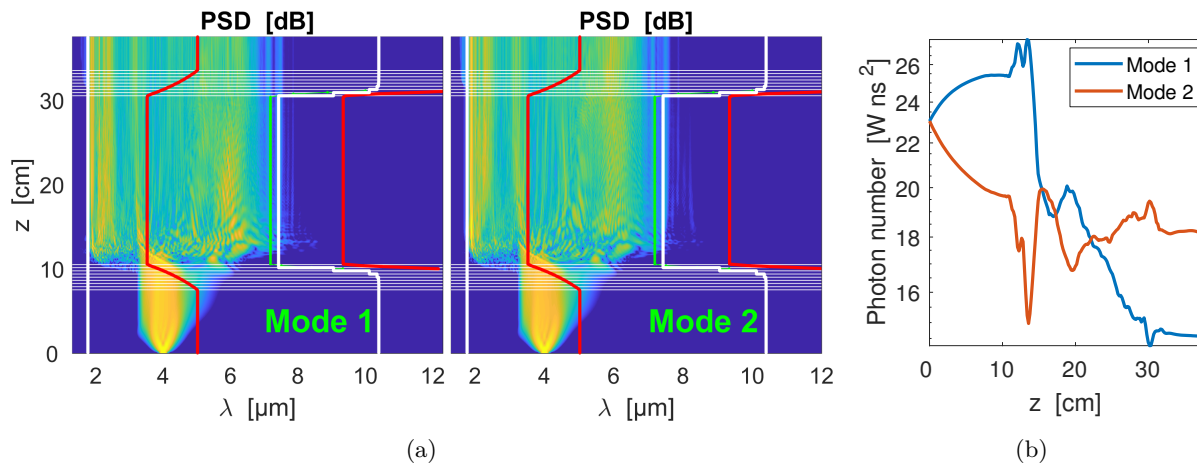


**Figure 7.10:** PSD (a) and photon number (b) during propagation for two equally seeded polarisation modes in the absence of delayed Raman response.

accurately coincides with the long wavelength edge of each supercontinuum.

As for the two different cases of initial polarisation seeding, we have not seen a significant difference either in terms of the spectral development, but then we have also neglected delayed Raman response so far.

### 7.5.3 Using full MM-GNLSE

Having simulated now the GNLSE and MM-GNLSE excluding the delayed Raman response, it is now time to simulate the full MM-GNLSE. Not knowing what the polarisation was in the experiment, we will assume that the polarisation modes have the same initial power, unless otherwise specified, because it seems unlikely that the pulse should have been completely polarised along one component in the experiment by chance.

Keeping all other parameters constant but now using the measured delayed Raman response

with the fractional Raman contribution being  $f_R = 0.15$ , the simulation results turn out completely different as seen in figure 7.11. We now see part of the pulse being redshifted through the barrier posed by the loss edge, and continues to propagate with significant power all until the fiber end. Furthermore, even with the similarly seeded modes, their PSD spectra are now quite distinct with mode 2 containing most of the spectral component that pierces through the loss edge, and mode 1 containing another spectral component that is also redshifted and is close to the loss edge.

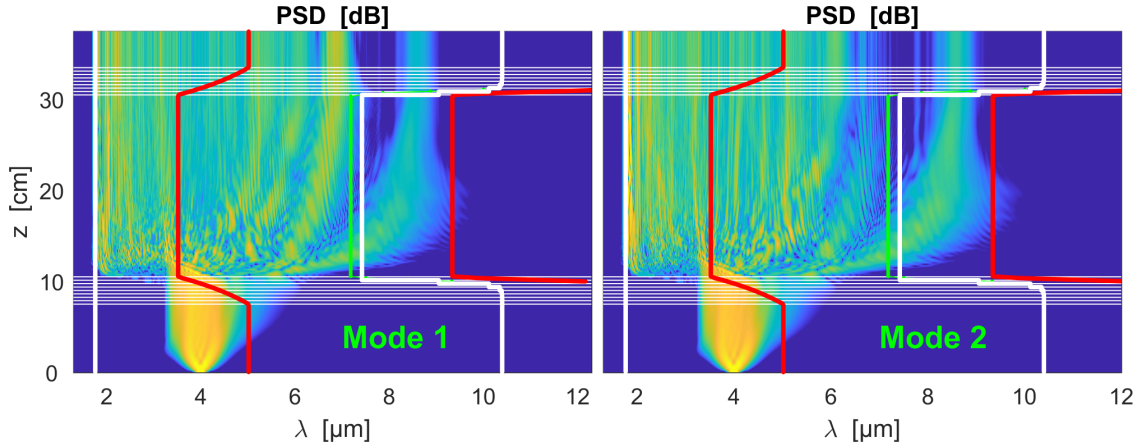


**Figure 7.11:** PSD during propagation of the respective modes when using the full MM-GNLSE.

The corresponding temporal development is seen in figure 7.12(a), where multiple components of the pulse can likewise be seen to separate from the rest of the pulse to wander off so to speak into increasing time delay. This spectral and temporal behaviour is reminiscent of some of the soliton dynamics that was explored in chapter 4. Hence, one might at this point hypothesise that what is seen here is indeed solitons. An investigation of this hypothesis will be undertaken shortly – first we will consider other characteristics of the new spectral development and how well it agrees with the experimental reference.

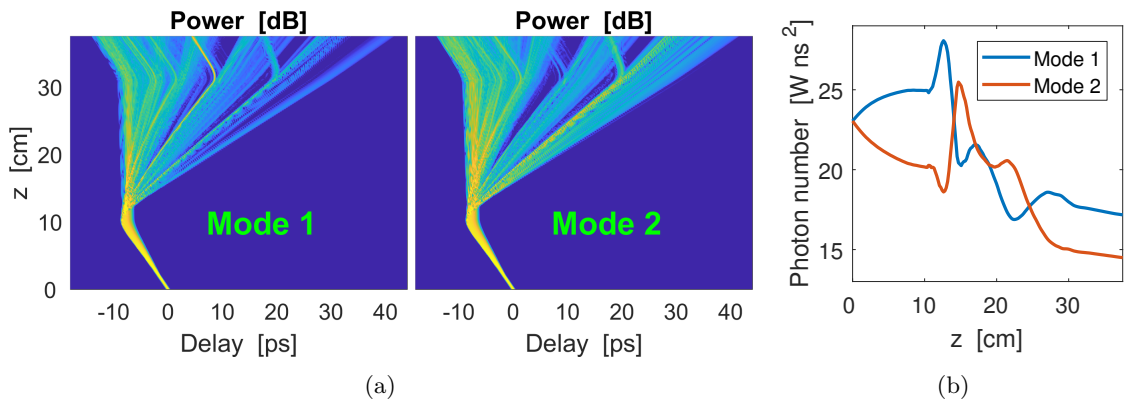


**Figure 7.12:** (a) Power in the time domain during propagation for the two polarisation modes. The time delay is defined with respect to the group velocity in the taper waist (which begins at 10 cm and ends at 30 cm). This is why the pulse moves faster than the reference frame initially and after the taper. (b) The photon number of the two modes during propagation.

During propagation the modes are seen to couple strongly with each other as evidenced by

the oscillating photon number in figure 7.12(b). The photon numbers of the modes do not quite reach an equilibrium, but they do end up relatively close with under 20 % difference. The PSD spectra at the fiber end do on the other hand end up quite distinct as shown on the left side of figure 7.13. Here the peak at 8+  $\mu\text{m}$  is seen to be broader and higher for mode 2 than for mode 1, which was also observed in figure 7.11 as well as the high peak in mode 1 at  $\mu\text{m} \sim 7$   $\mu\text{m}$ , which remarkably has no clear presence in mode 2.

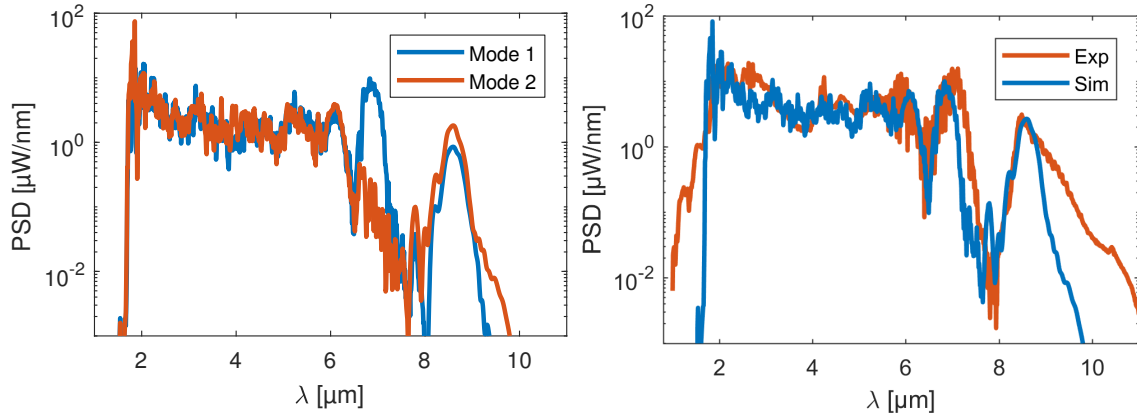


**Figure 7.13:** Comparisons of the PSD at the fiber end between the two polarisation modes (left) and between the combined PSD of the two modes and the reference experiment (right).

The combined PSD of the two modes is shown on the right side of figure 7.13 together with the experimental reference, and the agreement is seen to now be at an entirely different level of detail with three peaks at 6  $\mu\text{m}$ , 7  $\mu\text{m}$  and 8+  $\mu\text{m}$  being present in both curves. The peaks at 6  $\mu\text{m}$  and 7  $\mu\text{m}$  do not coincide exactly with the experimental reference, but the dip at 6.5  $\mu\text{m}$  certainly does, while the dip at 8  $\mu\text{m}$  and the peak at 8+  $\mu\text{m}$  also coincide very closely, with the latter being so close that the wavelength of the peaks only deviates by  $\sim 1$  %. One thing that differs somewhat between the simulation and experimental result is the long wavelength edge, which will be addressed after the next section.

### 7.5.3.1 Analysing the spectrogram

We now return to the hypothesis that the spectral development corresponds to soliton dynamics. A way to investigate this is by using the spectrogram defined by (2.28). The spectrogram for the full MM-GNLSE simulation at five different positions is shown on figure 7.14(a) with the corresponding PSD spectra in figure 7.14(b).

The soliton numbers  $N = \sqrt{\gamma P_0 T_0^2 / |\beta_2|}$ , indicated on the figure, have been estimated from the spectrogram along with a time domain plot of the power making it possible to read off the full-width half max (FWHM) of the peaks that are suspected to be solitons and will be referred to as such. The FWHM is then divided by  $2 \arccos(\sqrt{2}) \approx 1.76$  to give the pulse width  $T_0$ . The value for  $\beta_2$  is found from the propagation constant at the corresponding position in the fiber (i.e. the taper waist in both cases) using a finite difference approximation and interpolation to get the value at the wavelength indicated on the spectrogram. The power is found by integrating the power in the time domain in an interval that sufficiently encompasses the soliton pulse, which yields an energy that is converted to a power by division with the already estimated pulse width. Finally, the nonlinear coefficient is estimated using the definition  $\gamma = n_2 \omega_0 / (c A_{\text{eff}})$ . However, we note that  $A_{\text{eff}}$  is not completely well-defined in the current context, because the soliton is

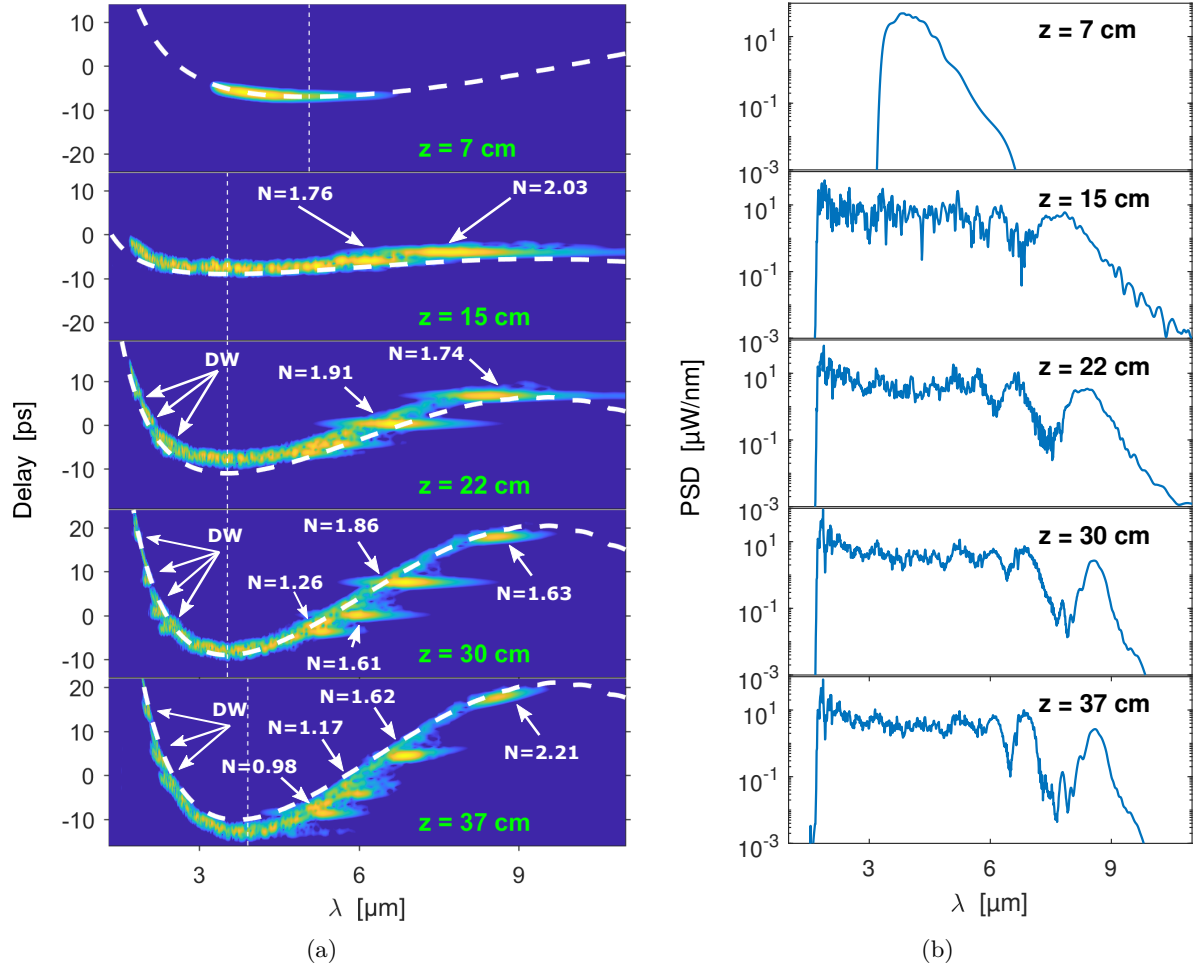


**Figure 7.14:** Spectrogram (a) and PSD (b) at five different position along the fiber, where  $z = 37$  cm is at the fiber end after the tapering, 7 cm is before the tapering and the three other positions are inside the taper waist. DW refers to dispersive waves, and  $N$  is the soliton numbers.

present in both polarisation modes and there are multiple overlap integrals between the modes, hence the ambiguity. However, the approximation  $Q_{1111}^{(1)}(\omega) \approx n_0^2 / [3n_{\text{eff}}^2(\omega)A_{\text{eff}}(\omega)]$  is used, which is true when there only is a single polarisation mode propagating with a real-valued mode function [13]. Due to this last uncertainty, the noted values for  $N$  are only suggestive.

As seen in chapter 4 fundamental solitons generated from soliton fission may be accompanied by dispersive waves. This appears to be the case in figure 7.14(a), where the suspected dispersive waves are indicated by the acronym DW.

The soliton numbers are overall close to 1, supporting the idea that they are fundamental solitons. The values tend to be consistent through the fiber, as we see no large changes at the four different positions in the figure. Furthermore the soliton number for solitons above 6  $\mu\text{m}$  seem to be a bit higher than the rest, which might indicate that the shortcomings of the approximation regarding  $A_{\text{eff}}$  are more pronounced at longer wavelengths.

The estimated values for the parameters  $\gamma$ ,  $P_0$ ,  $T_0$  and  $\beta_2$  for all the annotated solitons on figure 7.14(a) are listed in app. D, but two examples will be given here. For comparison purposes we will consider the large soliton already present at  $z = 15$  cm at around  $\lambda = 8$ , and

the smaller soliton that only starts to become present after  $z = 30$  cm at around  $\lambda = 5.5$   $\mu\text{m}$ . For the large soliton at  $z = 15$  cm, which is in the taper waist, the parameters were found to be  $P = 5.29$  kW,  $\beta_2 = -0.89$  ps<sup>2</sup>/m,  $T_{\text{FWHM}} = 0.08$  ps,  $A_{\text{eff}} = 35$   $\mu\text{m}^2$  yielding  $\gamma = 0.19$  (Wm)<sup>-1</sup> and  $N = 2.03$ . For the small soliton at  $z = 37$  cm, which is after the taper, the parameters were found to be  $P = 0.35$  kW,  $\beta_2 = -0.56$  ps<sup>2</sup>/m,  $T_{\text{FWHM}} = 0.22$  ps,  $A_{\text{eff}} = 120$   $\mu\text{m}^2$  yielding  $\gamma = 0.06$  (Wm)<sup>-1</sup> and  $N = 0.98$ . The higher (lower) value of  $A_{\text{eff}}$  ( $\gamma$ ) is not so much due wavelength dependency but rather that the after taper compared to the waist has much lower nonlinearity as seen previously in figure 7.4.

While there is more than a factor of 10 between the powers of those two solitons, the rest of the parameters are such that the soliton number only deviate by a factor of 2. The pulse width of the smaller soliton is a couple of times larger, which is likely due to higher-order dispersion whose effect is more pronounced the longer the fiber – the pulse width of the large soliton at  $z = 37$  cm has gone up to 0.6 ps for instance.

Finally, an observation regarding figure 7.14(b) is that the long wavelength edge is seen to extend further at 15 and 22 cm, also evident on figure 7.11, but due to confinement loss the long wavelength SC tail is attenuated as the pulse approaches the fiber end at  $z = 37$  cm ending up with a shorter tail than the experimental reference as seen in figure 7.13. This discrepancy will now be addressed.

#### 7.5.4 Matching the long wavelength loss edge

Now that it has been shown that the essential dynamics of the SC generation can be reproduced numerically, we can study some of the more minute differences with the experiment. One such difference is in the boundaries of the SC, especially the long wavelength end of the spectrum. The numerical results from modelling the fiber that was shown in figure 7.4, makes it clear that there tends to be sharp loss edges above 8  $\mu\text{m}$ . By comparison with the experiment, it does seem that those computed loss edges may be a bit too sharp. We will now investigate whether artificially reduced confinement loss, corresponding to shifted loss edges, might lead to better agreement in terms of boundaries while retaining the overall dynamics of the SC generation.

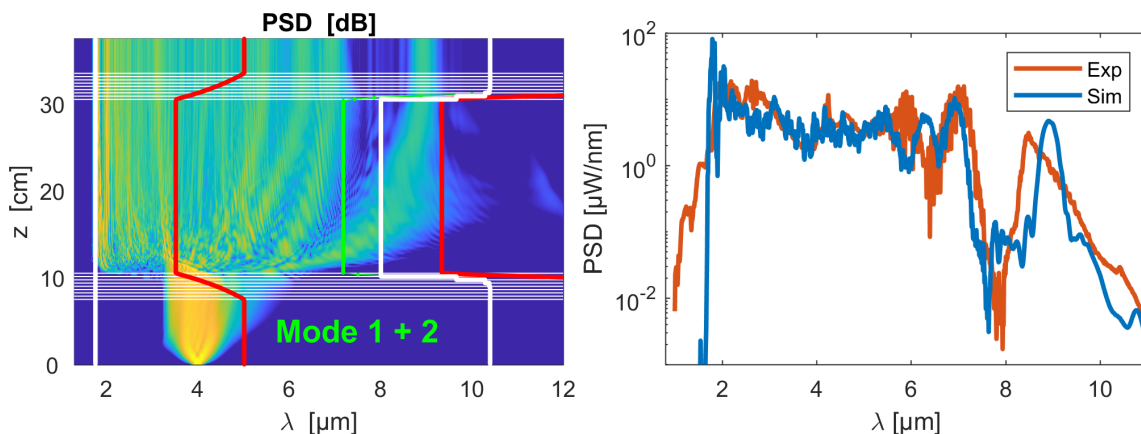


**Figure 7.15:** PSD during propagation (a) and at fiber end (b) when reducing confinement loss by a factor of 0.4.

We reduce the attenuation coefficient in the following way  $\alpha = k\alpha_{\text{con}} + r_{\text{glass}}\alpha_{\text{mat}}$  with  $k$  being a number between 0 and 1. This way only the confinement loss is altered, such that

only the long wavelength part of the SC is affected, and not the short wavelength part that is dominated by the material loss. Different values of  $k$  has been tried, but it was found that values lower than 0.2 leads to an unrealistic extension of the SC into 11+  $\mu\text{m}$  territory. An example of a simulation with  $k = 0.4$  is shown on figure 7.15. The long wavelength edge is certainly further into the infrared with the rightmost soliton peak surpassing that of the experimental result. At the same time this soliton is shifted to 9+  $\mu\text{m}$  wavelength, which does not agree as good with the experiment as before, nor does the central part of the spectrum from 4-7  $\mu\text{m}$ , but still this goes to show that an inaccurate confinement loss from the fiber modelling may give rise to the observed deviation of the long wavelength edges.

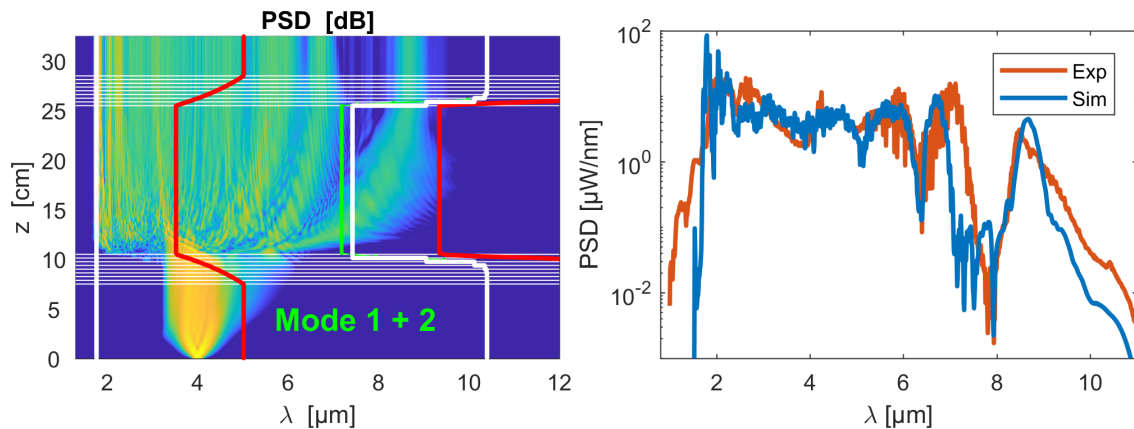


**Figure 7.16:** PSD during propagation (a) and at fiber end (b) when shortening the fiber waist by 5 cm.

Another parameter that influences the long wavelength loss edge is the taper waist length. Since the attenuation is very strong in the taper waist, a shorter waist length can also push the long wavelength edge further out. Naturally, the waist must not be so short as to inhibit the development of the SC, but based on previous propagation plots, we can easily cut 5 cm off the waist and still provide enough room for the SC development. As we have previously simulated a 20 cm waist, we will now consider propagation in a 15 cm waist instead of decreasing the attenuation coefficient as above. The PSD during propagation can be seen on the left in figure 7.16, and the comparison with the experiment on the right. From both of those figures it is clear that the long wavelength edge has been increased, and that this part of the spectrum is now in better agreement with the experiment, while the central spectrum is arguably in worse agreement than before. Note that a waist of 15 cm is still within the uncertainty of the measured length [22], but there is no justification for reducing it further, nor does it seem likely that it would improve agreement with the experiment anywhere but for the long wavelength.

Finally it is worth noting that the power can of course also be increased to push the long wavelength edge further, but this will change the rest of the spectrum very significantly as we shall see soon.

## 7.6 Dependence on power

We shall now see what happens, when the power is varied through a large range of values. In the experimental reference the pump power was varied from from around 1 mW to 190 mW, which based on the losses and laser properties mentioned earlier is estimated to correspond to

a range of pulse peak power from 80 W to around 16 kW. We will extend this range up to 22 kW, after which nothing particularly interesting have been found to happen.

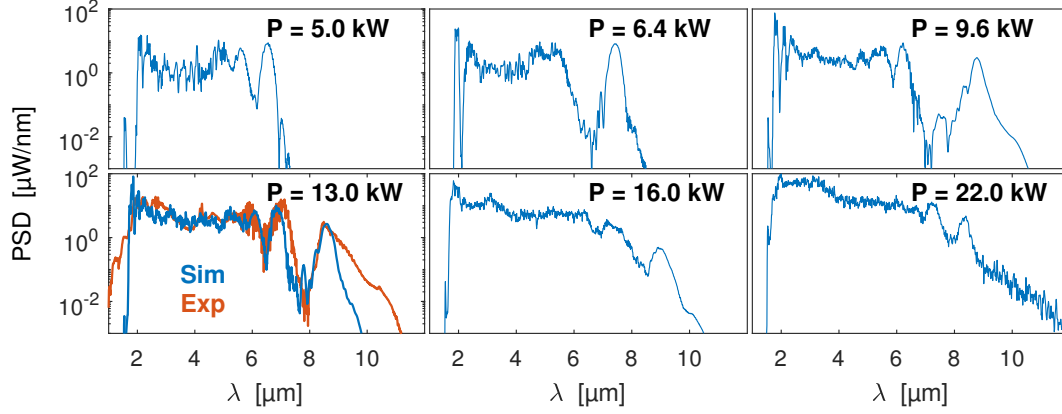


**Figure 7.17:** Variation of the peak power with other parameters kept constant at the values corresponding to the reference experiment that agrees best with the simulation for 13 kW peak power.

On figure 7.17 the spectra in the fiber end for six different peak powers are shown. For 5 kW the first soliton starts to redshift away from the rest of the pulse. The soliton redshifts further and gradually broadens as the power is increased up to 9.6 kW, where the second soliton starts to appear. The first soliton narrows from this point on, when increasing the power, while the second and third soliton catches up as seen in the 13 kW plot, the power at which the best agreement to the experimental result was found. For 16 kW the first soliton has less power compared to previous cases, presumably because it is redshifted so far into the long wavelength loss edge that the attenuation makes a clear mark. It is also possibly that the remaining pulse starts absorbing the soliton. This behaviour is even more evident for 22 kW, where only the soliton peak tops are visible.

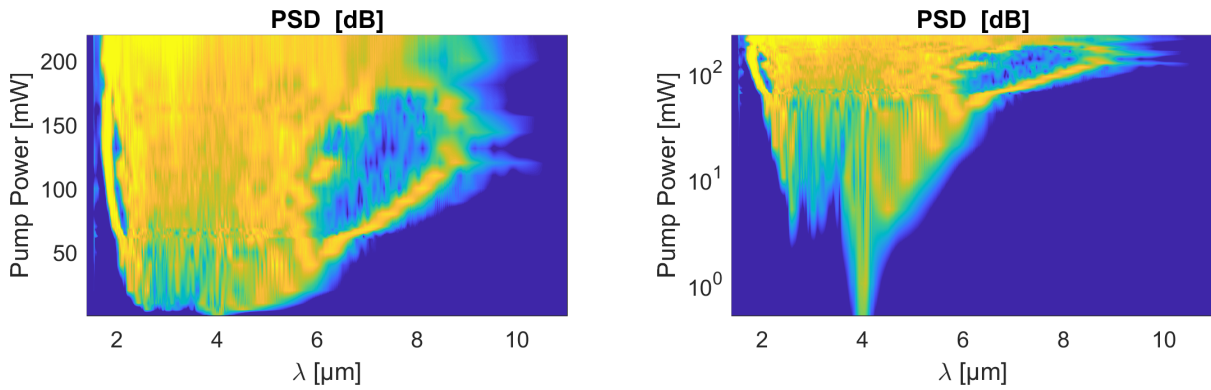


**Figure 7.18:** Interpolated PSD for 26 different values of average pump power on a linear (logarithmic) second axis to the left (right). The values for the average pump power are estimated based on expected losses and the properties of the laser used in the reference experiment.

Figure 7.18 features two visualisations of the end spectra for 26 different powers, the first of which has a linear axis of the pump power and the other one a log axis. The pump power is stated here rather than the peak power to make it comparable to the similar visualisation of the experimental measurement in figure 7.7(b) – the corresponding high end of peak powers are

similar to those on figure 7.17. On those two figures the gradual redshift of the first soliton is very clear with the peak's position moving along a tilted line into longer wavelengths leaving an empty space between it and the rest of the pulse. As was also seen on figure 7.17, the ultimate demise of the soliton at high powers is also clear, as we now see what almost looks like a collision with the strong loss edge at 9+  $\mu\text{m}$ . At pump powers over 150 mW, the SC becomes so broad that it fills the empty space between 6-8  $\mu\text{m}$ .

## 7.7 Sensitivity to important parameters

In this section we will see how the SC dynamics are influenced by changes to selected parameters that are identified to be important. It will not be a deep analysis but rather some examples of SC generated with different parameters that all lie within the uncertainty that is inherent to the parameter estimation in the first place.

The sensitivity to small changes in fiber lengths is overall not significant and not studied further. Down and up tapers as much as 2 cm longer or 1 cm shorter have been tried, and the results are very similar. The waist length has some importance, because the loss is relatively much higher, and therefore having a longer waist will reduce the long wavelength edge, as we have already seen. However, besides attenuation it is not a critical parameter, for instance a waist of 25 cm rather than 20 cm was found to produce very similar results, as well will a 15 cm waist. Of course a large reduction in the waist length will be detrimental to the SC generation, because the SC dynamics is still seen to develop within the first 10 cm of the waist in the previous propagation plots. The after taper length has very little importance, because both the loss and nonlinearity is relatively much smaller than in the waist, and therefore the pulse will essentially retain whatever form it had after the up taper. The before taper section is only influential on results if it is so long that the pulse power will have lost enough energy that the soliton fission does not happen. It does not matter if it is made a bit shorter though, because SPM will continue to happen in the waist until the rest of the dynamics follow.

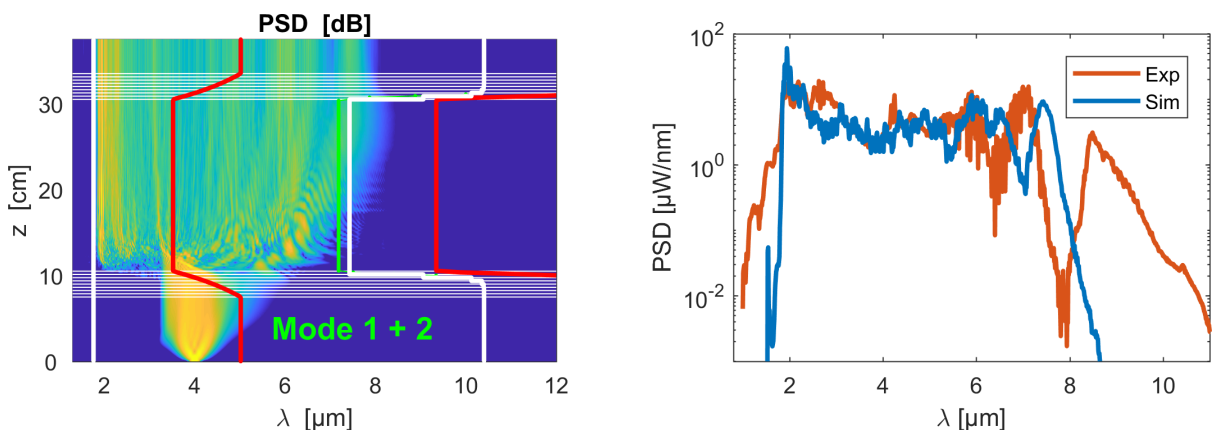


**Figure 7.19:** PSD during propagation (left) and at fiber end (right) when reducing the fractional Raman contribution from  $f_R = 0.15$  to  $f_R = 0.09$ .

### 7.7.1 Fractional Raman contribution

We will now consider an example, where the fractional Raman contribution is almost halved by decreasing the value to  $f_R = 0.09$ . The results presented so far have either had no delayed Raman response at all, i.e.  $f_R = 0$ , or have been based on  $f_R = 0.15$ . Keeping all other parameters as before, the decreased value of  $f_R$  leads to the simulation results shown in figure 7.19. It is clear that the Raman redshift of the longest wavelength soliton is now less pronounced, but is however still clear, especially when considering the PSD curve at the end of the fiber to the right of figure 7.19, where a clear dip now occurs as  $\sim 7 \mu\text{m}$  rather than  $8 \mu\text{m}$ . The second and third solitons are only slightly visible. With the less prominent redshift, the SC is overall more narrow, and clearly does not agree very well with the experimental, but even so the same dynamics must be said to still be visible as opposed to the case of no Raman at all, figure 7.10.

### 7.7.2 Initial polarisation seeding

The simulation results that have been presented so far have primarily been based on an initial condition with both polarisation modes having the same power, referred to as a 50/50 initial condition. We will now consider the other extreme, namely a 100/0 initial condition, i.e. when a single polarisation mode has all the power, to see whether the found agreement between simulation and experiment also applies to other initial conditions. The 100/0 initial condition gives rise to the simulation results shown in figure 7.20, where only the PSD of the second mode has been shown during propagation to emphasise the new initial condition, and because the PSD of mode 1 looks almost identical to the one shown on figure 7.11. Due to FWM, the energy transfer to mode 2 makes its associated PSD visible shortly into the taper waist – as with the other PSD plots the dB scales ranges from -40 to 0 dB, and therefore the PSD is at least  $10^{-4}$  smaller in the beginning of the taper waist compared to the middle of it. The energy transfer between the modes is very similar to the one seen in figure 7.9, where an equilibrium is almost reached near the fiber end.

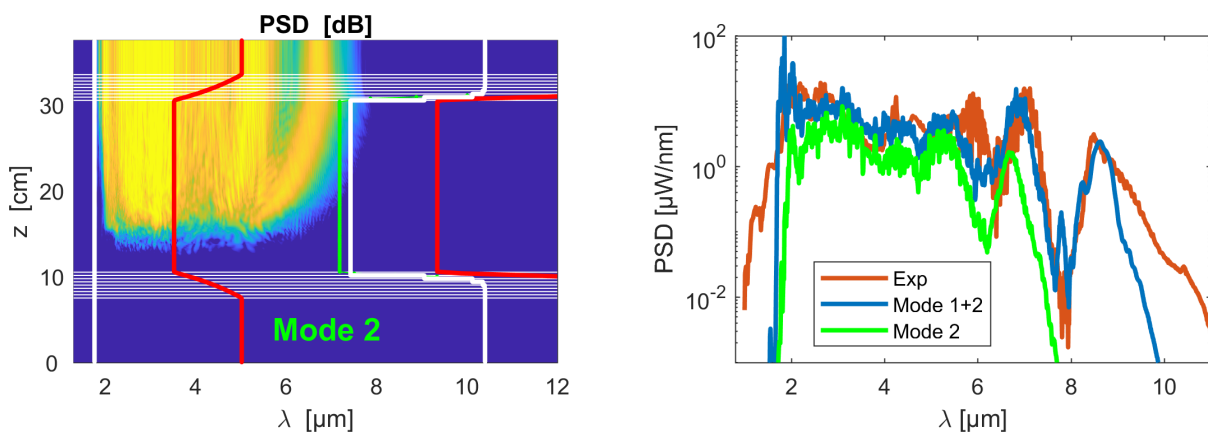


**Figure 7.20:** PSD during propagation of mode 2 (left) and PSD at fiber end (right) upon changing the initial condition of the polarisation modes from 50/50 to 100/0.

Interestingly, the PSD of mode 2 only shows the soliton referred to previously as the second soliton occurring at  $\sim 7 \mu\text{m}$ , and does not have the so-called first soliton that appeared at  $8+ \mu\text{m}$  before. The  $8+ \mu\text{m}$  soliton is however very clear in mode 1, which is evidenced by the combined PSD (mode 1 + 2) to the right of figure 7.20. When considering the combined PSD,

the agreement with the experiment is still very good qualitatively, and therefore we conclude that the initial condition is not crucial to reproducing the experimental results.

### 7.7.3 Fiber dimensions

Now we will consider what happens if the pitch and hole diameter in the taper waist are a bit smaller, but the hole-to-pitch ratio remains the same. All other parameters are kept the same. The pitch is reduced by  $0.1 \mu\text{m}$ , from  $3.91$  to  $3.81 \mu\text{m}$ , while the hole diameter is reduced  $0.06 \mu\text{m}$ , from  $1.89$  to  $1.83 \mu\text{m}$ , yielding a hole-to-pitch ratio that is unchanged. Different hole-to-pitch ratios have also been tested, but the consequence of changing the hole-to-pitch ratio in the waist is mainly characterised by shifting the loss edges as discussed in section 7.3.

The simulation results that follow from the changed fiber dimensions are shown on figure 7.21. At the plot to the left in figure 7.21 the long wavelength loss edge can be seen to be just slightly shifted towards shorter wavelengths, which is presumably what causes the  $8+$   $\mu\text{m}$  soliton to be a bit narrower and less redshifted compared to before as seen to the right of figure 7.21. The second soliton occurring at  $7 \mu\text{m}$  is seen to now agree remarkably well with the experiment, although this is likely just a coincidence given that the rest of the spectrum does not agree very well. Although the dynamics largely being the same as before, a significant difference is seen, and based on this it might have been worthwhile to investigate fiber dimensions just a bit larger instead of smaller as it could possibly lead to a matching of the long wavelength edge of the SC to the experiment similarly to what was achieved by other means in section 7.5.4.

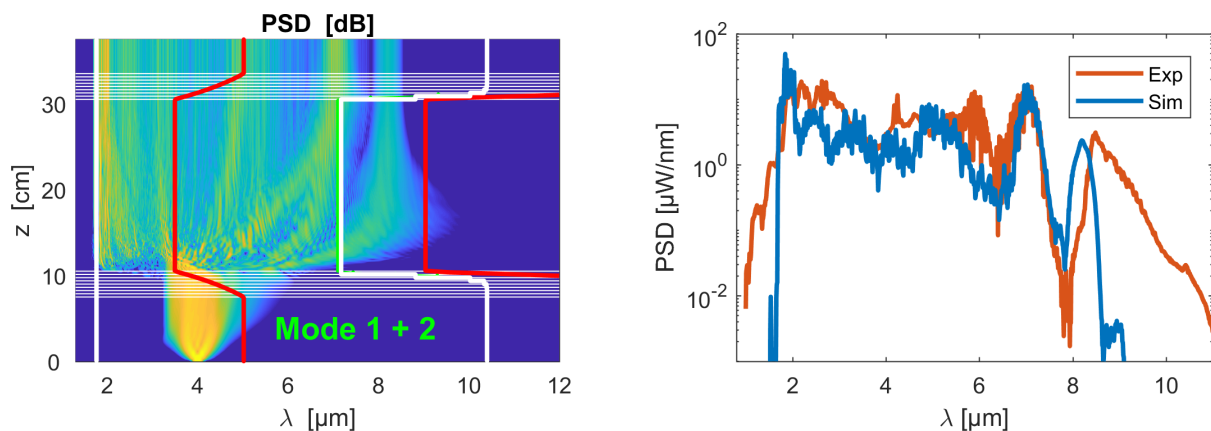


**Figure 7.21:** PSD during propagation (left) and at fiber end (right) when reducing the pitch and hole diameter of the PCF by  $0.1$  and  $0.06 \mu\text{m}$ , respectively.

## 7.8 Variations of the MM-GNLSE

In this section we will consider the consequences of two modifications to the MM-GNLSE. Similarly to the sensitivity analysis of the parameters, the purpose is here to investigate whether the found agreement with the experimental reference is peculiar to the particular form of the MM-GNLSE that has been used or if the associated dynamics are more general. The investigation is not thorough as we will just consider an example of each modification.

### 7.8.1 Excluding four-wave mixing

First we will consider what happens when there is no four-wave mixing in the MM-GNLSE. Of course we could just completely remove the  $Q_{plmn}^{(2)}$  term in the MM-GNLSE, equation (2.16), and another modification with the same effect is to change the conjugations of the field envelopes in this term to reflect the  $Q_{plmn}^{(1)}$  term, i.e. from  $A_l^* [(R \cdot e^{2i\omega_0\tau}) * (A_m A_n)]$  into  $A_l [(R \cdot e^{2i\omega_0\tau}) * (A_m A_n^*)]$ .

The consequence of this change is that the polarisation modes are now energy conserving individually [13], and for that reason if we use the initial condition that the polarisation start is 100 % aligned with mode 1, then there will be no development in mode 2 under propagation. This is shown on figure 7.22.

The dB scale on the mode 2 plot is relative to the initial PSD of mode 1, but it ranges all the way from -100 to 0, nearly three times greater range than for other figures featuring dB scales in the thesis. Even so, we hardly see any development during propagation, which is also clear on the photon number plot that shows a difference of 8 orders of magnitude. The non-zero photon number of mode 2 can be ascribed to numerical truncation errors that accumulate when computing the photon number integral. While this must definitely be the reason for the non-zero photon number initially in the fiber, given the initial condition, there appears to be slight increase after 10 cm of propagation. Whether this is due to an extremely weak energy transfer, perhaps resulting from the shock term, is unknown, but it does seem more likely that the accumulation of numerical errors becomes more significant in the taper waist at 10 cm. Nonetheless, this case goes to illustrate that energy transfer is effectively zero without FWM. The spectral development in mode 1 does show the same dynamics as when FWM is present however, but evidently when using the same parameters as before, the agreement with the experiment is worse as seen to the right of figure 7.22.

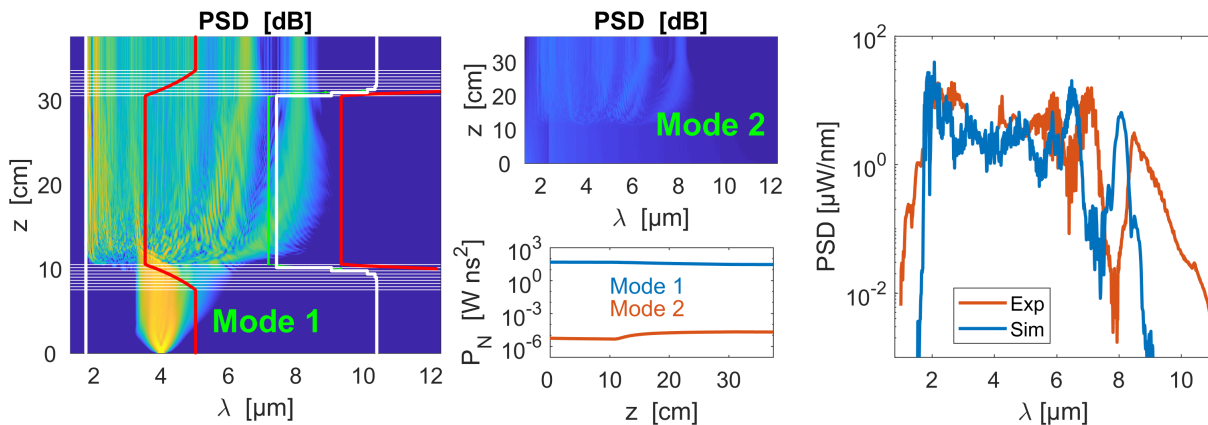


**Figure 7.22:** Left and top-mid plot show the PSD of the respective modes. Due to the initial condition and the absence of FWM, the inter-mode energy transfer is not in effect, rendering mode 2 idle during propagation, which is also seen by the 8 orders of magnitude lower photon number, abbreviated  $P_N$ , in the bottom-mid plot. The plot to the right shows a worse agreement with the experiment.

### 7.8.2 Including higher-order shock terms

We will now briefly consider the effect of including the higher-order contribution of the  $\tau_{plmn}^{(1,2)}$  terms in the MM-GNLSE, which in the case of simulating two polarisation modes gives rise to

32 separate shock time constants. Upon computation it is confirmed that  $1/\omega_0$  is indeed the dominant term, and therefore it should be no surprise that the previously seen dynamics are still present when simulating the propagation – see left side of figure 7.23. In this simulation the two modes were seeded equally initially, and since the spectral development are similar for the modes, only the total PSD is plotted in the figure. While the left side of figure 7.23 shows no new dynamics, the long wavelength soliton is now less redshifted, which is also evident when considering the PSD curve at the end fiber shown in the right side of figure 7.23, where the PSD found when using the approximation  $\tau_{plmn}^{(1,2)} = 1/\omega_0$  has been included for comparison.

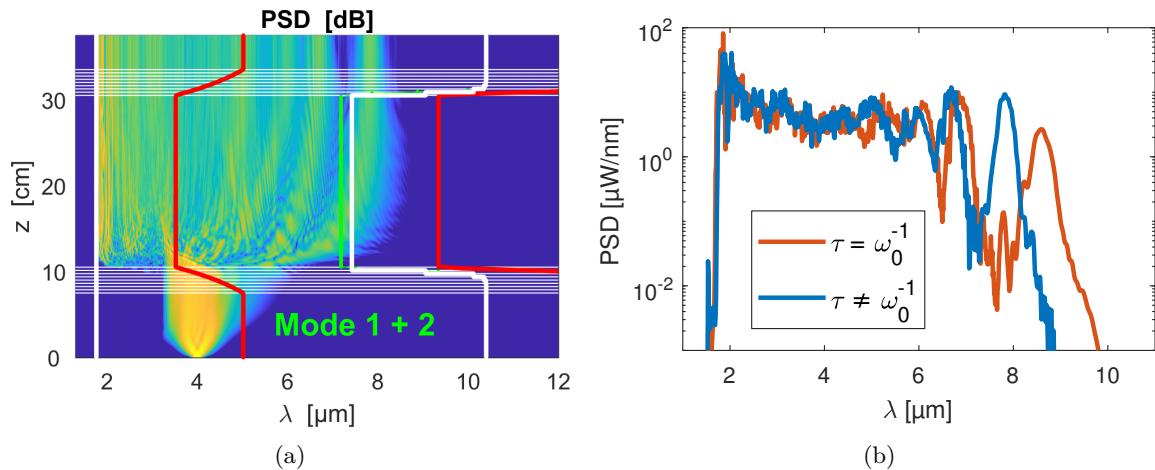


**Figure 7.23:** PSD during propagation (a) and at fiber end (b) when including higher-order shock terms.

The shock term is often associated with an effect known as self-steepening [7], in which the group velocity is intensity-dependent. This causes the group velocity in the pulse peak to be lower than in the wings resulting in a distortion, where the time delay of the peak increases towards the trailing edge, which is seen as a steepening in the time domain. Self-steepening is expected to occur both with and without the approximation, but it is less prevalent when not using the approximation, which is clear when plotting the SC in the time domain at the end of the fiber as seen on figure 7.24, where the red curve is more steep in the trailing edge.

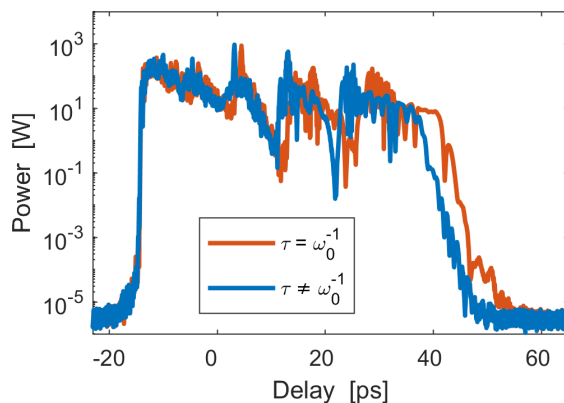


**Figure 7.24:** The curve for the simulation result where the  $\tau = 1/\omega_0$  approximation was used shows a more significant self-steepening indicating the the higher-order terms of  $\tau$  cause the overall shock time constants to decrease in value.

Even if the higher-order shock terms do seem to be of some importance, there are various proposals as to how they should be modelled [7, 2, 13, 15], and this diversity has spawned a bit of uncertainty towards including them, which is why the simpler model with the approximation

---

$\tau_{plmn}^{(1,2)} = \omega_0$  has been preferred and is used through-out the thesis. It is worth pointing out that while the right side plot of figure 7.23 may suggest that a better agreement between experiment and simulation is found when not including the shock terms, there may definitely exist a set of the uncertain and important parameters that will give an equally good agreement – those parameters include the power, the fractional Raman contribution and taper dimensions.

# CHAPTER 8

## Conclusion

---

The topic of supercontinuum (SC) generation has been studied from many sides. From a modelling and numerical perspective, the problem of describing and simulating SC generation has been addressed all the way from modelling photonic crystal fibers (PCF) by solving the wave equation with COMSOL to designing numerical integration schemes that efficiently solve the nonlinear propagation equations, such as the GNLSE and, its extension, the MM-GNLSE.

Chalcogenide fibers of the composition  $\text{Ge}_{10}\text{As}_{22}\text{Se}_{68}$  have been studied both experimentally and numerically. Two experiments have been conducted with the chalcogenide fiber each one with the purpose of determining a parameter either to be compared to or used in the modelling. The first of those experiments dealt with the dispersion in the fiber. An interferometry based method, inspired by [25], featuring a supercontinuum laser source was used to record interference fringes from which the dispersion can be derived by fitting to a variant of Cauchy's equation using a least squares method. The process was repeated several times, each time with a slight modification to the setup that would shift the interference fringes and produce a new fit of the dispersion. Upon taking the average of all such obtained fits, the final estimation of the dispersion was then compared to predictions from modelling. Those predictions were computed by solving the wave equation with COMSOL based on measurements of the chalcogenide PCF dimensions by microscope. The averaged dispersion fit from the experiment was found to be completely within the uncertainty of the numerical modelling that stem from the uncertainty of the fiber dimensions measurement. This agreement is taken to be a validation of the numerical modelling, which can then be trusted to provide accurate results when simulating variants of the same chalcogenide PCF with different dimensions as in tapered fiber simulations described shortly. A direct measurement of the ZDW was not possible as it happened to be outside the bandwidth of the SC source used, but based on extrapolation from the dispersion fit, the ZDW was found to be within  $\sim 2\%$  of the numerical prediction.

In the other experiment the self-phase modulation (SPM) in the fiber was recorded in an attempt to estimate the nonlinear refractive index,  $n_2$ , of the chalcogenide composition by fitting with a numerical simulation using  $n_2$  as a free parameter, while other parameters being estimated as accurately as possible. The resulting value for  $n_2$  at a wavelength of  $1.93\ \mu\text{m}$  was found to be  $3.5 \cdot 10^{-18}\ \text{m}^2/\text{W}$ . The value of  $n_2$  provided by the fiber manufacturer, SelenOptics, is  $8.8 \cdot 10^{-18}\ \text{m}^2/\text{W}$  at  $1.55\ \mu\text{m}$ , and while the value found in the experiment is significantly lower, reductions of over  $50\%$  has also been found for multiple other chalcogenide compositions when increasing the wavelength from  $1064\ \text{nm}$  to  $1430\ \text{nm}$  [26]. Hence, even with the considerable uncertainty of our estimation due to the nature of the approach, the value may in fact be plausible, and so it has been used for the simulations of the chalcogenide performed in the latter part of the thesis.

Those simulations have formed the main focus of the thesis with the chapters on modelling, numerical analysis and the experiments having provided a foundation for simulating multimode

pulse propagation in tapered fibers that is validated, tested and shown to be convergent<sup>1</sup> as well as optimised to perform superiorly compared to other methods. This optimised method, referred to as the DPIP method, has been developed during the project drawing inspiration from the RK4IP method in [18] but shown to eclipse the RK4IP method in terms of convergence rate and computational efficiency.

The simulations of multimode pulse propagation in tapered fibers revolved around the chalcogenide fibers measured upon in the experiment. Tapered version of these fibers are studied in an experiment [22], where broad mid-IR SC is generated by pumping with high average power. The parameters used in this experiment have formed the basis on which all tapered fiber SC generation simulations have been made in an attempt to reproduce the findings of the experiment. When using the MM-GNLSE proposed in [13] with two polarisation modes, and all parameters as in the experiment, the simulation predicts the formation of multiple redshifted fundamental solitons – that have been confirmed to be solitons through an analysis of the spectrogram at different positions in the fiber revealing that the soliton numbers are relatively close to 1 and do not change significantly during propagation. The peaks of those solitons as well as the dips between them coincide very well with the observed peaks and dips of the experimental reference, which implies with considerable certainty that the spectral development seen in the experiment is in fact due to soliton dynamics.

---

<sup>1</sup>All steps in the chain of numerical problems that are necessary to solve in order to simulate propagation in tapered fibers have been shown to be convergent: the numerical modelling of the fiber, the numerical integration scheme employed to solve the propagation equation, and the discretization of the tapered fiber.

# APPENDIX A

## The DPIP method

The DPIP (Dormand-Prince Interaction Picture) method is based on the Dormand-Prince Runge-Kutta scheme defined by the so-called Butcher tableau shown in table A.1.

A transformation similar to the one shown for the RK4IP method is used, but not the separation distance is a full step size rather than a half, i.e.  $z' = z + h$ . The reason that this choice is advantageous is due to the sixth and seventh stage being evaluated here (shown in the Butcher tableau as the two rows with a coefficient of 1 in the first column), where the interaction and normal picture will coincide and thus save FFTs by eliminating the need of transformations for these stages.

The first row of coefficients below the horizontal line in table A.1 gives the fifth order solution, and the second row gives the alternative fourth order solution. The embedded error estimate is then given by the absolute difference of the two solutions.

**Table A.1:** Butcher tableau of the Dormand-Prince integration scheme

0							
1/5	1/5						
3/10	3/40	9/40					
4/5	44/45	-56/15	32/9				
8/9	19372/6561	-25360/2187	6448/6561	-212/729			
1	9017/3168	-355/33	46732/5247	49/176	-5103/18656		
1	35/384	0	500/1113	125/192	-2187/6784	11/84	
	35/384	0	500/1113	125/192	-2187/6784	11/84	0
	5179/57600	0	7571/16695	393/640	-92097/339200	187/2100	1/40

# APPENDIX B

## Unchirped SPM fits

The unchirped fits from the SPM experiment is shown in figure B.1.

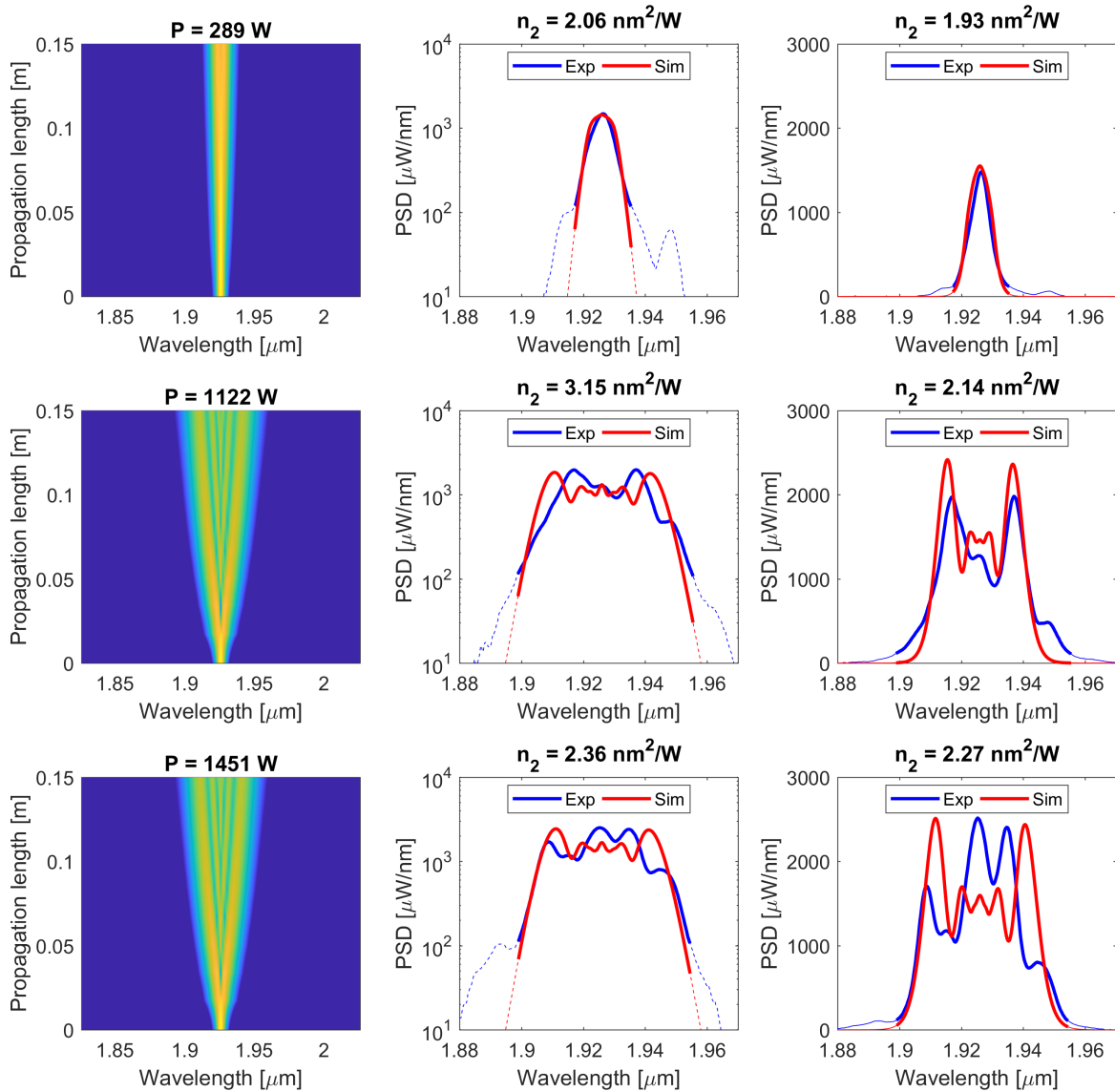


**Figure B.1:** Optimal fits for SPM measurement assuming unchirped pump laser pulses. The deviation between fit and measurement, both logarithmically and linearly, is larger than when assuming chirped pulses, and the resulting value of  $n_2$  is lower – further away from the expected value.

# APPENDIX C

## Implementation of MM-GNLSE solver

The implementation has been made in Matlab due to its excellent balance between performance and high-level programming. A smaller C++ implementation was also developed and although its speedup was significant, a factor of 2-3 using a parallel implementation of the FFT (the library FFTW), the increased development time and more messy code ultimately made Matlab the preferred option.

The solver is conveniently partitioned into different logical parts, of which the most essential ones are shown in this appendix, namely `CCS_Main.m`, `CCS_Param.m`, `CCS_Fiber.m`, `CCS_GetCOMSOLData.m` and `CCS_Integrator` – functions for plotting and postprocessing have been omitted. The overall logic of the implementation is contained in `CCS_Main.m`, which calls the above functions – see listing C.1. Every piece of input is contained in `,CCS_Param.m`, a file that can be copied into a subfolder for every batch job (was done automatically via a bash script) to allow for simultaneous computations with different configurations, see listing C.2.

The fiber configuration that is simulated is described by the function `CCS_Fiber.m`, shown in listing C.3. Based on this fiber configuration, save files from COMSOL are loaded and processed into appropriate data structures in the function `CCS_GetCOMSOLData.m`, see listing C.4.

Finally, the most interesting function is `CCS_Integrator.m`, which solves the MM-GNLSE propagation equation – the associated code is shown in listing C.5.

**Listing C.1:** Content of `CCS_Main.m`.

```
%% Init
CCS_Param

%% Fiber init
5 [ztarget,taper_zlist,COMSOL_Filenames] = CCS_Fiber(FiberType,rend);

%% Preprocessing
[D_c,Q_c,gsTerms,taus] = CCS_GetCOMSOLData(P,COMSOL_Filenames,LossFile);
P.gsTerms = gsTerms;
10 P.taus = taus;

%% Processing
zlist = linspace(0,ztarget,P.Nz);
[Z,ATZ_p,ext] = CCS_Integrator(P,(A),zlist,taper_zlist,D_c,Q_c,opt);
```

**Listing C.2:** Content of `CCS_Param.m`

```
%% Discretization
P = struct();
P.Nt=2^15;           % Number of time steps, 2^N makes fft faster
P.dt=4.84e-15;      % Time step [s], note dt>pi/w0 to avoid negative frequencies
5 P.Nz = 200;       % Save points

%% Physical constants
P.c = 299792458;    % Speed of light [m/s]
P.eps0=8.854*10^(-12); % Vacuum permittivity [F/m] (for Q1 and Q2)
10 hbar=1.0545718*10^(-34); % Planck Constant [m^2*kg/s] (for noise)

%% Data structures
```

```

P.T=(-P.Nt/2:P.Nt/2-1)*P.dt.';
P.V=2*pi*(-P.Nt/2:P.Nt/2-1)/(P.Nt*P.dt);
15 P.Vshift = fftshift(P.V);
P.dV = P.V(2)-P.V(1);

%% Functions
20 P.fftc = @(TD) (ifft((TD))*fscale);
P.ifftc = @(FD) (fft((FD))*iscale);
P.fftscale = P.Nt*P.dt;

%% Fiber/laser parameters
25 P.wpump = 2*pi*P.c/4e-6; % Pump angular freq. [s^-1]
P.w0 = 2*pi*P.c/2350e-9; % Expansion angular freq. [s^-1]
power=5600; % Pulse peak power [W]

t0 = 0.212e-12; % Pulse width [s]
30 P.n2 = 2.5e-18; % Nonlinear refractive index [m^2/W]
P.Nmodes = 2;
rend = 0.48; % Taper profile (for Fiber function)
FiberType = 'smallBTAT'; % Taper length configuration
% FiberType = [0.075 0.03 0.2 0.03 0.04]; % alternative def.
35

% Raman (showing analytical approximation here as an example)
P.fr = 0.15;
tau1 = 23.1e-15; tau2 = 195e-15;
P.RT = (tau1^2+tau2^2)/tau1/tau2^2*exp(-P.T/tau2).*sin(P.T/tau1);
40 P.RT(P.T<0) = 0; % Heaviside step function
P.RT=P.RT/trapz(P.T,P.RT); % Normalise
P.RW = (3/2*P.fr*P.fftc(fftshift(P.RT))); % Frequency domain Raman, included factor 3/2*fr
for numerical efficiency
P.RWexp = (3/2*P.fr*P.fftc(fftshift(P.RT.*exp(2*i*P.w0*P.T)))); % Raman for Q2 term in MM-
GNLSE

45 % Loss file
LossFile = 'ParameterData/LossData_Chalc_WithExpExtension_v2';
P.alphaCoeffA = 1; % artificial scale of confinement loss
P.alphaCoeffB = 1; % artificial scale of material loss

50 % gamma and shock term data structures
P.useAllShockTerms = 0; % whether to use tau_plmn
P.gsTerm = cell(1); % gs = gamma & shock, modified in GetCOMSOLData function
P.tau = cell(1); % shock time constants, modified in GetCOMSOLData function
P.gsCoeff = 0; % whether to include higher order shock terms when useAllShockTerms =
0

55 % Should Q overlap integrals be continuous? Akin to mode profile dispersion
P.MPD = 1;

%% Input pulse
60 Mode1Seed = 0.50; % Initial power fraction of mode 1

A=zeros(P.Nt*P.Nmodes,1);
if P.Nmodes > 1
    A(1:P.Nt)=sqrt(Mode1Seed*power)*exp(-P.T.^2/t0^2).*exp(-1i*(P.wpump-P.w0)*P.T); % Chirp
65 A(P.Nt+1:end)=sqrt((1-Mode1Seed)*power)*exp(-P.T.^2/t0^2).*exp(-1i*(P.wpump-P.w0)*P.T); %
    Chirp
else
    A(1:P.Nt)=sqrt(power)*exp(-P.T.^2/t0^2).*exp(-1i*(P.wpump-P.w0)*P.T); % Chirp
end

70 % One photon per mode noise
if exist('ArrayID','var'), rng(ArrayID,'Twister'); end % for ensemble averaging in batch
processing
RandNoise=exp(1i*rand(length(P.V)*P.Nmodes,1)*2*pi)...
.*sqrt(1/P.dV*hbar*repmat((P.V+P.w0),[P.Nmodes,1]));
Rifft=MMifftc(RandNoise,P.Nt,P.Nmodes); % important to do proper iFT with scaling

```

```

75 A = A+Rifft;

    %% Solver parameters
    opt = struct();

80 opt.dz = 5e-5;
    opt.useAdapt = 1;
    opt.useAdapt_RKerr = 1;
    opt.useAdapt_mindz = 2.5e-5;
    opt.useAdapt_maxdz = 1e-3;
85 opt.tol = 3e-4;
    opt.solver = 2;

```

Listing C.3: Content of CCS\_Fiber.m

```

function [ztarget,taper_zlist,COMSOl_Filenames] = CCS_Fiber(FiberType,rend)

switch rend % only showing one case as an example
    case 0.48
5         dRings=[5.1, 4.69181, 4.28579, 3.88196, 3.48035, 3.08097, 2.68384, 2.28899, 1.89642]*1
            e-6;
            LList=[10.08, 9.3261, 8.5679, 7.80537, 7.03846, 6.26714, 5.49137, 4.71112, 3.92633]*1e
            -6;
            dRings = [dRings fliplr(dRings)]*1e6;
            LList = [LList fliplr(LList)]*1e6;
            COMSOl_Filenames = cell(length(LList),1);
10         for i = 1:length(LList)
                COMSOl_Filenames{i,1}=sprintf('PCFChalc_rend%s_L%s_D%s',strrep(num2str(rend),'.','-'),
                '-'),...
                strrep(num2str(LList(i)),'.','-'),strrep(num2str(dRings(i)),'.','-'));
            end
        end
15     end
    if ischar(FiberType)
        switch FiberType
            case 'plain' % no tapering test case
20                 COMSOl_Filenames = {COMSOl_Filenames{1}};
                    ztarget = 0.1;
                    taper_zlist = ztarget;
            case 'earlyW'
                L_BT = 0.075;
                L_DT = 0.03;
25                 L_W = 0.02;
                    taper_zlist=cumsum([L_BT L_DT/8*ones(1,8) L_W]);
                    ztarget=taper_zlist(end); %Target total length of fiber
            case 'smallBTAT'
30                 L_BT = 0.075;
                    L_DT = 0.03;
                    L_W = 0.15;
                    L_UT = 0.03;
                    L_AT = 0.04;

35                 taper_zlist=cumsum([L_BT L_DT/8*ones(1,8) L_W L_UT/8*ones(1,8)]);
                    ztarget=taper_zlist(end)+L_AT; %Target total length of fiber
            end
        else % Manually setting lengths
40             L_BT = FiberType(1);
                L_DT = FiberType(2);
                L_W = FiberType(3);
                L_UT = FiberType(4);
                L_AT = FiberType(5);
                taper_zlist=cumsum([L_BT L_DT/8*ones(1,8) L_W L_UT/8*ones(1,8)]);
45             ztarget=taper_zlist(end)+L_AT; %Target total length of fiber
        end
    end
end

```

Listing C.4: Content of CCS\_GetCOMSOLData.m

```

function [D_cellarr,Q_cellarr,gsTerms,taus] = CCS_GetCOMSOLData(P,COMSOL_Filenames,LossFile)

V = P.V;
w0 = P.w0;
5 wpump = P.wpump;
c = P.c;
Nmodes = P.Nmodes;

load(LossFile)
10 D_cellarr = cell(1,length(COMSOL_Filenames));
Q_cellarr = cell(2,length(COMSOL_Filenames));
gsTerms = cell(1,length(COMSOL_Filenames));
taus = cell(1,length(COMSOL_Filenames));

15 % N.B.!: for the implementation to be truly multimode, the linear operator
% should be computed separately for each mode (except b_0 and b_1), but
% since the main purpose of the code was to simulate different
% polarisation modes for which the linear operator is virtually identical,
% this has not been implemented.

20 % Setting beta0 and beta1 w.r.t. dispersion in waist
idx = ceil(length(COMSOL_Filenames)/2);
fprintf('Pre-loop: Loading %s, ',COMSOL_Filenames{idx})
load([COMSOL_Filenames{idx}])
25 neff = reshape(Data(1,1,:),[1 length(Flist)]);

propagation_constant = 2*pi*neff.*Flist/c;
beta = real(propagation_constant);
dV_in = 2*pi*(Flist(2)-Flist(1));
30 beta1 = (beta(3:end) - beta(1:end-2))/(2*dV_in);
beta = interp1(2*pi*Flist,beta,V + w0,'pchip',0);
beta1 = interp1(2*pi*Flist(2:end-1),beta1,V + w0,'pchip',0);

beta0_w0 = interp1(V + w0, beta, wpump,'pchip',0);
35 beta1_wpump = interp1(V + w0, beta1, wpump,'pchip',0);

for i = 1:length(COMSOL_Filenames)

    fprintf('Loading %s, \n',COMSOL_Filenames{i})
40 load([COMSOL_Filenames{i}]) % yields variables Flist and Data
neff = reshape(Data(1,1,:),[1 length(Flist)]);
GlassFraction = reshape(Data(1,14,:),[1,size(Data,3)]); % truncated
n0 = interp1(2*pi*Flist, neff, w0); % according to agger

45 propagation_constant = 2*pi*neff.*Flist/c;
beta = real(propagation_constant);
dV_in = 2*pi*(Flist(2)-Flist(1));

beta1 = (beta(3:end) - beta(1:end-2))/(2*dV_in);
50 beta2 = (beta(3:end) -2*beta(2:end-1) + beta(1:end-2))/dV_in^2;
beta3 = (1/2*beta(5:end) -beta(4:end-1) + beta(2:end-3) -1/2*beta(1:end-4))/dV_in^3;

% interpolating
GlassFraction = interp1(2*pi*Flist,GlassFraction,V + w0,'pchip',0);
55 attenuation_constant = interp1(2*pi*Flist,imag(propagation_constant),V + w0,'pchip',0);
beta = interp1(2*pi*Flist,beta,V + w0,'pchip',0);
beta1 = interp1(2*pi*Flist(2:end-1),beta1,V + w0,'pchip',0);
beta2 = interp1(2*pi*Flist(2:end-1),beta2,V + w0,'pchip',0);
beta3 = interp1(2*pi*Flist(3:end-2),beta3,V + w0,'pchip',0);

60 neff = interp1(2*pi*Flist,neff,V+ w0,'pchip',0);
Aeff = interp1(2*pi*Flist,Aeff,V+ w0,'pchip',eps);

OverlapInt1 = interp1(2*pi*Flist,OverlapInt1,V+ w0,'pchip',0);
65 OverlapInt2 = interp1(2*pi*Flist,OverlapInt2,V+ w0,'pchip',0);

```

```

70 % interpolate loss data
Loss_Beta_Meas=interp1(c*10^6./LossData(:,1),LossData(:,2),(P.V+P.w0)/(2*pi),'pchip',0);
Loss_Beta_Meas(Loss_Beta_Meas>0)=0;
Loss_Beta=Loss_Beta_Meas;
Loss_Beta((P.V+P.w0)/(2*pi) > 235e12)=-1/(20*log10(exp(1)))*1e3; %High frequency loss.
alpha = -2*(P.alphaCoeffA*attenuation_constant + P.alphaCoeffB*GlassFraction .* Loss_Beta)
;

75 %% Linear operator

B = beta - beta0_w0 - beta1_wpump.*V;

D_cellarr{i} = fftshift(1i*B - alpha/2); % linear operator

80 %% Q

Q1 = zeros(length(V),Nmodes^4);
Q2 = zeros(length(V),Nmodes^4);

85 for p = 0:Nmodes-1
    for ll = 0:Nmodes-1
        for m = 0:Nmodes-1
            for n = 0:Nmodes-1
90                 if P.MPD
                    Q1(:,1 + n + 2*m + 4*ll + p*8) = OverlapInt1(:,p+1,ll+1,m+1,n+1);
                    Q2(:,1 + n + 2*m + 4*ll + p*8) = OverlapInt2(:,p+1,ll+1,m+1,n+1);
                else
95                     Q1(:,1 + n + 2*m + 4*ll + p*8) = interp1(V + w0,...
                        OverlapInt1(:,p+1,ll+1,m+1,n+1),w0);
                    Q2(:,1 + n + 2*m + 4*ll + p*8) = interp1(V + w0,...
                        OverlapInt2(:,p+1,ll+1,m+1,n+1),w0);
                end
100            end
        end
    end
end

105 Q1 = P.eps0^2*real(n0)^2*c^2/12 * Q1;
Q2 = P.eps0^2*real(n0)^2*c^2/12 * Q2;

%% Shock term

110 if P.useAllShockTerms
    tauArr = zeros(2,Nmodes^4);

    for p = 1:Nmodes^4
        dQ1 = interp1(P.V(2:end-1), (Q1(3:end,1)-Q1(1:end-2,1))/(2*P.dV) ./ Q1(2:end-1,1),
            0, 'pchip');
        dQ2 = interp1(P.V(2:end-1), (Q2(3:end,1)-Q2(1:end-2,1))/(2*P.dV) ./ Q2(2:end-1,1),
115            0, 'pchip');
        tauArr(1,p) = 1/w0 + dQ1; % In CCS_Integrator: (1 + V.* tauArr(p))
        tauArr(2,p) = 1/w0 + dQ2; % In CCS_Integrator: (1 + V.* tauArr(p))
    end
    taus{i} = tauArr;
    gsTerms{i} = 1i*P.n2*P.w0/P.c;
else
    dAeff = interp1(P.V(2:end-1), (Aeff(3:end) - Aeff(1:end-2))/(2*P.dV/(2*pi)),0,'pchip',
        0);
    gsTerms{i} = fftshift(1i*P.n2*P.w0/P.c*(1+V.*(1/w0 - P.gsCoeff./Aeff*dAeff)));
120 end

125 %% Finalize
Q_cellarr{1,i} = Q1;
Q_cellarr{2,i} = Q2;

```

```

130     fprintf('gamma at w0 is ca. %0.3f\n',3*interp1(V,Q1(:,1),0)*P.n2*P.w0/c)
end

```

Listing C.5: Content of CCS\_Integrator.m

```

function [Z,ATZ,ext] = CCS_Integrator(P,ATO, zlist,taper_zlist,D_c,Q_c,opt)

%% Init
Z = zeros(1,P.Nz);
5  ATZ = zeros(P.Nz, P.Nt*P.Nmodes);
nzi = 1; % next z idx
nextz = 0; % forcing the first save in the loop

AT = ATO;
10 z = 0;
steps = 0;
alpha = zeros(P.Nt,1);

% Handle
15 Pnf = @(AT_pIn,alphaIn) PhotonNumber(P.Nt,P.Nmodes,AT_pIn,...
    P.Vshift,P.w0,P.dV,alphaIn,P);

% Default options
useAdapt = 1;
20 useAdapt_RKerr = 1; % whether to use RK error estimators if possible
useAdapt_mindz = 0.5e-5; % do not let step sizes come below this
useAdapt_maxdz = 1e-2; % do not let step sizes come above this
dz = 1e-4; % initial dz
tol = 1e-5;
25 solver = 1;

if isfield(opt, 'useAdapt'), useAdapt = opt.useAdapt; end
if isfield(opt, 'useAdapt_RKerr'), useAdapt_RKerr = opt.useAdapt_RKerr; end
if isfield(opt, 'useAdapt_mindz'), useAdapt_mindz = opt.useAdapt_mindz; end
30 if isfield(opt, 'useAdapt_maxdz'), useAdapt_maxdz = opt.useAdapt_maxdz; end
if isfield(opt, 'tol'), tol = opt.tol; end
if isfield(opt, 'dz'), dz = opt.dz; end
if isfield(opt, 'solver'), solver = opt.solver; end

35 ext = struct();
ext.PNum = zeros(length(Z),1);
ext.predPNum = zeros(length(Z),1);
ext.steps = zeros(length(Z),1);
ext.dz = zeros(length(Z),1);
40 ext.time = zeros(length(Z),1);
PNum = Pnf(ATO,alpha);
predPNum = PNum;

tic
45 while nzi <= length(Z)
    %% Saving
    if z+1e-13 > nextz
        Z(nzi) = z;
        ext.steps(nzi) = steps;
50     ext.dz(nzi) = dz;
        ext.time(nzi) = toc;
        ext.PNum(nzi) = PNum;
        ext.predPNum(nzi) = predPNum;
        ATZ(nzi,:) = AT;
55
        eta = (toc/steps)*(zlist(end)-z)/dz;
        fprintf('T:%04.0f-%04.0f S:%.5d z:%0.2e dz:%0.2e ni:%.2d p:%0.4e pp:%0.4e\n',toc
            ,eta,steps,z,dz,nzi,PNum,predPNum)

        nzi = nzi + 1;
60     if nzi > length(Z) || z+1e-13 > zlist(end), break; end

```

```

    nextz = zlist(nzi);
end

%% Preprocessing
% tapering blending
65 if z >= taper_zlist(end)
    D = D_c{end};
    Q1 = Q_c{1,end};
    Q2 = Q_c{2,end};
70 P.gsTerm = P.gsTerms{end};
    P.tau = P.taus{end};
elseif z <= taper_zlist(1)
    D = D_c{1};
75 Q1 = Q_c{1,1};
    Q2 = Q_c{2,1};
    P.gsTerm = P.gsTerms{1};
    P.tau = P.taus{1};
else
80 idx2 = find(z < taper_zlist, 1);
    idx1 = idx2 - 1;
    r = (z-taper_zlist(idx1))/(taper_zlist(idx2)-taper_zlist(idx1));
    D = D_c{idx2}*r + (1-r)*D_c{idx1};
    Q1 = Q_c{1,idx2}*r + (1-r)*Q_c{1,idx1};
    Q2 = Q_c{2,idx2}*r + (1-r)*Q_c{2,idx1};
85 P.gsTerm = P.gsTerms{idx2}*r + (1-r)*P.gsTerms{idx1};
    P.tau = P.taus{idx2}*r + (1-r)*P.taus{idx1};
end
alpha = -2*real(D);

90 %% Processing
if ~useAdapt
    switch solver
        case 1 % RK4IP method
95 ATzh = IP_Step(P,AT,dz,D,Q1,Q2);
        case 2 % DPIP method
            [ATzh,ATzh4] = IP_Step_DOPRI(P,AT,dz,D,Q1,Q2);
        case 3 % Fehlberg method
            [ATzh,ATzh4] = IP_Step_Fehlberg(P,AT,dz,D,Q1,Q2);
100 end

    [PNum, dPdz] = Pnf(ATzh,alpha);
    predPNum = predPNum + dPdz*dz;
    AT = ATzh;
105 z = z + dz;
    steps = steps + 1;
else
    acceptStep = 0;

110 while ~acceptStep
        acceptStep = 1;

        switch solver
            case 1 % RK4IP method, no RK error estimate available
115 ATzh = IP_Step(P,AT,dz,D,Q1,Q2);
                [PNum_new, dPdz] = Pnf(ATzh,alpha);
                PTrue = PNum + dPdz*dz;
                predPNum_new = predPNum + dPdz*dz;
                relerr = abs(PNum_new-PTrue) / PTrue;
            case 2 % DPIP method
120 [ATzh,ATzh4] = IP_Step_DOPRI(P,AT,dz,D,Q1,Q2);
                [PNum_new, dPdz] = Pnf(ATzh,alpha);
                PTrue = PNum + dPdz*dz;
                predPNum_new = predPNum + dPdz*dz;
                if useAdapt_RKerr
125 relerr = sum(abs( abs(ATzh).^2 - abs(ATzh4).^2 )) / max(abs(ATzh).^2);
                else

```

```

        relerr = abs(PNum_new-PTrue) / PTrue;
    end
130
    case 3 % Fehlberg method
        [ATzh,ATzh4] = IP_Step_Fehlberg(P,AT,dz,D,Q1,Q2);
        [PNum_new, dPdZ] = Pnf(ATzh,alpha);
        PTrue = PNum + dPdZ*dz;
135
        if useAdapt_RKerr
            relerr = norm(ATzh-ATzh4)/norm(ATzh);
        else
            relerr = abs(PNum_new-PTrue) / PTrue;
        end
140
    end

    if relerr > 2*tol && dz > useAdapt_mindz
        % reject step
        acceptStep = 0;
145
        dz = dz/2;
    else
        % accept step
        AT = ATzh;
        z = z + dz;
        steps = steps + 1;
        PNum = PNum_new;
        predPNum = predPNum_new;
    end
150
end
end

% prepare dz for next iteration
if relerr > tol && dz > useAdapt_mindz
    dz = dz/2^(1/5);
elseif relerr < 0.1*tol && dz < useAdapt_maxdz
160
    dz = dz*2^(1/5);
end

% making sure we hit the exact end
if z + dz > zlist(end)
165
    dz = zlist(end)-z;
end

end
end

170
fprintf('Steps taken %d\n',steps);

end

175 %% Functions
function [P,dPdZ] = PhotonNumber(Nt,Nmodes,AT_p,V,w0,dV,alpha,P)

photonDensity = zeros(Nt,1);
for p = 0:Nmodes-1
180
    AT=AT_p((1:Nt)+Nt*p);
    photonDensity = photonDensity + abs(P.fftc(AT)).^2 ./ (V+w0) * dV;
end

P = sum(photonDensity);
185
dPdZ = -sum(alpha .* photonDensity);

end

190
function [ATzh5,ATzh4] = IP_Step_DOPRI(P,AT,h,D,Q1,Q2)

Nop = @(AT) NonlinearOperator(P,AT,Q1,Q2);
FT = @(FD) MMfftc(FD, P.Nt,P.Nmodes);
iFT = @(TD) MMifftc(TD,P.Nt,P.Nmodes);

```

```

195     hD = h*D;
        expDf = @(x) repmat(exp(x*hD), [P.Nmodes 1]);

        expD = expDf(1);
        AI = iFT(expD.*FT(AT));
200     k1 = iFT(expD.*FT(h*Nop(AT)));
        k2 = iFT(expDf(4/5).*FT(h*Nop(iFT(expDf(-4/5).*FT(AI+k1/5)))));
        k3 = iFT(expDf(7/10).*FT(h*Nop(iFT(expDf(-7/10).*FT(AI+3/40*k1+9/40*k2)))));
        k4 = iFT(expDf(1/5).*FT(h*Nop(iFT(expDf(-1/5).*FT(AI+44/45*k1-56/15*k2+32/9*k3)))));
        k5 = iFT(expDf(1/9).*FT(h*Nop(iFT(expDf(-1/9).*FT(AI+19372/6561*k1-25360/2187*k2
205         +64448/6561*k3-212/729*k4)))));

        k6 = h*Nop(AI+9017/3168*k1-355/33*k2+46732/5247*k3+49/176*k4-5103/18656*k5);
        lincomb = AI+35/384*k1+500/1113*k3+125/192*k4-2187/6784*k5+11/84*k6;
        k7 = h*Nop(lincomb);

210     ATzh5 = (lincomb);
        ATzh4 = (AI+5179/57600*k1+7571/16695*k3+393/640*k4-92097/339200*k5+187/2100*k6+1/40*k7);
end

function [ATzh5,ATzh4] = IP_Step_Fehlberg(P,AT,h,D,Q1,Q2)
215
    Nop = @(AT) NonlinearOperator(P,AT,Q1,Q2);
    FT = @(FD) MMfftfc(FD, P.Nt,P.Nmodes);
    iFT = @(TD) MMifftc(TD,P.Nt,P.Nmodes);

220     hD = h*D;
        expDf = @(x) repmat(exp(x*hD), [P.Nmodes 1]);

        expD = expDf(1/2);
        AI = iFT(expD.*FT(AT));
225     k1 = iFT(expD.*FT(h*Nop(AT)));
        k2 = iFT(expDf(1/4).*FT(h*Nop(iFT(expDf(-1/4).*FT(AI+k1/4)))));
        k3 = iFT(expDf(1/8).*FT(h*Nop(iFT(expDf(-1/8).*FT(AI+3/32*k1+9/32*k2)))));
        k4 = iFT(expDf(-11/26).*FT(h*Nop(iFT(expDf(11/26).*FT(AI+1932/2197*k1-7200/2197*k2
        +7296/2197*k3)))));
        k5 = iFT(expDf(-1/2).*FT(h*Nop(iFT(expDf(1/2).*FT(AI+439/216*k1-8*k2+3680/513*k3-845/4104*
230         k4)))));

        k6 = h*Nop(AI-8/27*k1+2*k2-3544/2565*k3+1859/4104*k4-11/40*k5);

        ATzh5 = iFT(expD.*FT(AI+16/135*k1+6656/12825*k3+28561/56430*k4-9/50*k5+2/55*k6));
        ATzh4 = iFT(expD.*FT(AI+25/216*k1+1408/2565*k3+2197/4104*k4-1/5*k5));
235 end

function ATzh = IP_Step(P,AT,h,D,Q1,Q2)

240     Nop = @(AT) NonlinearOperator(P,AT,Q1,Q2);
        FT = @(FD) MMfftfc(FD, P.Nt,P.Nmodes);
        iFT = @(TD) MMifftc(TD,P.Nt,P.Nmodes);

        % linear op
245     expD = repmat(exp(h/2*D), [P.Nmodes 1]);
        AI = iFT(expD.*FT(AT));
        k1 = iFT(expD.*FT(h*Nop(AT)));
        k2 = h*Nop(AI + k1/2);%.*(AI + k1/2);
        k3 = h*Nop(AI + k2/2);%.*(AI + k2/2);
250     k4 = h*Nop(iFT(expD.*FT(AI + k3)));

        ATzh = iFT(expD.*FT(AI + k1/6 + k2/3 + k3/3)) + k4/6;
end

255 function N = NonlinearOperator(P,AT,Q1v,Q2v)

    Nt = P.Nt;

```

```

260 N = zeros(Nt,1);
A = cell(1,P.Nmodes);
for p = 0:P.Nmodes-1
    A{p+1} = AT((1:Nt) + p*Nt);
end
265
for p = 0:P.Nmodes-1
    Ntemp = zeros(Nt,1);
    for ll = 0:P.Nmodes-1
        for m = 0:P.Nmodes-1
270             for n = 0:P.Nmodes-1
                Q1 = Q1v(:,1 + n + 2*m + 4*ll + 8*p);
                Q2 = Q2v(:,1 + n + 2*m + 4*ll + 8*p);
                if norm(Q1) < eps && norm(Q2) < eps, continue, end
275                 A1 = A{ll+1};
                 Am = A{m+1};
                 An = A{n+1};

                 if abs(P.fr) > eps
280                     RamanConv1 = (1-P.fr)*Am.*conj(An) + P.ifftc(P.RW.*P.fftc(Am.*conj(An)));
                     RamanConv2 = (1-P.fr)*Am.*An + P.ifftc(P.RWexp.*P.fftc(Am.*An));
                     else
                     RamanConv1 = (1-P.fr)*Am.*conj(An);
                     RamanConv2 = (1-P.fr)*Am.*An;
                     end

285                     if P.useAllShockTerms
                         tau1 = P.tau(1,1 + n + 2*m + 4*ll + 8*p);
                         tau2 = P.tau(2,1 + n + 2*m + 4*ll + 8*p);
                         contrib = (1 + P.Vshift*tau1).*P.fftc(2*Q1.*A1 .* RamanConv1) ...
290                             + (1 + P.Vshift*tau2).*P.fftc(Q2.*conj(A1) .* RamanConv2);
                     else
                         contrib = P.fftc(2*Q1.*A1 .* RamanConv1 ...
295                             + Q2.*conj(A1) .* RamanConv2);
                     end

                    Ntemp = Ntemp + contrib;
                end
            end
        end
    end
300
    N((1:Nt) + Nt*p) = P.ifftc(P.gsTerm .* Ntemp);
end
305
end

```

# APPENDIX D

## Soliton numbers

---

The soliton number and associated parameters inferred from the spectrogram in chapter 7 are shown in the table below.

**Table D.1:** Soliton numbers that were calculated based on estimations from the spectrogram and corresponding time domain power plots.

N	P [kW]	$\gamma$ [Wm] <sup>-1</sup>	GVD [ps <sup>2</sup> /m]	$T_{\text{FWHM}}$ [ps]	$A_{\text{eff}}$ [ $\mu\text{m}^2$ ]
2.03	5.29	0.19	-0.89	0.08	35
1.76	4.14	0.19	-0.71	0.07	35
1.74	1.78	0.19	-0.92	0.12	35
1.91	2.09	0.19	-0.89	0.12	35
1.63	3.83	0.19	-0.39	0.05	35
1.86	1.61	0.19	-0.99	0.14	35
1.61	0.12	0.19	-0.74	0.38	35
1.26	0.51	0.19	-0.59	0.13	35
2.21	0.17	0.06	-0.39	0.60	120
1.62	0.86	0.06	-0.94	0.30	120
1.17	0.36	0.06	-0.76	0.30	120
0.98	0.35	0.06	-0.56	0.22	120

# Bibliography

---

- [1] RR Alfano and SL Shapiro. “Emission in the Region 4000 to 7000 Å via Four-Photon Coupling in Glass”. In: *Physical Review Letters* 24.11 (1970).
- [2] John M. Dudley, Goëry Genty, and Stéphane Coen. “Supercontinuum Generation in Photonic Crystal Fiber”. en. In: *Reviews of Modern Physics* 78.4 (October 2006).
- [3] Christian Skovmøller Agger and Ole Bang. “Infrared Supercontinuum Generation in Soft-Glass Fibers”. PhD thesis. DTU Fotonik, 2013.
- [4] JM Harbold et al. “Highly Nonlinear As-S-Se Glasses for All-Optical Switching”. In: *Optics Letters* 27.2 (2002).
- [5] Richard E Slusher et al. “Large Raman Gain and Nonlinear Phase Shifts in High-Purity As<sub>2</sub>Se<sub>3</sub> Chalcogenide Fibers”. In: *JOSA B* 21.6 (2004).
- [6] George B Arfken and Hans J Weber. “Mathematical Methods for Physicists”. In: (1999).
- [7] G. P. Agrawal. *Nonlinear Fiber Optics*. Fifth edition. Amsterdam: Elsevier/Academic Press, 2013.
- [8] Andrei V Lavrinenko et al. *Numerical Methods in Photonics*. Volume 1. CRC Press, 2014.
- [9] Robert W Boyd. *Nonlinear Optics*. Academic press, 2003.
- [10] A Zakery and Stephen Richard Elliott. *Optical Nonlinearities in Chalcogenide Glasses and Their Applications*. Volume 135. Springer, 2007.
- [11] Simon Toft Sørensen and Ole Bang. “Deep-Blue Supercontinuum Light Sources Based on Tapered Photonic Crystal Fibers”. English. OCLC: 930993080. PhD thesis. DTU Fotonik, Technical University of Denmark, 2013.
- [12] Bora Ung and Maksim Skorobogatiy. “Chalcogenide Microporous Fibers for Linear and Nonlinear Applications in the Mid-Infrared”. In: *Optics express* 18.8 (2010).
- [13] Francesco Poletti and Peter Horak. “Description of Ultrashort Pulse Propagation in Multimode Optical Fibers”. In: *JOSA B* 25.10 (2008).
- [14] Roman Khakimov et al. “Numerical Solver for Supercontinuum Generation in Multimode Optical Fibers”. en. In: *Optics Express* 21.12 (June 2013).
- [15] Jesper Laegsgaard. “Mode Profile Dispersion in the Generalized Nonlinear Schrödinger Equation”. In: *Optics express* 15.24 (2007).
- [16] Michael H. Frosz. “Supercontinuum Generation in Photonic Crystal Fibres: Modelling and Dispersion Engineering for Spectral Shaping”. PhD thesis. COM, DTU, 2007.
- [17] J. M. Dudley and J. R. Taylor, editors. *Supercontinuum Generation in Optical Fibers*. OCLC: ocn456838616. Cambridge ; New York: Cambridge University Press, 2010.
- [18] Johan Hult. “A Fourth-Order Runge-Kutta in the Interaction Picture Method for Simulating Supercontinuum Generation in Optical Fibers”. In: *Journal of Lightwave Technology* 25.12 (December 2007).

- 
- [19] Keith J. Blow and David Wood. “Theoretical Description of Transient Stimulated Raman Scattering in Optical Fibers”. In: *IEEE Journal of Quantum Electronics* 25.12 (1989).
- [20] Benjamin Michael Caradoc-Davies. “Vortex Dynamics in Bose-Einstein Condensates”. In: *Ph. D. thesis* (2000).
- [21] A.M. Heidt. “Efficient Adaptive Step Size Method for the Simulation of Supercontinuum Generation in Optical Fibers”. In: *Journal of Lightwave Technology* 27.18 (September 2009).
- [22] Christian Rosenberg Petersen et al. “Increased Mid-Infrared Supercontinuum Bandwidth and Average Power by Tapering Large-Mode-Area Chalcogenide Photonic Crystal Fibers”. en. In: *Optics Express* 25.13 (June 2017).
- [23] Randall J LeVeque. “Finite Difference Methods for Differential Equations”. In: *Draft version for use in AMath* 585.6 (1998).
- [24] Chin-Lin Chen. *Foundations for Guided-Wave Optics*. en. Google-Books-ID: LxzWP-skhn5OC. John Wiley & Sons, September 2006.
- [25] P. Hlubina, M. Kadulová, and D. Ciprian. “Spectral Interferometry-Based Chromatic Dispersion Measurement of Fibre Including the Zero-Dispersion Wavelength”. en. In: *Journal of the European Optical Society: Rapid Publications* 7 (May 2012).
- [26] C Quémard et al. “Chalcogenide Glasses with High Non Linear Optical Properties for Telecommunications”. In: *Journal of Physics and Chemistry of Solids* 62.8 (2001).
- [27] Qing Wang et al. “Mode-Locked 2 Mm Laser with Highly Thulium-Doped Silicate Fiber”. In: *Optics letters* 34.23 (2009).
- [28] Perrine Toupin et al. “Optical Aging of Chalcogenide Microstructured Optical Fibers”. In: *J. Lightwave Technol.* 32.13 (July 2014).